Nanophotonic Phenomena in Dielectric Photonic Crystals

Thesis by

Ryan Cecil Ng

In Partial Fulfillment of the Requirements for the
Degree of
Doctor of Philosophy

CALIFORNIA INSTITUTE OF TECHNOLOGY
Pasadena, California

2020
Defended December 9, 2019

Ryan Cecil Ng
ORCID: 0000-0002-0527-9130

ACKNOWLEDGEMENTS

Even as I near the end of my time here at Caltech, everything feels so surreal, and it is still hard to believe that we have almost reached the end. These past years have been an incredible opportunity to learn and grow, not only as a scientist and researcher, but also as a person, and I can visibly see a difference in my emotional and scientific maturity. I have never been someone that has been particularly adept at accurately articulating my personal feelings, but there are so many amazing people that I have met along the way to whom I am extremely grateful for and by whom I continue to be inspired.

First, I wanted to thank my research advisor, Professor Julia Greer. In addition to just being a great, positive, and supportive mentor, role model, and research advisor, Julia has always been open to new ideas and has always provided me with almost complete creative research freedom to pursue whatever scientific problems happened to be interesting at the time. She really allowed graduate school to become a scientific playground of sorts for me. I am extremely grateful for her constant encouragement and support, and appreciated her consideration to always placing the well-being and professional development of her students as the highest priority. I am grateful for the faith she placed in me beginning from when I was a young, blossoming, new graduate student with no particular research direction in mind. Through her help and support, I discovered my love for nanoscience and nanofabrication, which has really shaped my research in the form of many different collaborations over the years. I also would like to thank my committee members, Andrei Faraon, Mikhail Shapiro, and John Brady for taking the time to serve on my candidacy and thesis committees, and for all of the interesting discussions that we have had over the years.

In addition to Julia's guidance, I have been extremely lucky to have had the guidance of Kate Fountaine throughout my PhD, who has been an incredible and extremely patient mentor and friend, and has taught me so much about nanophotonics, optical simulations, and science in general. Through regular meetings, hundreds of emails, and plenty of extremely silly questions, I have gained so many invaluable technical skills through my collaborations with Kate. I am immensely grateful for her mentorship, and a very significant portion of my research in graduate school would not have been possible without her.

An incredible amount of time during my PhD was spent on nanofabrication and troubleshooting in the cleanroom at Caltech, in the Kavli Nanoscience Institute (KNI). So much of what I learned came from the amazing staff in the KNI. I am extremely grateful for the help of all of the cleanroom staff, past and present, that I have had the opportunity to work with and learn from: Matthew Sullivan Hunt, Melissa Melendes, Nathan Lee, Bert Mendoza, Alex Wertheim, and Guy DeRose.

I have been incredibly blessed to have made some incredible friendships over the last several years in graduate school. First, I wanted to thank Victoria Chernow for her friendship and scientific support, having become one of my closest friends in graduate school. I am also grateful to the "ChemE bro squad:" John Birmingham, Ben Lacetti, Steven Lee, and Ben Kanevsky. The first couple years of graduate school were easily the most difficult I have ever experienced, but also some of the most entertaining due to this great group of friends. From regular hang outs, to discussions about life, I also wanted to thank some of the other closest friends I made at Caltech: Neal Brodnik, Christina Burghard, and Amylynn Chen. I also wanted to specifically acknowledge all the friends who taught me some scientific tricks or helped contribute to my thesis indirectly in some way, and wanted to thank in no particular order: Ottman Tertuliano, Rebecca Gallivan, Sophia Cheng, Kelly Mauser, Michelle Sherrott, Dagny Fleischman, and Lucas Meza. I am also incredibly thankful to the rest of the Greer group, for being really fun, friendly, and supportive lab mates. Our group is definitely one of the most supportive, outgoing, and fun groups at Caltech. I wanted to also acknowledge some of the other incredible close friends I have made at Caltech who have contributed to my experience and development as a person: Austin Dulaney, Jane Zhang, Phillipe Pearson, Stphane Delalande, and Mike Citrin. I also owe a big thank you to my closest friends outside of Caltech who have helped me maintain my sanity over the years outside of the lab: Adriane Turner, Mingchen Shen, Morgan Hubbell, Oi Long, Jennifer Osaki, Priscilla Chan, Julie Ching, Sean Chiu, Rungchit Thunyakij, Dustin Lai, Emily Nakamoto, Cecilia Chow, and Jennifer Koo. There are so many people that have contributed to my development and success in these past years, and I am forever grateful to each and every one of them, in addition to only the ones that I listed here. I legitimately believe that I would not have successfully made it to this point without the help of all of these people.

Prior to coming to graduate school, I was blessed with especially incredible undergraduate research mentors: Professor Mike Gordon and Alex Heilman. They were my first mentors in the world of research, and gave me so much support. I have never known another professor who was so willing to make time to attend every research talk given, even by an undergraduate in their lab. A special thank you as well to my graduate research mentor, Alex, who spent so much time patiently helping me learn and grow as a scientist. I attribute my ability to create and give good research presentations primarily to all of the time and advice Alex gave me. Outside the lab, Alex was also a great friend and a fun person to be around. Without their inspiration and guidance, I would not have made it all the way to graduate school. I am also grateful to Professors William Tang, Melissa Grunlan, and Glenn Fredrickson for the opportunies to have done research in their lab as an undergraduate.

There have also been some amazing administrators and staff at Caltech, who were always so willing to lend an ear. In particular, I wanted to thank Angie Riley and Allison Kinard, with whom I have always been able to discuss whatever was on my mind.

Of course, absolutely none of this would have been possible without the incredible love and support of my family: Joely, Ken, and Lesley Ng. In particular, my mother is the strongest human being I know, and I continue to be impressed by everything she achieves and I constantly aspire to be more like her. My family has made so many sacrifices to provide me with the opportunities that I have today, and for that I will be forever indebted.

Finally, I wanted to acknowledge Ximena Zubaran: all of her love, care, and support have kept me surprisingly sane in the final year of graduate school, despite the hardships that tend to come with a PhD. Thank you for all of your patience and support.

I genuinely believe that each and every one of these people, along with many others, have contributed to who I have become. I am extremely grateful to all of the amazing and incredible people I have had the wonderful opportunity to know.

ABSTRACT

Photonic crystals are periodic optical nanostructures with varying dielectric constant that allow light flow to be controlled and manipulated much in a similar way to electrons within a semiconductor crystal. These nanostructures tend to have a spatially varying refractive index on the order of the wavelength of light to be manipulated. 1D and 2D photonic crystals have already garnered significant attention in the realm of thin-film optics, while 3D photonic crystals have been thus far limited in application, due to difficulties in fabrication and a lack of available materials for fabrication.

In this work, we first explore 1D and 2D photonic crystals based on the concept of a guided mode resonance, which manifests as a narrow near-unity resonance in reflection or transmission that arise from the coupling of an incident wave into a leaky waveguide mode via a grating vector that is subsequently re-radiated. Such a resonance is well-suited for multi- and hyper- spectral filtering applications in the infrared. We designed a platform consisting of amorphous Si arrays embedded in SiO_2 in simulation and experiment for application as narrow stopband filters. We present the tunability of the spectral characteristics of the resonance in these arrays through variation of array geometric parameters in simulation and experiment. Guided mode resonance designs often consider only the case of an infinite array, where the leaky waveguide mode can propagate laterally for hundreds of periods, allowing for this mode to eventually scatter out of the array giving rise to the characteristic narrow near-unity rapid spectral variations of a GMR. With an insufficient number of periods, the quality factor and thus the optical filtering performance is greatly diminished. Thus, we further extend our analysis to compact periodic arrays of finite size, which are required for high spatial resolution snapshot imaging, and introduce array designs that operate under finite size limitations in the near-infrared.

We then transition to 3D photonic crystals, exploring the use of an additive manufacturing process to directly fabricate nanocrystalline rutile TiO_2 with $\sim$100 nm resolution. Though TiO_2 was chosen as the model material, the key to this work is that a similar process can be used to print many different materials, enabling future applications of 3D photonic crystals. The focus here is the additive manufacturing of high index materials such as TiO_2, and its potential for photonic applications is demonstrated by characterizing the optical band

gap of 3D PhC TiO_2 structures printed with this method. We present a system where the ability to print high refractive index 3D photonic crystals would be useful, by studying 3D polymer-germanium core-shell structures that should exhibit all-angle negative refraction in the mid-infrared regime.

PUBLISHED CONTENT AND CONTRIBUTIONS

Chapter 2 is adapted from:

[1] **Ryan C. Ng**, Julia R. Greer, and Katherine T. Fountaine. "Fabrication of ultra-thin Si nanopillar arrays for polarization-independent spectral filters in the near-IR." *Proceedings of SPIE*. 10541 (2018).

R.C.N. designed and optimized the structures in FDTD simulations, fabricated the filters, assisted in building the optical set-up, prepared the data, and wrote the manuscript.

[2] **Ryan C. Ng**, Juan C. Garcia, Julia R. Greer, and Katherine T. Fountaine. "Polarization-independent, narrowband, near-IR spectral filters via guided mode resonances in ultrathin a-Si nanopillar arrays." *ACS Photonics*. 6 (2), 265-271 (2019). DOI:10.1021/acsphotonics.8b01253

R.C.N. designed and optimized the structures in FDTD simulations, fabricated the filters, assisted in building the optical set-up, took the optical characterization measurements, prepared the data, and wrote the manuscript.

Chapter 3 is adapted from:

[3] **Ryan C. Ng**, Juan C. Garcia, Julia R. Greer, and Katherine T. Fountaine. "Miniaturization of a-Si guided mode resonance filter arrays for near-IR multi-spectral filtering." (in preparation)

R.C.N. designed and optimized the structures in FDTD simulations, fabricated the filters, prepared the data, and wrote the manuscript.

Chapter 5 is adapted from:

[4] Andrey Vyatskikh, **Ryan C. Ng**, Bryce W. Edwards, and Julia R. Greer. "Additive manufacturing of titanium dioxide for dielectric photonic crystals." *Proceedings of SPIE*. 10930 (2019).

[5] Andrey Vyatskikh, **Ryan C. Ng**, Bryce Edwards, Ryan M. Briggs, and Julia R. Greer. "Nanoscale additive manufacturing of high refractive index titanium dioxide for 3D dielectric photonic crystals." (submitted)

R.C.N. generated the code to fabricate the woodpile structures, computed, generated, and interpreted the band structures in PWE simulations, optically characterized woodpiles in FTIR, and edited the manuscript.

[6] Victoria F. Chernow, **Ryan C. Ng**, and Julia R. Greer. "Designing core-shell photonic crystal lattices for negative refraction." *Proceedings of SPIE*. 10112 (2017).

[7] Victoria F. Chernow, **Ryan C. Ng**, S. Peng, Harry A. Atwater, and Julia R. Greer. "Dispersion Mapping in 3-Dimensional Core-Shell Photonic Crystal Lattices Capable of Negative Refraction in the Mid-Infrared." (in preparation)

R.C.N. generated the code to fabricate the negative refractive index structures structures, participated in initial tests of the structures, contributed and optimized significant aspects of the fabrication procedure, and edited the manuscript.

TABLE OF CONTENTS

LIST OF ILLUSTRATIONS

LIST OF TABLES

Chapter 1

INTRODUCTION

1.1 Introduction

Nanophotonics, at its core, is the study of light-matter interactions on the nanoscale and how these interactions can be controlled through the use of nanostructures on the length scale of the wavelength of light. To manipulate light at this length scale for applications in the ultraviolet, visible, and near-infrared (IR), structures with resolutions as low as 10's of nanometers must be fabricated. While traditionally limited by available techniques in nanofabrication, the growth and development of the field of nanophotonics has largely been a result of somewhat recent technological developments such as complementary metal-oxide-semiconductor (CMOS) silicon processes in the past several decades enabling the ability to precisely fabricate structures at these length scales.

Nanophotonics can broadly be divided into four thrusts: electron confinement effects on the optical properties of matter, the quantum optics of nanostructures, optics and optical engineering with metal-dielectric nanostructures, and light wave confinement phenomena in structured dielectrics [1]. The first of these thrusts, electron confinement effects, is often referred to as quantum confinement effects and utilizes size-dependent absorption/emission effects in systems such as quantum dots, quantum wells, or quantum wires. The second of these thrusts is quantum optics, where spontaneous emission can be controlled via engineering of the density of states, traditionally in a cavity through the Purcell effect and Fermi's golden rule. In such a system, if a band gap exists, as the total number of states within the system must be conserved, the local density of states is "redistributed" to the band gap edges. If light can couple to these photonic band gap edges where the local density of states is higher, emission is also enhanced by Fermi's golden rule. The best resonators to date to observe these effects are metal nanostructures and photonic crystals. The third of these thrusts is optical engineering in metal-dielectric nanostructures, or nanoplasmonics. This field focuses on the notion of a surface plasmon, a collective oscillation of electrons at a metal surface. While metals traditionally were not considered

important to optics due to their large optical losses, surface plasmon resonances can drastically enhance light-matter interactions, and have found widespread applications. The focus of this work is mostly based on the lattermost of these four thrusts, in light wave confinement in dielectric materials, namely in periodic structures that have come to be known as photonic crystals (PhCs). A PhC is a periodic optical nanostructure that possesses regularly spatially repeating regions of varying dielectric constant in one, two, or three dimensions. The addition of this type of architecture strongly influences the way in which light can propagate within a system, analogous to the way in which solids control the propagation of electron waves. PhCs can possess something known as an optical or photonic band gap given sufficient refractive index contrast, in which light propagation of certain optical modes is inhibited.

This notion is primarily classical, and thus can be explained through the classical Maxwell's equations:

$$\nabla \times \mathbf{E} + \frac{\partial \mathbf{B}}{\partial t} = 0 \tag{1.1}$$

$$\nabla \times \mathbf{H} - \frac{\partial \mathbf{D}}{\partial t} = \mathbf{J} \tag{1.2}$$

$$\nabla \cdot \mathbf{D} = \rho \tag{1.3}$$

$$\nabla \cdot \mathbf{B} = 0 \tag{1.4}$$

where $\mathbf{E}$ is the electric field, $\mathbf{H}$ is the magnetic field, $\mathbf{D}$ is the displacement field, $\mathbf{B}$ is the magnetic induction field, $\mathbf{J}$ is the current density, and ρ is the free charge density. The electric and magnetic field intensities can be related to the electric and magnetic displacement fields with the constitutive relations (assuming simple, homogeneous, isotropic dielectric materials and magnetic materials at low frequencies):

$$\mathbf{D} = \epsilon \mathbf{E} \tag{1.5}$$

$$\mathbf{B} = \mu \mathbf{H} \tag{1.6}$$

where ϵ is the electric permittivity and μ is the magnetic permeability. While Maxwell's equations precisely describe the interaction between electromagnetic radiation and matter, these equations are often difficult to solve for all but the most ideal scenarios, requiring the use of computational or numerical methods.

1.2 Overview of Photonic Crystals

1D and 2D Photonic Crystals

1D PhCs in the form of multi-layer dielectric stacks have been studied since 1887, when Lord Rayleigh first demonstrated the concept of a 1D optical band gap in such a stack. These are often referred to as a Bragg mirror or a distributed Bragg reflector (DBR). Within a DBR, partial reflection occurs at each material interface. Through careful design of the material choices and layer thicknesses, interference of light reflected within the different layers can provide a desired optical response through interference (Figure 1.1) [2]. DBRs are still an extremely common component of modern day optics.

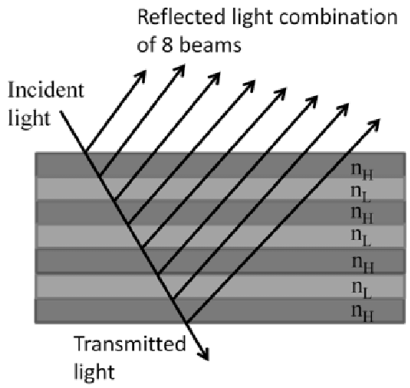

Figure 1.1: Schematic of DBR within which reflection at each interface leads to constructive and destructive interference throughout the DBR, generating the desired optical response. [2]

Depending on the context and application, PhCs can also be studied as diffraction gratings, in 1D or 2D, with the primary subtle distinction being the direction of the grating vector relative to that of the incident wave. Diffraction gratings are a very familiar optics problem that make up a fundamental part of optics. Any light incident on the grating is scattered and split into multiple beams that are either reflected or transmitted, given by the grating equation:

$$d \sin \theta = n\lambda \tag{1.7}$$

where n is an integer denoted the order number, λ is the wavelength of the incident wave, d is the grating periodicity, and θ is the angle of incidence with respect to the grating normal. For diffraction gratings, the diffraction order can be positive or negative, with the "zeroth order mode" ($n = 0$) corresponding to no diffraction in which either specular reflection or direct transmission of the light wave occurs, much in the same way that it would behave with a mirror or lens. Each subsequent order corresponds to light waves that are diffracted at increasingly greater angles.

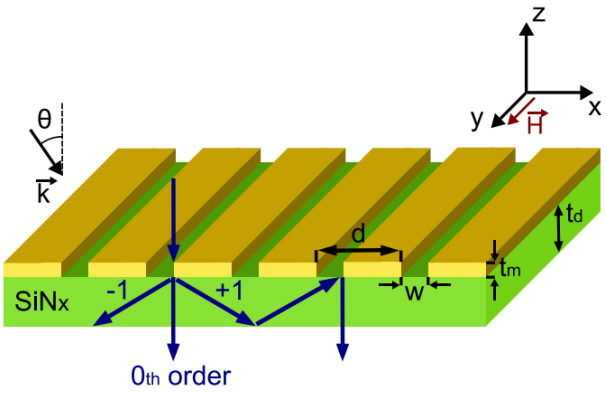

Figure 1.2: Schematic of GMR phenomenon where higher diffraction orders are waveguided until they are eventually re-radiated. Adapted from [3] © The Optical Society.

As the periodicity of a diffraction grating is reduced to the subwavelength regime, where the periodicity approaches the order of the wavelength of the incident wave, only the zeroth order mode propagates in the far field, and all higher orders become evanescent within the grating. In this regime, a resonant phenomenon occurs, often known as a guided-mode resonance (GMR). A GMR occurs when a diffraction grating acts as a phase-matching element, and allows light to be scattered into laterally propagating leaky waveguide modes (Figure 1.2) [3]. This light can subsequently re-radiate back out into the cover or substrate, and manifests itself as a narrowband, near-unity rapid spectral variation [4–6]. This effect only occurs at resonance, at a given incident angle and wavelength. For off-resonance light incident on a grating, light behaves essentially as if no grating was present.

Common terminology that has arisen in recent years to describe the periodic grating structures in which GMRs are observed are zero contrast gratings (ZCGs) [7, 8] and high contrast gratings (HCGs) [9–11]. The difference between

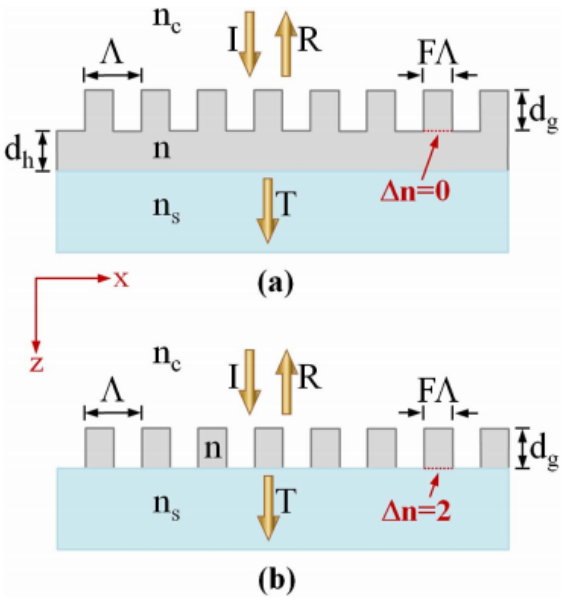

Figure 1.3: Schematic model of GMR devices. (a) Zero-contrast resonant grating structure. (b) High-contrast resonant grating structure. For the examples provided, the devices are made of a partially etched or a fully etched silicon layer with $n = 3.48$ on a glass substrate with $n_s = 1.48$. The cover index is $n_c = 1$ for operation in air. I represents the input plane with unit amplitude, R denotes reflectance, and T transmittance. Adapted from [7] © The Optical Society.

each of these designs is shown in Figure 1.3 [7]. ZCGs contain grating slabs that are placed on top of a homogeneous layer of the same material, such that no reflections or phase changes arise when transitioning from the grating slabs into the homogeneous layer, all surrounded by low-index material (Figure 1.3a). In HCGs, the grating slabs, or high-index material, are completely surrounded by low-index material (Figure 1.3b). In the examples presented in Figure 1.3, the high index grating material is silicon, with a lower index SiO_2 substrate and air cover.

3D Photonic Crystals

In the past, the ability to fabricate PhCs has been greatly limited by available fabrication methods, especially at smaller dimensions. 1D PhCs can be fabricated simply by stacking layers of alternating materials together, while at the macro scale, 2D PhCs can be fabricated by drilling holes into a substrate [12]. At optical length scales, more precise techniques such as photolithography or electron beam lithography may be required to fabricate PhCs. Though lower

dimensionality PhCs have existed and been studied for quite some time, significant interest in 3D PhCs began with the independent work of Eli Yablonovitch and Sajeev John in 1987 [13, 14], 100 years after Lord Rayleigh's report of band gaps in 1D DBR structures, suggesting that periodic variations in dielectric constant can affect the photonic modes of a material, much in an analogous manner to how electron properties are modified by semiconductor crystals. Very similarly to how electronic band gaps in semiconductors prevent the propagation of electrons based on the periodic potential of the crystal lattice, Bragg scattering off of the interfaces of constituent material can produce similarly behaving phenomena for photons, giving rise to the notion of a photonic band gap, or more notably, a full or complete photonic band gap, defined as a range of frequencies over which light cannot propagate in any direction.

Even in recent years, the primary obstacle to the more widespread incorporation of 3D PhCs has been in their fabrication complexity, requiring techniques that are exotic or complex relative to those used for the fabrication of 1D or 2D crystals. As Maxwell's equations possess no inherent length scale, any solutions that exist at larger scales where fabrication is simple should be able to be scaled down to optical length scales. The first theoretical demonstration of a dielectric PhC possessing a complete photonic band gap was demonstrated in 1990 by Ho et al. [15] in dielectric spheres arranged into a diamond structure. Later, in 1991, Yablonovitch reported the first experimental demonstration of a 3D PhC with a band gap, which later became known as Yablonovite: an array of holes drilled into a dielectric material on the centimeter scale where each layer forms an inverse diamond structure, providing a response in the microwave regime [12]. To reach optical length scales with 3D PhCs, fabrication is much more involved and complicated, requiring complex techniques such as layer by layer electron-beam lithography (rod based structures), chemical etching techniques (inverse opals), or direct laser writing (DLW) for more general geometries, to name a few. Due to the complexity of these fabrication techniques, the types of materials that can be used to fabricate these PhCs has to date been quite limited. The realization of 3D PhCs promises many interesting applications in the realm of optics such as photonic circuitry, optical transitors, light capture, or sensing applications, among others.

1.3 Scope of this Thesis

The primary focus of this thesis in its broadest sense is the study of nanophotonics, specifically as it pertains to PhCs in various dimensionalities in dielectric media. We apply these fundamental ideas towards the realization of three different types of nanophotonic structures.

The first type of structure, 1D and 2D PhCs or gratings based off the GMR concept, are explored in Chapters 2-4. In Chapter 2, we report the optical properties obtained through experiments, simulation, and theory of ultrathin, amorphous Si (a-Si) nanopillar arrays based on the HCG architecture with subwavelength periodicity embedded in a thin film of SiO_2 designed for narrowband filtering for multi- and hyper-spectral imaging in the near-IR due to a narrow, near-unity reflectivity resonance. With a combination of full-wave simulations and theory, we demonstrate that these narrowband filtering properties arise from efficient grating coupling of light into guided modes of the array because the nanopillar arrays serve as PhC slabs. We discover that the resonance spectral location is passively tunable by modifying array geometry and is most sensitive to nanopillar spacing. Theoretical PhC slab band diagrams accurately predict the spectral locations of the observed resonance and provide physical insights into and support the guided mode resonance formulation. This work demonstrates that these ultrathin all-dielectric nanopillar arrays have advantages over existing hyperspectral filter designs because they are polarization independent, do not suffer from material absorption loss, and have significant implications for minimizing imaging device size.

While these results were promising, the reliance on a GMR necessitates periodic structures that exhibit a large lateral footprint, often requiring hundreds of periodicities to maintain the high quality factor (Q-factor) of the GMR. To circumvent this issue, in Chapter 3 we introduce a similar design utilizing a grating with only 7 periods but incorporating reflective boundaries at the grating boundaries to emulate an infinite array. The passive tunability of these arrays was explored in a similar manner to their infinite counterparts in full-wave simulations, and fabricated and demonstrated experimentally. These filters present significant improvements in lateral footprint at the cost of small losses in reflection efficiency. To improve the signal-to-noise (SNR) ratio of such a design, we explore a theoretical design in which we reduce noise in the system by removing the reflective mirror boundaries, where each grating

"piggy-backs" off of the periodicity of its neighbor grating.

Though these filters now exhibit lateral footprints, and thus pixel sizes, that are competitive with current state-of-the-art, the finite-based designs possess spectral resolution that is only sufficient for multispectral, rather than hyperspectral imaging. Thus, in Chapter 4, we theoretically explore a design where we utilize a tandem stack of a finite ZCG which exhibits an extremely high Q-factor GMR with undesirable sidebands, with a wideband ZCG reflector to isolate the desired GMR peak. We demonstrate how a superpixel consisting of many narrower peaks from finite ZCG filters can be formed under the relatively broad passband of the other filter.

In Chapter 5, we transition to the exploration of 3D PhCs. Specifically, we present a template-free route to utilize an additive manufacturing (AM) process to directly fabricate nanocrystalline rutile titanium dioxide (TiO_2) 3D PhCs (although any arbitrary geometry is possible) based on DLW with ∼100 nm resolution. TiO_2 was chosen as the model material as a proof-of-concept, though the key is that a similar chemistry can be used to print many different types of materials. For our applications, we were interested in the ability to print high index materials, and explore the applications that such a structure would enable. Notably, AM has previously been limited by its unability to print high index materials. Thus, the second of the aforementioned nanophotonic structures that we explore is a TiO_2 woodpile structure. These woodpile structures are fabricated with two-photon lithography (TPL) followed by a pyrolyzation process, and characterized to confirm that they are indeed TiO_2 structures. We design these structures with plane wave expansion (PWE) simulations and match generated band structures to experimentally measured band gaps. The key of this work is that it provides an ability to print many different materials (in this case with the focus of achieving high index). While we focus on the model material TiO_2, this process is easily amenable to many other materials as well.

Finally, in Chapter 6, we explore a possible implication of the work on 3D TiO_2 PhCs, which leads us to the third of the aforementioned structures to be discussed in this thesis: 3D PhCs that exhibit all-angle negative refraction (AANR) in the mid-IR based on dispersion engineering. To enable a 3D PhC that exhibits AANR, the constituent material must also have a very high refractive index. While the AM technique that will be introduced in 5 will

eventually enable such an application, in this work, 3D polymer-germanium core-shell structures are fabricated with a much more complicated procedure. The structures are designed based on their band structure and fabricated with a combination of TPL and sputtering. The fabrication of such a structure requires significant complexity, and is unrealistic for commercialization. However, its fabrication would be greatly facilitated by the development of an AM process that could enable DLW of high index materials.

Chapter 2

POLARIZATION-INDEPENDENT, NARROWBAND, NEAR-IR SPECTRAL FILTERS VIA GUIDED MODE RESONANCES IN ULTRATHIN A-SI NANOPILLAR ARRAYS

2.1 Introduction

Spectral imaging allows for noncontact sensing and object differentiation based on molecular chemical information by dividing the spectrum into many spectral bands based on the unique spectral signatures of different objects. This is extremely powerful as every chemical species in existence emits a unique spectral signature that can be identified and used to differentiate them from one another. Spectral imaging has been proposed for a wide range of applications such as environmental tracking (oil spills, hazardous waste, atmospheric pollution) [16–19], mineralogy [20], mine detection [21], biology and medicine [22, 23], food inspection [24–26], and surveillance [27], among others [28–32].

Attaining the hyperspectral regime for imaging applications is non-trivial, and necessitates a set of narrowband filters that provide high spectral resolution. High in-band reflection/transmission through these filters is also ideal for high-sensitivity imaging. Furthermore, minimizing the total thickness of an imaging device enables more compact devices and improved imaging performance. Greater thicknesses result in a greater distance for optical crosstalk to occur and a decrease in imaging device performance, since as the lateral size of a pixel (and thus the lateral size of the microlens) decreases, the total filter/circuitry stack in a pixel must also decrease to ensure that the focal length of the microlens is smaller than the focal length of the imaging lens [33, 34].

Conventionally, absorption filters and dichroic/interference filters are used to obtain these desired spectral characteristics. Absorption filters tend to suffer from ultraviolet or high-temperature degradation in the long term and form relatively broad bandwidths. Interference filters permit more precise control and narrower bandwidth than their absorption counterparts, but these interference filters have a large footprint, which typically necessitates scanning imaging methods, and have a total thickness of >1 μm consisting of 10's to 100's of layers of alternating materials that require a complicated and expensive

fabrication process [35].

To compare the performance of filters that operate in different wavelength regimes to one another in this work, we quantify the filter spectral resolution, i.e., bandwidth, using $\Delta\lambda/\lambda$, which is the full width at half-maximum (FWHM) divided by the peak wavelength, as bandwidths tend to be narrower at shorter wavelengths. Interference filters currently represent the commercial standard, which can achieve narrow near-unity pass/stopbands with $\Delta\lambda/\lambda$ on the order of 10^{-2} enabled by their large footprint, thickness, and fabrication complexity.

Many plasmonic-based designs, such as subwavelength nano-rod/hole arrays [36–38] or metal-insulator-metal (MIM) arrays [39, 40], have been explored for color and other spectral filtering because they have the potential to be small footprint and can exhibit an optical response in the visible and IR ranges, but these plasmonic-based designs are known to exhibit significant loss due to the materials used, which leads to low filtering efficiencies [28, 29, 41]. In one plasmonic demonstration, Xu et al. created MIM stacked arrays consisting of 100 nm thick ZnSe sandwiched between two 40 nm thick Al layers, which allowed them to obtain a $\Delta\lambda/\lambda$ as low as 10^{-1} and a transmission of $\sim$40-60% with filter area dimensions of 10 μm x 10 μm [39].

With the use of nanophotonic design principles, a dielectric-based design offers the same potential for small pixel sizes as metal-based plasmonic designs, while minimizing material losses due to insignificant absorption. Appropriately designed dielectric subwavelength 1D gratings and 2D pillar arrays exhibit narrowband near-unity spectral variations at normal light incidence, which make them particularly useful in filtering applications [42–46]. Niraula et al. reported a near-unity band in a dielectric design, with a $\Delta\lambda/\lambda$ of 3.7 x 10^{-4} centered at 1304 nm with a 272 nm thick patterned periodic c-Si layer on a 248 nm thick slab layer of the same material [45]. However, it is worth noting that these high-performance filter designs that have previously been reported usually require thicknesses on the order of 1 μm.

In dielectric subwavelength arrays, only specular reflection and transmission are observed outside the grating without any higher order diffraction or reflection/transmission efficiencies, which gives rise to very narrow, near-unity bandwidths. These particular spectral features are passively tunable via geometric variation of the array over a large spectral range, which is advantageous for the simultaneous production of many filters which cumulatively form a much

larger contiguous spectral band desired for hyperspectral imaging. A number of theoretical explanations for these spectral features have been discussed in the literature, including the interference of axially propagating waveguide modes [9, 47, 48], interference of periodic scatterers [49], and guided mode resonances [4–6]. The first approach approximates the resonance to be created by two interfering axially propagating waveguide modes, and the narrowband resonances arise from their constructive and destructive interference [9, 47, 48]. Magnusson et al. demonstrated that this approximation breaks down for gratings with an antireflection layer deposited at the transmission interface or for systems with very thin structures that exhibit resonances beyond the cutoff point of the waveguides [7]. This resonance effect has also been described by treating the observed resonance with analytical Mie theory as the result of interfering electric and magnetic dipole modes in an infinite array of weakly coupled dielectric scatterers [49]. The lattermost formalism describes a GMR, where periodic design enables an incident light wave to couple into a guided mode within the array via a grating vector, then which also allows re-radiation into the cover or the substrate [4–6]. Sturmberg et al. attempted to reconcile some of these different formalisms by developing an analytical formulation of these spectral features as a Fano resonance, indicated by an asymmetric spectral line shape, in a 1D slab array that arises from the interference between an axially propagating Fabry-Perot mode and an in-plane propagating grating vector-coupled waveguide mode [50]. However, this theory is only valid for arrays with a fill fraction near unity, as it approximates the array as a homogeneous slab with an effective index and loses accuracy the further the fill fraction of high-index material decreases. The GMR formalism is universally applicable in describing the observed near-unity narrowband reflection/transmission peaks of subwavelength periodic structures without requirements such as high fill fraction or sufficiently thick waveguide layers to be valid, and thus, it is the formalism we use for this study.

2.2 Design and Optimization of Nanopillar Filters

We report the optical properties of ultrathin ($<0.1\lambda$) amorphous Si (a-Si) ($n \approx 3.5$) nanopillar arrays embedded in SiO_2 ($n \approx 1.4$) designed to perform narrowband filtering for multi- and hyper-spectral imaging applications in the near-IR, supported by experiment, simulation, and theory. In addition to their low loss relative to plasmonic designs, these all-dielectric nanopillar arrays also

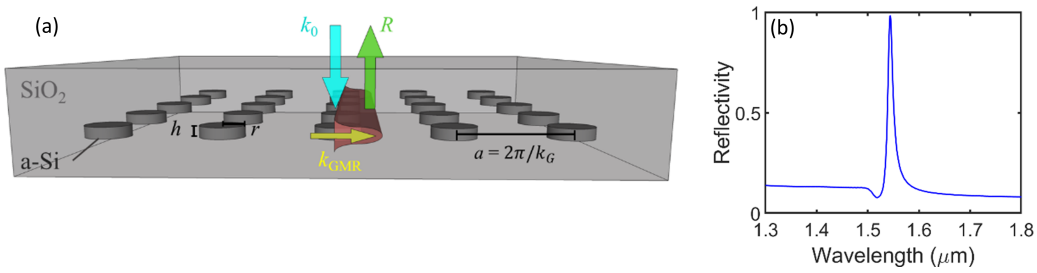

Figure 2.1: a-Si nanopillar array schematic and optical response. (a) Schematic of a 2D subwavelength a-Si nanopillar array embedded in glass that exhibits a GMR under normal incidence illumination. The a-Si nanopillar layer has a thickness, h, radius, r, and periodicity, a. The GMR phenomenon is illustrated: incident light with wavevector k_0 couples into a guided mode with propagation constant k_{GMR}, via a grating vector k_G and is reradiated into the cover. (b) Simulated reflectivity spectrum for such an array with $h = 100$ nm, $r = 210$ nm, and $a = 1050$ nm.

possess the advantage of polarization independence due to their 2D periodicity.

The design presented in this work possesses experimental filter performance on par with many existing plasmonic or dielectric designs while also possessing the advantage of being only ∼100 nm thick. Figure 2.1a displays a schematic of the a-Si nanopillar arrays embedded in SiO_2 along with a visual representation of the GMR phenomenon. The nanopillar thickness/layer height, radius, and array periodicity are denoted by h, r, and a, respectively. A representative GMR reflectivity spectrum for such an array is shown in Figure 2.1b. Our choice of a-Si stems from its low cost, high refractive index, and band gap of 1.55 eV that lies near the edge of the visible spectrum and renders it lossless in the near-IR. While arrays in this work operate in the near-IR, this design can be more generally applied over a broad spectral range via appropriate geometric design, beginning from the band gap of a-Si through the mid-IR where the phonon resonances of a-Si begin to occur. A high index of refraction increases the ability of the nanopillars to scatter light that passes through. As the scattering strength increases (via either a higher nanopillar index or fill fraction), both the peak amplitude and the bandwidth of the observed resonance increase. Embedding these a-Si nanopillars into a SiO_2 film allows for these filters to easily be integrated into an imaging device. This work enriches the existing body of literature on 1D and 2D dielectric arrays [4–7, 9–11, 42–44, 47, 50–75] by offering a comprehensive study of polarization-independent, near-unity, narrowband filters, including theory, simulation, and experimental

demonstration.

In this work, full-field, 3D simulations were computed with Lumerical finite-difference time domain (FDTD), a commercial electromagnetics software package. In this chapter, all simulations utilized single broadband simulations from 1300-1800 nm. At normal incidence, symmetric and antisymmetric boundary conditions were used on the lateral boundaries to emulate infinite periodicity. For simulations at off-normal incidence, Bloch boundary conditions were applied that apply a phase correction to the fields in adjacent periods. In all cases, perfectly matched layers were used for the axial boundaries as an artificial absorbing region to emulate infinite space. For the materials in the simulation, Palik data was used for SiO_2 and ellipsometric data was used for a-Si (Figure 2.2). Ellipsometry n,k data was obtained for 100 nm thick a-Si deposited in PECVD at 200 °C, 800 mTorr, and 10 W with 250 sccm of 5% SiH_4 diluted in Ar. This n,k is input into the FDTD simulations. A finer override mesh was applied over the a-Si nanopillar with mesh sizes of <5% the height and radius of the nanopillars. For all reflection and transmission calculations in FDTD in this chapter, a Fresnel correction was applied to account for the additional material interfaces not directly accounted for in simulation (derivation in Appendix A.1):

$$R_{03} = \frac{R_{01} + \left(\frac{R_{12}+R_{23}}{1+R_{23}R_{12}}\right)}{1 + \left(\frac{R_{12}+R_{23}}{1+R_{23}R_{12}}\right)R_{01}} \tag{2.1}$$

where R_{ij} is the reflectivity between layers i and j. This equation is applied for a 4 layer stack of (air-SiO_2-SiO_2-air), where the reflectivity obtained from simulation of the nanopillar array is treated as R_{12}, the SiO_2-SiO_2 interface. The other air-glass interfaces can be calculated with the normal Fresnel equations assuming a refractive index of $n = 1$ for air, and $n = 1.44$ for SiO_2.

Describing the resonance phenomenon that occurs in our 2D dielectric nanopillar design using a GMR formulation, in which incident light couples into waveguide modes of a PhC slab, the phase matching condition that allows for an incident wave to couple into a guided mode via a grating vector can be expressed as [50]:

$$k_{GMR} = k_0 \sin\theta + mG = k_0 \sin\theta + \frac{2\pi m}{a} \tag{2.2}$$

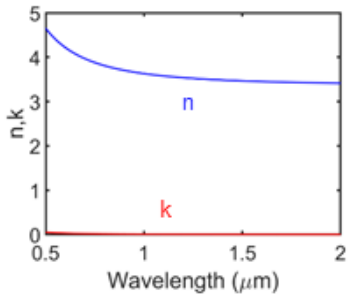

Figure 2.2: Raw n and k data for a-Si model used for FDTD simulations determined from ellipsometry for a 100 nm thick film of a-Si deposited via PECVD

where k_{GMR} is the propagation constant of the waveguide mode, k_0 is the incident wave vector, m is the grating order (m = 0,1,2...), θ is the incident angle, and G is the reciprocal lattice vector.

The GMR phenomenon can be validated using PhC slab band structure diagram calculations [9, 65]. To illustrate this, Figure 2.3 shows a comparison between band structure and the associated reflectivity spectra generated by FDTD numerical simulations. Figure 2.3a shows the FDTD reflectivity spectra for a nanopillar array with r = 210 nm, a = 1050 nm, and h = 100 nm under various incident illumination angles that vary from 0° (orange) to 20° (dark blue) in 5° increments for p-polarization. These were calculated as single-wavelength simulations. Figure 2.3b contains the PhC slab band structure in the first Brillouin zone, which shows normalized frequency, k_0/K, vs the normalized wave vector, k_{GMR}/K, where $K = 2\pi/a$ for the same nanopillar array and the same incident illumination angles as shown in Figure 2.3a. The corresponding light lines for each illumination angle are also shown in the plot in self-consistent color. The PhC slab band diagram was generated using Lumerical FDTD, following the methodology described in their planar 3D example for PhC band structure. The band structure was modeled for a 2D infinite a-Si nanopillar array with the aforementioned geometric parameters, embedded in SiO_2. A 5 nm mesh was used in each direction, and the structure modes were identified between 100 and 240 THz along the Γ-X direction. The GMR peak locations from FDTD simulations (Figure 2.3a) were then converted into frequencies and plotted along the light line for each incident wave on the PhC band structure (colored squares in Figure 2.3b). These peaks coincide with the intersections between the light lines and dispersion modes, as expected. Following this

procedure for every incident angle allows us to accurately trace out the full band and indicates that the dispersion relation accurately predicts the location of the GMR and supports the GMR formalism.

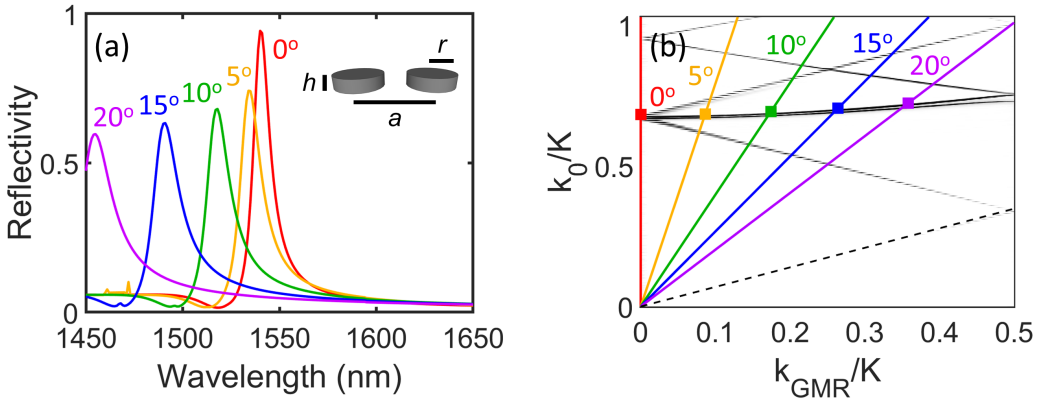

Figure 2.3: Dispersion of a-Si nanopillar array. (a) FDTD simulations of reflectivity spectra for an a-Si nanopillar array with geometrical parameters of $r = 210$ nm, $a = 1050$ nm, and $h = 100$ nm under an incident illumination angle that varies from 0° (orange) to 20° (dark blue) in 5° increments for p-polarization. (b) Simulated PhC slab band diagram of this a-Si nanopillar array in the first Brillouin zone. The dashed gray line represents the substrate light line. The peak locations of resonances from the simulated reflectivity spectra under varying incident angle are indicated by squares and coincide with the intersection between the light lines for the corresponding incident angle and the modes in the dispersion; color scheme is consistent throughout the figure.

Under normal incidence, this pillar array has a band gap between the modes around the frequency of the observed reflectivity peak. While the observed near-unity reflections may appear to be a PhC band gap effect in the context of a periodic system, this cannot be the case, as the bandwidths of the simulated GMRs are too narrow to span an entire band gap on the dispersion and the reflection peaks clearly follow the upper band rather than the center of the gap when angles other than normal incidence are considered. Additionally, the observed reflection corresponds with specular transmission, or zeroth-order diffraction, in a subwavelength array. The first-order diffraction point occurs at 1512 nm ($a^*n_{SiO_2}$, where n_{SiO_2} denotes the refractive index of SiO_2) for the array represented in the band structure in Figure 2.3, as opposed to the observed reflection at 1540 nm, indicating the observed reflection is not a result of higher order diffraction. The presence of a reflection band is determined by whether the counterpropagating waves of the guided mode in the grating

are π out of phase, which quenches radiation, or in phase, which enhances radiation [64, 73]. An edge at which radiation is enhanced is known as a leaky edge, and its existence depends on factors such as the physical array profile and the index contrast between the array and its cover and substrate. For the array presented here, the GMR occurs as a result of the top band edge being leaky. Thus, the band structure provides a wealth of information with regard to predicting GMR location and building a physical description of how these GMRs arise.

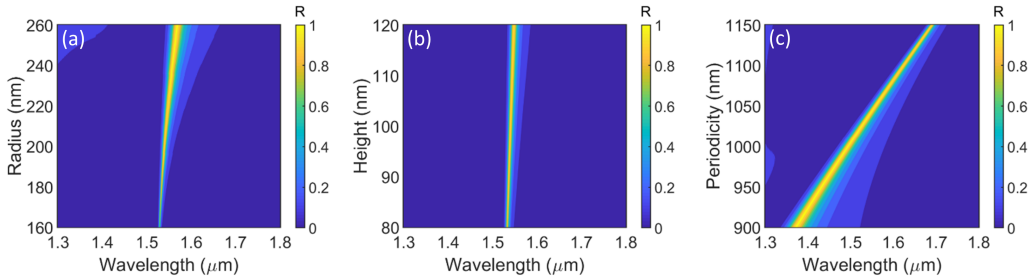

Figure 2.4: Intensity plots of simulated reflectivity (color axis) vs wavelength (x-axis) and structure dimensions (y-axis): (a) $h = 100$ nm, $a = 1050$ nm, variable r; (b) $r = 210$ nm, $a = 1050$ nm, variable h; (c) $h = 100$ nm, $r = 210$ nm, variable a.

This theory can be further generalized to nanopillar arrays with different dimensions and spacings, which offers control of spectral characteristics such as the GMR spectral location, amplitude, and bandwidth or FWHM of the reflectivity resonance. To gain insights into the sensitivity of the resonance to changing nanopillar array dimensions, we conducted FDTD simulations in the near-IR, in which we individually varied parameters r, a, and h one at a time while holding the others constant. The results of these simulations are presented in Figure 2.4, which shows the effect of individually varying each of these parameters on the reflection spectra of the nanopillar array. A change in the radius or periodicity affects k_{GMR} by changing the waveguide dispersion and thereby influencing the phase-matching condition in Equation 2.2. Increasing the radius (Figure 2.4a) and height (Figure 2.4b) causes the GMR to red-shift, broaden, and increase its amplitude because larger nanopillars are stronger scatterers. Increasing periodicity (Figure 2.4c) also red-shifts the GMR due to the change in grating vector and decreases its amplitude, but causes it to narrow. The array serves as a waveguide with a thickness that is the height of the pillar, h. Changing the thickness of this waveguide region affects the

waveguide modes and thus the resonance. When radius, height, and pitch each increase by 10% from the nominal values of $r = 210$ nm, $h = 100$ nm, and $a = 1050$ nm, a spectral shift of 9.9, 0.9, and 154.2 nm is observed, respectively. This observation demonstrates that pillar spacing is the most powerful handle in controlling the peak location of the GMR. The observed resonance corresponds with the zeroth-order mode. As the wavelength of the incident propagating wave decreases, additional higher order modes become available, which introduce additional resonances. The onset of the next order mode is observed at lower wavelengths in Figures 2.4a and 2.4c. These results indicate that it is possible to easily control the spectral characteristics of the GMR, allowing for significant design flexibility in creating a filter.

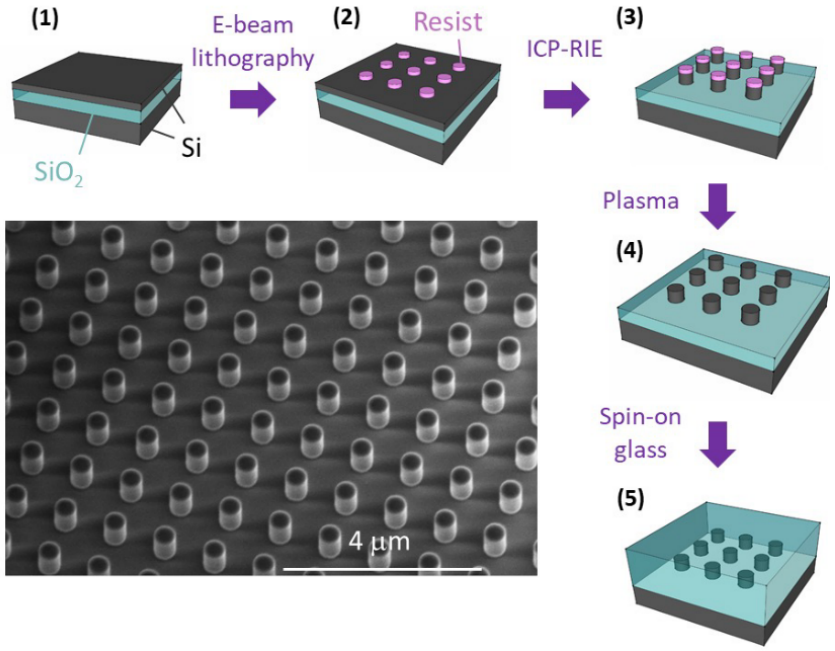

Figure 2.5: Schematic of fabrication process for nanopillar arrays on SOI and associated SEM image of array prior to applying spin-on glass.

2.3 Experimental Fabrication and Verification

The original fabrication procedure for these filters utilized a silicon-on-insulator (SOI) substrate, with a 220 nm thick device layer, 3 μm thick oxide layer, and 675 μm thick substrate due to the simplicity of such a fabrication procedure. The device layer in this fabrication procedure consists of c-Si, as opposed to a-Si, which exhibits a band gap closer to 1.1 eV. A schematic illustrating this fabrication process and an associated SEM image of the nanopillars prior

to incapsulation in SiO_2 are shown in Figure 2.5. The final pillar height is determined via the thickness of the device layer. First, the device layer is thermally oxidized then etched in buffered HF down to the desired pillar height. This surface is patterned in e-beam lithography with a 5 nA beam current and a 610 $\mu C/cm^2$ dosage with 200 nm thick MaN-2403 negative tone resist which serves as an etch mask. The pattern is then transferred through the entire device layer down to the oxide layer by inductively coupled plasma reactive-ion etching (ICP-RIE) with a pseudo-Bosch etch [76]. Following etching, the resist etch mask is removed in an oxygen plasma. Finally, to maintain no index contrast between the substrate and the cover, 500 nm of a methylsiloxane spin-on glass (Filmtronics) optimized for gap-filling is applied to the surface to fully encapsulate the nanowire array.

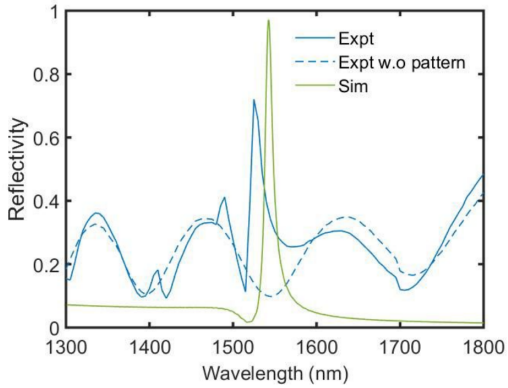

Figure 2.6: Reflectivity spectrum for a nanopillar array with dimensions $r = 210$ nm, $a = 1050$ nm, $h = 100$ nm for experiment (solid blue line) and simulation (solid green line). Fabry-Perot interference is observed in experiment confirmed by comparison to a spectrum taken on the substrate without a nanopillar array (dashed blue line).

Reflectivity of these experimentally fabricated arrays on SOI were measured and compared to FDTD simulations (Figure 2.6). Measurements were made with a Fianium white light source coupled to a near-IR monochromator with Ge photodetectors. Reflection measurements were taken from 1300 to 1800 nm spaced evenly 1 nm apart from one another. To determine absolute reflectivity at each point, a pair of Ge photodetectors simultaneously recorded the intensity of the beam reflecting off of a sample, I_{ref}, and the intensity of the incident beam, I_{inc}, separated by a beamsplitter. This was normalized by the same quantity reflecting off of a silver mirror. The absolute reflectivity, R, was then calculated by:

$$R = \left(\frac{I_{\text{ref}}}{I_{\text{inc}}}\right)_{\text{sample}} \left(\frac{I_{\text{inc}}}{I_{\text{ref}}}\right)_{\text{mirror}} \tag{2.3}$$

For the filters fabricated on SOI substrates, the GMR exhibits a reflectivity of 71%; the peak position of the array in experiment is slightly blue-shifted from the value in simulation (peak position is located at 1525 nm against 1542 nm in simulation), with a measured FWHM of 24 nm in experiment vs 11 nm in simulation. The amplitude of the experimental reflectivity peak is a factor of 1.36 lower compared with the simulation, likely due to energy lost to the Fabry-Perot interference evidenced by the oscillatory behavior, resulting from the presence of theunderlying silicon layer with higher index relative to that of the oxide layer that encompasses the array. To confirm that this effect is, in fact, Fabry-Perot interference, we also measured the reflectivity on a region of the as-fabricated sample where no silicon array pattern is present. As expected, these measurements revealed fully present oscillations, but no GMR.

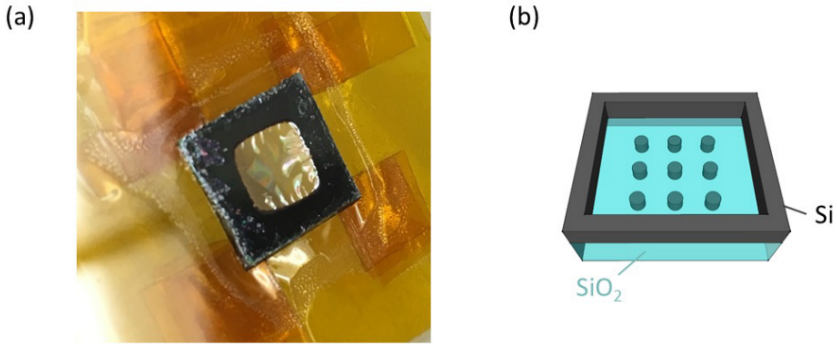

Figure 2.7: Camera image (a) and schematic drawing (b) of free-standing film containing nanopillar array with silicon supports following etching through the backside silicon substrate.

We hypothesized that removal of the underlying silicon substrate would eliminate the Fabry-Perot interference, thus reducing energy loss and maximizing the amplitude of the GMR. Etching through a 675 μm-thick substrate layer while maintaining the integrity of the thin oxide containing the array limit the use of wet chemical etchants. Instead, we used ICP-RIE to etch through the entirety of the underlying silicon wafer within the rectangular area shown in Figure 2.7. The SOI chip is taped face down onto a glass slide with Kapton tape, with the substrate side facing up (Figure 2.7a). The Kapton tape serves a double purpose by also masking the edges of the taped substrate, while the center underneath the pattern is etched away. As the etch nears the thin

oxide layer, care must be taken as over-etching ruptures the thin oxide layer. The resulting structure is a 3.5 μm SiO_2 film bounded by silicon supports (schematically shown in Figure 2.7b). The different stiffness between Si and SiO_2 cause the oxide film to wrinkle upon its release from the silicon, which renders measuring specular reflectivity impossible due to significant scattering on the non-flat surface.

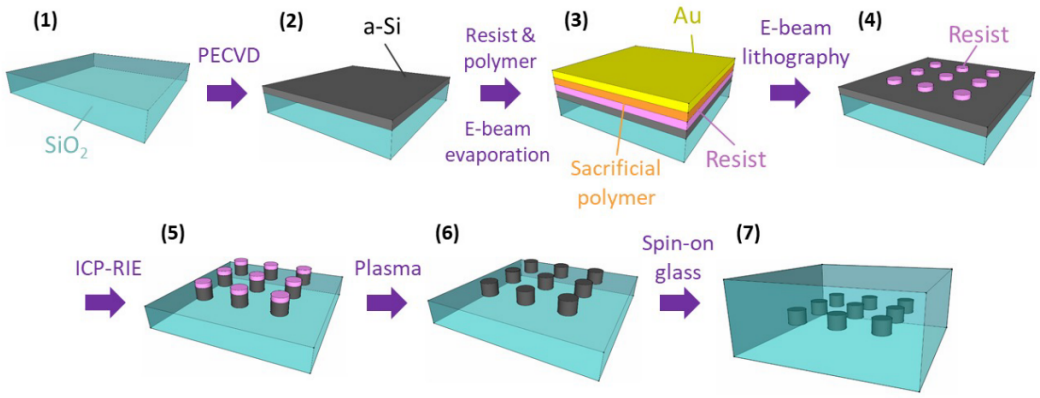

Figure 2.8: Schematic of fabrication process for nanopillar arrays on a-Si.

To circumvent this challenge, we developed an alternative fabrication process using a top-down methodology on a glass substrate without an underlying silicon layer (Figure 2.8) [74]. Approximately 120 nm of a-Si was deposited onto the substrate by PECVD at 200 °C, 800 mTorr, and 10 W with 250 sccm of 5% SiH_4 diluted in Ar for 4 min. The thickness deposited in PECVD dictates the height of the nanopillars in the array in this fabrication scheme. Next, MaN-2403 negative-tone electron beam resist was applied onto the a-Si. A sacrificial layer (a solution of poly(4-styrenesulfonic acid) mixed with 1% by volume of Triton X-100 surfactant) was spin-coated above the resist, followed by 10 nm of thermally evaporated Au to improve conductivity for charge dissipation prior to EBL. Without this step, due to the electrically insulating nature of the underlying glass substrate, significant drifting in adjacent fields in the e-beam are observed. While existing commerical solutions exist that serve a similar purpose, these solutions tend to be extremely expensive. The Au was not directly applied above the resist due to chemical incompatibility between the gold etchant and the electron beam resist, leading to washed out features, though this technique is often also viable [77]. The desired pattern was exposed with a Raith 5200 electron beam writer with a 100 kV electron source with a 5 nA beam and 610 $\mu C/cm^2$ dose. Following electron beam exposure, the

sacrificial polymer and gold were easily removed by rinsing in water, and then the pattern was developed in MF-319 for 1 min and transferred into the a-Si layer with a pseudo-Bosch SF_6/C_4F_8 etch with ICP-RIE at 10 °C with 25 W ICP power, 600 W forward power, 22 sccm of SF_6, and 30 sccm of C_4F_8 [76]. The resist mask was removed by cleaning in an oxygen plasma for 10 min (20 mTorr with 20 sccm O_2). The nanopillars were in-filled with 800 nm of SiO_2 by deposition via PECVD at 350 °C, 1000 mTorr, and 20 W with 710 sccm of N_2O and 170 sccm of 5% SiH_4 diluted in Ar for 11 min to ensure a good match to the index of the underlying glass. Finally, this surface was planarized to minimize potential scattering at the rough surface by application of 500 nm of methylsiloxane-based spin-on glass solution (Filmtronics 500F).

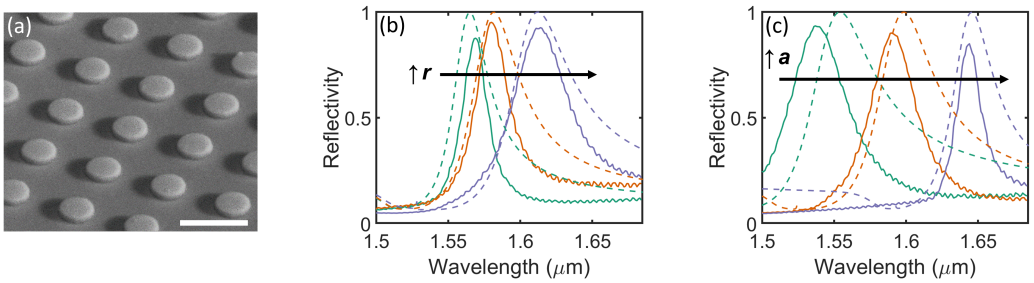

Figure 2.9: Experimental results of a-Si nanopillar array. (a) Scanning electron microscope image of a nanopillar array coated with 10 nm of Pd to improve imaging. Scale bar is 1 μm. (b) Reflectivity spectra: experiment (solid lines) and FDTD simulations (dashed lines) of as-fabricated a-Si nanopillar arrays with h = 100 nm, a = 1050 nm, and r = (240 nm, 297 nm) (green), (269 nm, 327 nm)(orange), and (303 nm, 378 nm) (blue); and (c) $r \approx$ 263-302 nm with a = 1000 nm (green), 1050 nm (orange), and 1100 nm (blue) where the pairs are given as the top and bottom radius of the pillars to describe their slight vertical taper. The dashed lines indicate simulations; the solid lines are experimental spectra. The simulations account for tapering of the pillars. Dimensions for the tapered pillars are measured in atomic force microscopy

With this fabrication methodology, we fabricated three a-Si nanopillar arrays with varying radius and three arrays with varying periodicity and measured their specular reflection to verify the self-consistent theoretical and computational results of section 2.2 experimentally. Figure 2.9a displays a scanning electron microscope (SEM) image of a representative a-Si nanopillar array. A 10 nm thick Pd layer was sputtered on this particular array to provide conductivity for SEM imaging. Figure 2.9b (varying radius) and Figure 2.9c (varying periodicity) display the experimentally measured reflectivity spectra for the

fabricated arrays at normal incidence, overlaid with simulated reflectivity spectra. Measurements were made similar to in Figure 2.6, though here data was only collected from 1500 to 1700 nm spaced evenly in increments of 1 nm.

Table 2.1: Spectral characteristics for each array in experiment / simulation for variable radius and variable periodicity. The color scheme is consistent with that in Figure 2.9.

Variable Radius

Array	Peak Position (nm)	Peak Amplitude	FWHM (nm)
Green	1569 / 1565	87.6 / 99.8	22.4 / 33.4
Orange	1580 / 1582	95.1 / 99.9	31.4 / 45.4
Blue	1614 / 1612	92.6 / 100.0	51.4 / 58.9

Variable Period

Array	Peak Position (nm)	Peak Amplitude	FWHM (nm)
Green	1537 / 1554	93.5 / 100.0	49.9 / 62.8
Orange	1590 / 1598	90.1 / 100.0	40.4 / 54.4
Blue	1644 / 1646	85.0 / 99.9	22.4 / 39.4

The measured reflection peaks in Figure 2.9 demonstrate an experimental observation of the GMR. For optimal hyperspectral performance, the desired peak characteristics for these filters are high reflection efficiencies and small FWHM values. Reflectivities from 85% to 95%, $\Delta\lambda/\lambda$ from $1.37\text{x}10^{-2}$ to $3.24\text{x}10^{-2}$, and FWHM from 22.4 to 51.4 nm are obtained experimentally. To avoid any ambiguity, we define the FWHM in these plots as the bandwidth at half of the maximum amplitude, instead of at half of the amplitude minus the background as it is conventionally defined, because the background intensity is asymmetric due to the Fano lineshape of the GMR. Due to this definition, these FWHM values slightly underrepresent the performance of our filters, since the FWHM is measured lower on the peak where the bandwidth is broader than if a background was subtracted. Spectral characteristics for each of the fabricated arrays measured experimentally are summarized in Table 2.1 in a self-consistent color scheme with Figure 2.9. Despite experimental imperfections, we observe good agreement between the experimental and simulated reflectivities. The slight discrepancies between experiment and simulation likely stem from (1) refractive index differences between material models used in simulation and that of the fabricated devices and (2) natural inaccuracies in AFM measurements of the tapered nanopillars due to minor fabrication complexities. For simulations matched to experimental measurements in Figure 2.9, a tapered cone was used

to model physical tapering of the nanopillar with dimensions determined via AFM measurements. These AFM measurements of the nanopillar profiles are obtained prior to encapsulation in SiO_2, and these scans and their nanopillar profiles are presented in Figure 2.10. These profiles provide the height, radius, and periodicity of the nanopillar arrays. Figures 2.10a-2.10c provide AFM data for variable radius which corresponds with the spectra in Figure 2.9b. Figures 2.10d-2.10f provide AFM data for variable periodicity which corresponds with the spectra in Figure 2.9c.

The slight tapering observed in these nanopillars is characteristic of structures etched in ICP-RIE processes. To emulate experiment, the simulated pillars also had a taper with dimensions matched to experiment, with r_{top} and r_{bottom} representing the pillar radius at the top and bottom of the pillar, respectively. The simulated radii were chosen based on AFM pillar measurements. In Figure 2.9b (varying radius), the nanopillars have $h = 100$ nm, $a = 1050$ nm, and $r_{top,bottom} = 240$ nm, 297 nm (green line), 269 nm, 327 nm (orange line), and 303 nm, 378 nm (blue line). For Figure 2.9c (varying periodicity), the nanopillars have $h = 100$ nm, $a = 1000$ nm, and $r = 302$ nm, 369 nm (green line), $a = 1050$ nm and $r = 287$ nm, 357 nm (orange line), and $a = 1100$ nm and $r = 263$ nm, 338 nm (blue line). While r varies slightly for variable a, the effect of the radial variation is negligible compared to the effect that the periodicity variation has on the GMR (see Figure 2.11). For the sweep in variable periodicity shown in Figure 2.9c, while these nanopillars should have a constant radius, fabrication imperfections cause a slight disparity between the radius in each of these arrays. In Figure 2.11, the effect of a change in radius and a change in periodicity on the GMR peak location is presented. The top radius of the nanopillar in the variable periodicity sweep varies from 263 nm to 302 nm. Over this radius range, we observe minimal shifting of the GMR location at a constant periodicity of $a = 1050$ nm (Figure 2.11a). The GMR locations for each array are 1559 nm (green), 1569 (orange), and 1581 (blue). On the other hand, for variable periodicity, we see a much more significant shift in the GMR location as we vary the periodicity from 1000 nm to 1100 nm which causes the peak to shift with peak locations of 1508 nm (green), 1569 nm(orange), and 1633 nm (blue) in Figure 2.11b. This range of radii and periodicities reflect the range over which the nanopillar arrays exhibited experimentally. Due to the much stronger effect of the periodicity on the GMR location, we assume the radius to be approximately constant for the variable periodicity arrays.

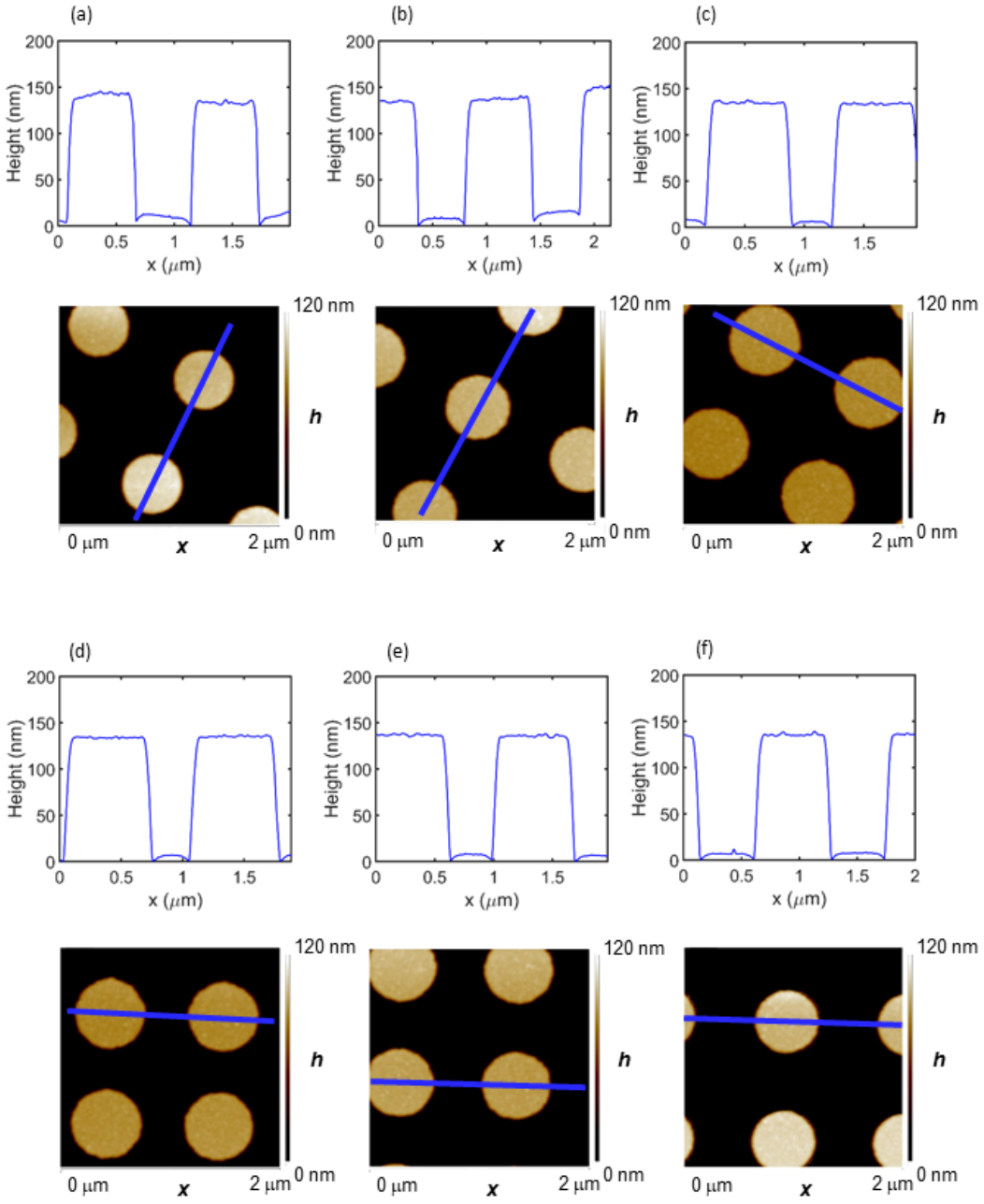

Figure 2.10: AFM profiles of the radius of the tapered wires in Figure 2.9b with variable radius for (a) green spectrum, (b) orange spectrum, and (c) blue spectrum and in Figure 2.9c with variable period for (d) green spectrum, (b) orange spectrum, and (c) blue spectrum.

2.4 Conclusions

We fabricated ultrathin a-Si nanopillar arrays embedded in a continuous SiO_2 matrix that demonstrate narrow-band, passively tunable, near-unity reflectiv-

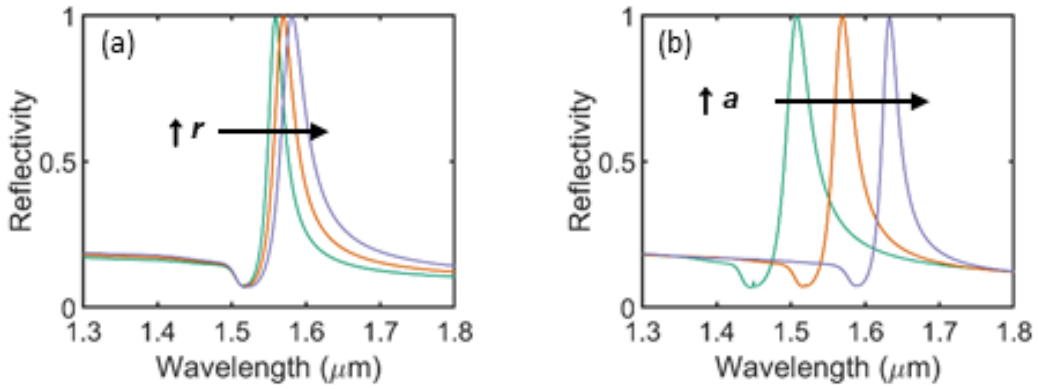

Figure 2.11: FDTD simulations for (a) $a = 1050$ nm, $r = 260$ nm (green), 280 nm (orange), 300 nm (blue) and (b) $r = 280$ nm, a = 1000 nm (green), 1050 nm (orange), 1100 nm (blue).

ity peaks, which renders them particularly useful for hyperspectral filtering applications in the near-IR. The design and the fabrication process are simple compared to existing polarization-independent-based designs, requiring a single nanopatterned layer and a single lithography step. These filters are efficient and have a high spectral resolution, while being much thinner than most existing designs. Using a combination of band structure theory, FDTD simulations, and reflectivity experiments, we demonstrate that these narrow reflectivity peaks arise from GMR effects and provide insights toward a full understanding of 2D subwavelength arrays. We explored the effect of varying geometric parameters of the nanopillar arrays to passively tune the GMR to obtain desired spectral characteristics. The demonstrated existence and tunability of this GMR opens up a substantial new design space for creating hyperspectral filters for imaging applications.

Chapter 3

MINIATURIZATION OF GUIDED MODE RESONANCE FILTERS

3.1 Introduction

While GMR-based filters possess high resolving power, this comes with the requirement of a significant number of periods, leading to lateral footprints and thus pixel sizes on the order of 10s to 100s of microns in the IR, much too large to provide high spatial resolution in an imaging system, an effect that has previously been studied [78–82]. This relationship between Q-factor/spectral resolving power and lateral periodicity is a typical trade-off for filter designs consisting of periodic structures [83].

Specifically, in GMR-based designs, many periods are required as once an incident light wave is scattered by the periodic array into a laterally propagating waveguide mode, it must propagate for a sufficient number of periods until it scatters back out, manifesting as the GMR phenomenon. In a finite lattice, if the laterally propagating mode reaches the array edge prior to scattering out, this mode can couple into fully guided modes in the bulk material, and this energy is lost. Thus, high Q-factor modes often are not observable in finite lattices with an insufficient number of periods [82]. These edge loss effects can be suppressed to emulate infinite periodicity via the incorporation of reflective boundaries outside the array such that the array essentially unfolds into an infinitely periodic structure and these fully guided modes in the bulk medium cannot be accessed. This strategy has been incorporated and experimentally demonstrated from the visible through near-IR to be effective for small aperture size GMR designs using DBRs as the reflective boundaries [42, 82, 84–90]. For a spectral imaging system, the many layers required for a DBR greatly increases the lateral footprint. In the radio wave regime, a single reflective mirror was used at each boundary in place of a DBR in an all-dielectric GMR design [91]. In this work, we employ this strategy in the near-IR regime.

3.2 Design and Optimization of Miniaturized Guided Mode Resonance Filters

We report the optical properties of a 1D 7-period compact a-Si (n $\approx$ 3.5) HCG surrounded on two sides with reflective Al mirrors, all embedded in SiO_2 (n $\approx$ 1.4), designed for multi-spectral imaging applications in the near-IR. A schematic of the proposed filter design is shown in Figure 3.1a. In this design, the incident light operates in the transverse electric (TE) polarization state (red text), in which the electric field runs parallel to the length of the grating beams of the filter. As the incident light wave is scattered via the periodicity of the 7-period grating into a laterally propagating leaky waveguide mode, the Al mirrors allow this laterally propagating mode to reflect back and continue propagating until it scatters back out, giving rise to the GMR. The grating slab height, periodicity, fill fraction of high index material (a-Si), and wall height is denoted by h, a, f, and d, respectively. Additionally, a spacer region is incorporated to ensure that the reflected wave is in phase with itself. This spacer, s, is defined as the distance half a period away from the center of the outermost grating slab until the inner mirror edge. To determine the optimal value for these parameters, we utilized nonlinear optimization by mesh adaptive direct search (NOMAD) with FDTD simulations, a method ideal for metamaterial optimization that iteratively alternates between global and local searches [83, 92–94]. From NOMAD, an optimized 7-period filter was found with the parameters $h = 64$ nm, $a = 831$ nm, $f = 0.18$, $d = 61$ nm, and $s = 215$ nm, which was used as the standard design for this work.

In the work in this chapter, full-field, 2D simulations were computed with Lumerical FDTD. For infinite filter simulations, periodic boundary conditions were used on the lateral boundaries to reduce the simulation region and emulate infinite periodicity. For finite simulations, perfectly matched layers were used for the lateral boundaries as an artificial absorbing region to emulate infinite space. In all cases, perfectly matched layers were used for the axial boundaries. For the materials in the simulation, Palik data was used for Al and SiO_2 and ellipsometric data was used for a-Si (Figure 2.2). A finer override mesh was applied over the a-Si slabs with mesh sizes <5% the height and width of the slabs. The spectra in this work utilized single broadband (800-2000 nm) simulations. As before in Chapter 2, a Fresnel correction was applied to all simulations to account for interfaces that were not included in simulation (Appendix A.1). Here, it takes a similar form:

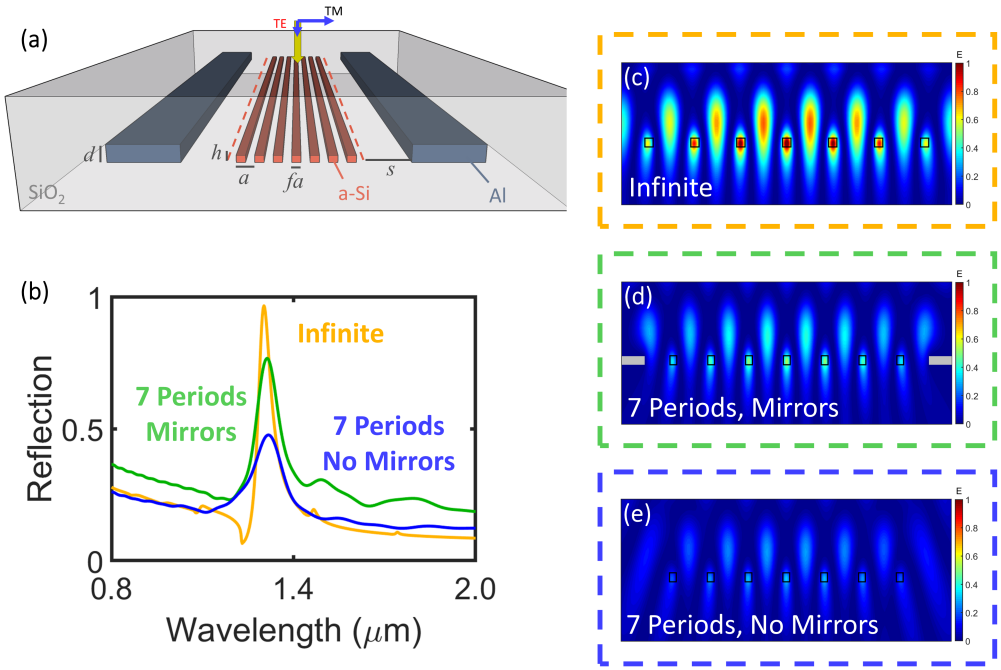

Figure 3.1: Design of 7-period finite HCG. (a) Schematic of the 1D compact a-Si GMR filter with 7 periods of a-Si slabs surrounded by Al mirrors embedded in SiO_2. The array of a-Si slabs has thickness, h, periodicity, a, fill fraction, f, and wall height, d. A spacer region, s, denotes the space between the filter and mirror. The incident light TE polarization state (red text), in which the electric field runs parallel to the length of the grating beams of the filter. (b) Simulated reflectivity spectra comparing the GMR in three different designs: an infinite array (no mirrors), the finite 7-period a-Si slab design with Al mirrors presented here, and a finite 7-period a-Si slab design that does not utilize Al mirrors. Their respective electric field profiles of a cross-section of the filter are given in (c), (d), and (e). The black boxes represent the a-Si slabs, while the grey squares represent the Al mirrors.

$$R_{03} = \frac{R_{01} + \left(\frac{R_{12}+R_{23}}{1+R_{23}R_{12}}\right)}{1 + \left(\frac{R_{12}+R_{23}}{1+R_{23}R_{12}}\right)R_{01}} \tag{3.1}$$

where R_{ij} is the reflectivity between layers i and j. This equation is applied for a 4 layer stack of (air-SiO_2-SiO_2-air), where the reflectivity obtained from simulation of the nanopillar array is treated as R_{12}, the SiO_2-SiO_2 interface. The other air-glass interfaces can be calculated with the normal Fresnel equations assuming a refractive index of $n = 1$ for air, and $n = 1.44$ for SiO_2.

Figure 3.1b shows a comparison of the spectra of three finite filter design

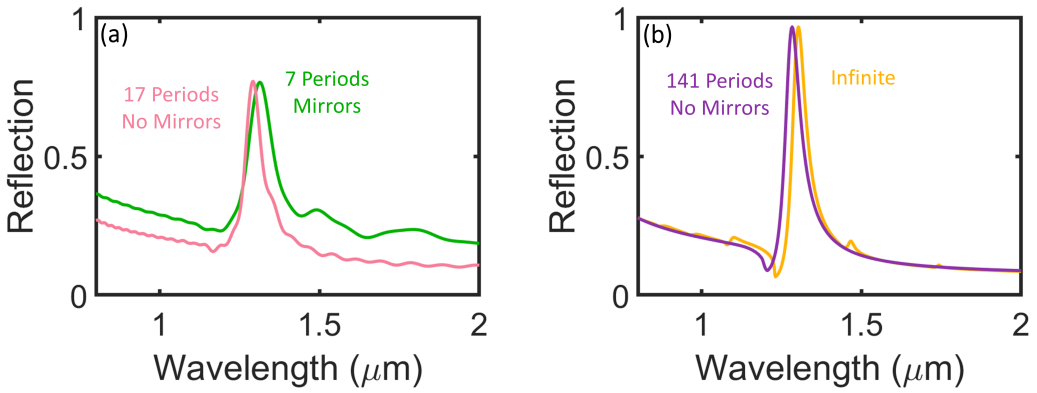

Figure 3.2: Comparison of spectra from FDTD simulations between designs that do and do not utilize mirrors demonstrating the number of periods required in a design that does not incorporate mirrors for it to match the amplitude of another design. (a) Comparison between the finite 7-period design with mirrors (green) with a finite 17-period design that does not incorporate mirrors (pink). (b) Comparison between an infinite design (yellow) and a finite 141-period design that does not incorporate mirrors (purple).

variations that motivate the inclusion of mirrors, generated by FDTD numerical simulations. The scenario depicted in Figure 3.1a with the compact 7-period design with Al mirrors (green) optimized in NOMAD exhibits lower in-band reflection and greater FWHM than the infinite case (yellow), but greater in-band reflection and slightly lower FWHM than the case of a compact 7-period design that does not incorporate Al mirrors (blue). As GMR reflection peaks often possess a Fano line shape, or asymmetric background, we define the FWHM in this work as the bandwidth at half of the maximum amplitude, rather than half of the amplitude minus the background as is conventionally defined, to avoid any ambiguity. This leads to an underestimation in the performance of this design, since the FWHM is reported at a lower reflection value where the peak is slightly broader. To match the peak amplitude of our proposed design or the infinite design using a finite design that does not utilize mirrors, approximately 17 periods (pink) and 141 periods (purple) are required, respectively, for this given set of geometric parameters as the peak increases in amplitude and narrows with an increasing number of periodicities (Figure 3.2). This effect of reducing the filter footprint is demonstrated in Figure 3.3 for a variation in the number of periods for the finite design that incorporates mirrors. Even with only 11 periods or less, the spectral characteristics of the infinite scenario can mostly be replicated. However, at the sacrifice of 19.9%

reflection and an increase in 55.2 nm FWHM, the lateral footprint of this finite 7-period filter has decreased by more than a factor of 20 when compared to the 141 periods required to match the performance of an infinite array, and by more than a factor of 2 when compared to the 17 periods required to obtain a similar amplitude response in a finite design that does not incorporate mirrors.

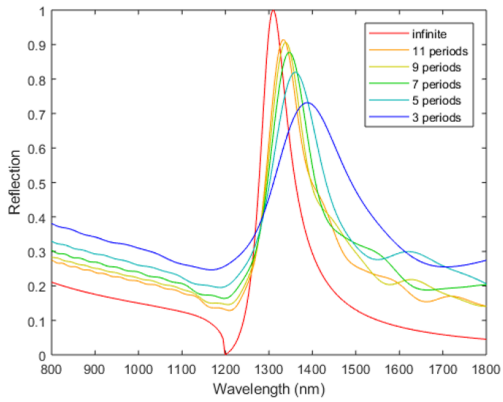

Figure 3.3: FDTD generated spectra demonstrating the effect of reducing the filter footprint by changing the number of periods in the 7 period finite design incorporating mirrors. As the number of periods decreases, the amplitude of the peak decreases and the peak broadens.

The associated electric field profiles for each of the scenarios in Figure 3.1b are presented in Figures 3.1c-3.1e. In Figure 3.1c, a clear enhancement of the electric field is observed for the infinite case, indicative of the GMR phenomenon. If we express the order-mode resonance as $TE_{m,v}$ where m is the generating diffraction order and v is the resultant mode, the order-mode resonance associated with this GMR is $TE_{1,0}$ [73]. The finite case that incorporates mirrors (Figure 3.1d) shows greater field enhancement and less loss relative to that of the finite case with the same number of periods that does not incorporate mirrors (Figure 3.1e), though this enhancement is not as strong as the infinite case. These results clearly demonstrate the advantage of incorporating mirrors in a finite GMR filter design to emulate infinite periodicity.

These ideas are not limited to only 1D gratings, but can also be extended to 2D, with a representative GMR spectrum for a 2D array of cubes presented in Figure 3.4. While the spectral characteristics of this spectrum are not ideal, this spectrum is a proof-of-concept and has not been optimized in any way, meaning that the optical response could be greatly improved. The spectrum presented in Figure 3.4 has geometric parameters $h = 150$ nm, $a = 800$ nm,

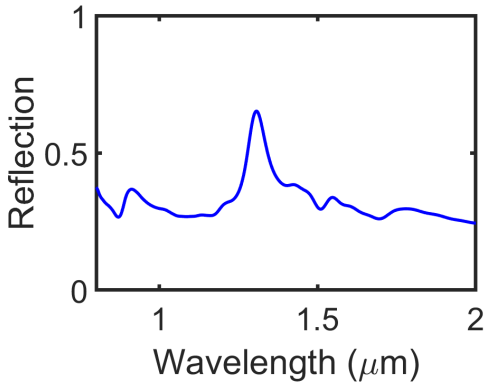

Figure 3.4: FDTD generated spectrum for a 2D array of cubes with $h = 150$ nm, $a = 800$ nm, $f = 0.5$, and $d = 300$ nm with mirrors only along the edges parallel to the electric field.

$f = 0.5$, and $d = 300$ nm with mirrors only along the edges parallel to the electric field. Mirrors are only required along one axis (i.e. two opposite sides of the array instead of all four lateral edges), as the GMR only propogates along a single axis [82], though polarization-independence of the design can be incorporated similar to the nanopillar arrays in Chapter 2 by including mirrors on all four array edges. In this Chapter, we limit the scope of this work to 1D gratings for simplicity and computational resourcefulness, though any ideas presented here are easily extended to 2D without additional design complexity.

As we demonstrated experimentally and computationally previously for an infinite array of a-Si nanopillars embedded in SiO_2, the spectral characteristics of the GMR such as the spectral location, amplitude, and bandwidth or FWHM can be controlled via variation of the geometric parameters of the array [75]. A similar analysis here demonstrates the sensitivity of the GMR in the current filter designs. FDTD simulations were conducted in the near-IR, in which the geometric parameters a, h, f, and s, were varied one at a time while the others were held constant, and the resulting intensity plots are presented in Figure 3.5. The strongest parameter to control the resonance spectral location is the periodicity (Figure 3.5a), with a GMR peak that shifts almost 800 nm when varying a between 500 and 1000 nm. This is important as a suite of filters that each filter a separate wavelength must be created for any spectral imaging system. While reflection amplitude decreases with increasing periodicity, this effect can be counteracted via an increase in the height (Figure 3.5b) or fill fraction (Figure 3.5c) of the a-Si slabs, though overlap with adjacent modes

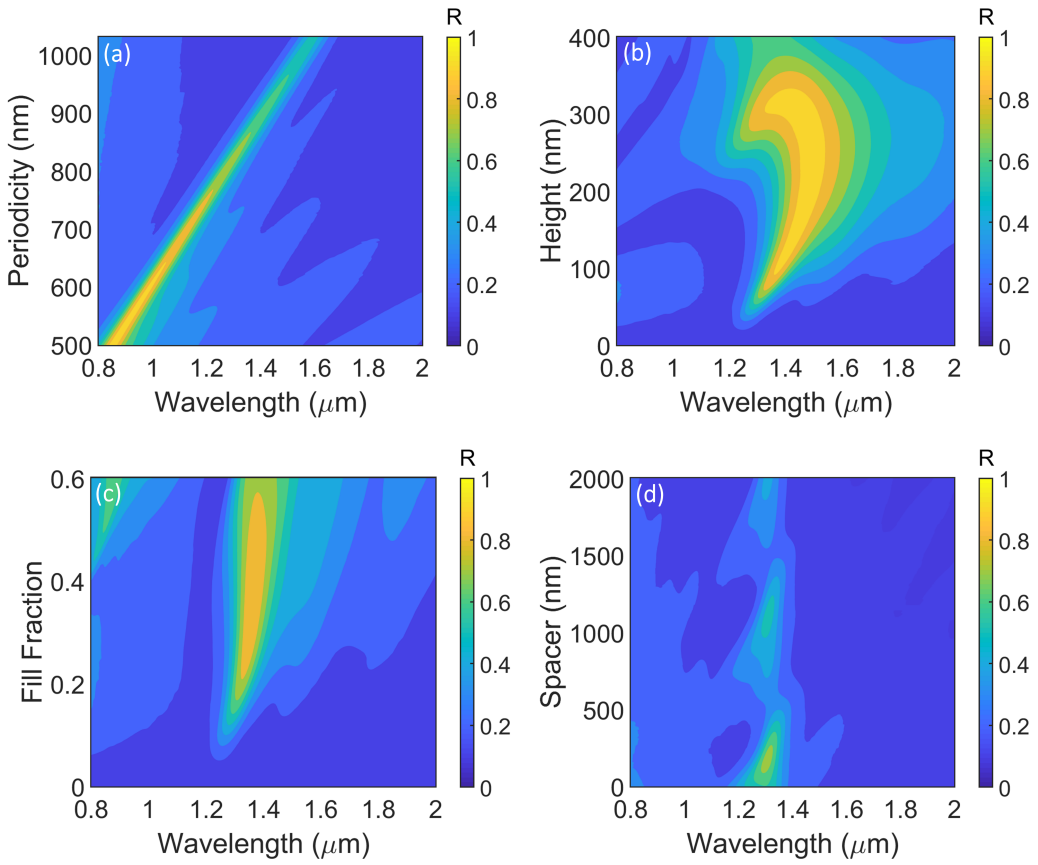

Figure 3.5: FDTD generated intensity plots of simulated reflectivity (color axis) vs wavelength (x-axis) and structure dimensions (y-axis); (a) $h = 64$ nm, $f = 0.18$, $s = 215$ nm, variable a; (b) $a = 831$ nm, $f = 0.18$, $s = 215$ nm, variable h; (c) $a = 831$ nm, $h = 64$ nm, $s = 215$ nm, variable f; (d) $a = 831$ nm, $h = 64$ nm, $f = 0.18$, variable s.

can occur with significant enough parameter variation, such as observed in Figure 3.5b, resulting in a significant broadening and blue-shifted tail at higher values of h, as the resonance of interest begins to interact with a mode at lower wavelengths. Between the two options of variation of the height or variation of the fill fraction, only fill fraction variation is realistic due to parallel fabrication on a single chip. The height of all the filters on a single chip are fixed by the thickness of material deposited and therefore must be the same between each filter. In both variable height and variable fill fraction, we note that there is an optimal range of parameters, outside of which the resonance quickly disappears, though this range can be tuned by simultaneously varying other parameters. Figure 3.5d shows the effect of incorporating the spacer region to ensure the laterally propagating mode within the array does not destructively interfere

with itself. As s controls whether the wave is in or out of phase with itself after reflecting, an optimal range exists for s where the resonance amplitude is the highest, outside of which the amplitude quickly decreases. However, as s is increased by a factor of the period, we observe a return in the resonance, though the amplitude is lower each time due to loss in the system as the laterally propagating mode needs to propagate further to reach the mirrors. Thus, these results demonstrate the ability to passively tune the spectral characteristics of the finite 7-period with mirrors GMR filter through variations of the geometric parameters.

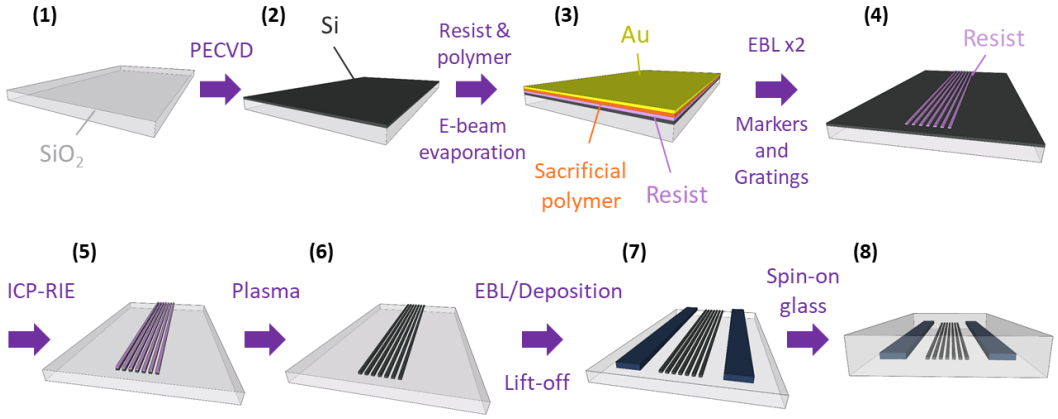

Figure 3.6: Schematic of fabrication process for compact 7-period finite filter design incorporating a-Si slabs between two Al mirrors fully embedded in SiO_2.

3.3 Experimental Fabrication and Verification

The nanopillar arrays were fabricated based on these designs using a top-down methodology on a glass substrate (Figure 3.6). Approximately 64 nm of a-Si was deposited onto the substrate by PECVD at 200 °C, 800 mtorr, and 10 W with 250 sccm of 5% SiH_4 diluted in Ar for 2 minutes and 18 seconds. The thickness deposited in PECVD dictates the height of the a-Si slabs in the array. Prior to all electron beam lithography writes in the fabrication process, a sacrificial layer (a solution of poly(4-styrenesulfonic acid) mixed with 1% by volume of Triton X-100 surfactant) was spin-coated above the resist at 3000 rpm and baked at 90 °C for 3 minutes, followed by 10 nm of electron beam evaporated Au for charge dissipation. The sacrificial layer gold can be removed following EBL in water and developed as normal. Ti alignment markers (h = 200 nm) for all subsequent writes are first patterned in polymethyl methacrylate (PMMA) 950

A8 positive-tone electron beam resist with a Raith 5000+ electron beam writer at 100 kV, developed in methyl isobutyl ketone:isopropanol (MIBK:IPA) in a 1:3 ratio for 90 seconds, and then deposited in electron beam evaporation and lifted off. The next EBL write utilized MaN-2403 negative-tone electron beam resist applied onto the a-Si. The grating slabs were then exposed in an aligned write to the Ti markers and are 21 μm each in length. Following electron beam exposure, the pattern was developed in MF-319 for 40 seconds and the pattern was transferred into the a-Si layer with a pseudo-Bosch SF_6/C_4F_8 etch with ICP-RIE at 15 °C with 40 W ICP power, 1500 W forward power, 26 sccm of SF_6 and 35 sccm of C_4F_8 [76]. The MaN-2403 resist mask was removed by cleaning in an oxygen plasma for 10 minutes (10 mtorr and 80 W with 20 sccm O_2). Finally, the mirrors were aligned and patterned with PMMA 950 A4 and developed in 1:3 MIBK:IPA for 90 seconds, and a 65 nm thick layer of Al that dictated the mirror height was deposited in electron beam evaporation and subsequently lifted-off. Rather than patterning and depositing two rectangular blocks for the mirrors as suggested by Figure 3.1a, we surround the filter with an Al frame. This frame is the length of the filter and spacer regions in one lateral direction perpendicular to the grating beams, and 24 μm in the other lateral direction parallel to the grating beams. Frames of the same lateral dimensions were fabricated without gratings for normalization in measurement. The resulting filter was in-filled with 500 nm of methylsiloxane based spin-on glass solution (Filmtronics 500F).

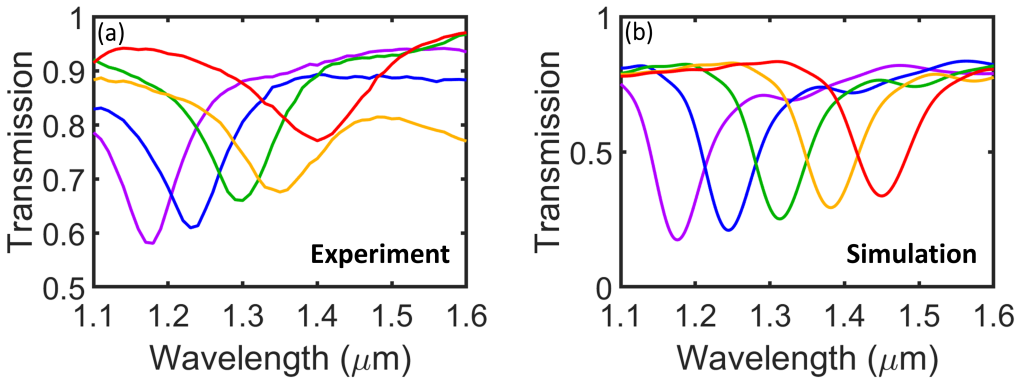

Figure 3.7: Comparison of (a) experimental and (b) simulated transmission measurements for variable periodicity. The arrays have the geometric parameters optimized in NOMAD of $h = 64$ nm, $f = 0.18$, $d = 61$ nm, $s = 215$ nm, and variable $a = 731$ nm (purple), 781 nm (blue), 831 nm (green), 881 nm (yellow), and 931 nm (red).

With this fabrication methodology, we fabricated and measured five a-Si gratings with varying periodicity and measured their transmission to verify the computational results experimentally (Figure 3.7). Figure 3.7a displays the experimentally measured transmission spectra for the fabricated arrays at normal incidence, while Figure 3.7b displays the simulated transmission spectra. Measurements were made with a Fianium white light source coupled to a near-IR monochromator with Ge photodetectors and a 20x Mitutuyo objective with a range from 480-1800 nm. This objective allowed focusing of the spot size down to $\sim$10 μm. Transmission measurements were taken from 1100 to 1600 nm spaced evenly 10 nm apart from one another. To properly normalize to the power transmitted through the patterned sample area, transmission through mirror frames matching the area of the sample but with no patterned area was measured. A similar normalization was done in simulations by normalizing to an air-glass-air stack with no pattern, using a Fresnel correction. To account for any power fluctuations between the measurement of the sample and the frame, a pair of Ge photodetectors simultaneously recorded the intensity of the beam transmitting through the sample, I_{ref}, and the intensity of the incident beam, I_{inc}, using a beamsplitter prior to the objective. The tranmissivity of the sample, T, was then calculated by:

$$T = \left(\frac{I_{\text{ref}}}{I_{\text{inc}}}\right)_{\text{sample}} \left(\frac{I_{\text{inc}}}{I_{\text{ref}}}\right)_{\text{frame}} \tag{3.2}$$

The gratings have the NOMAD optimized geometric parameters given earlier, of $h = 64$ nm, $f = 0.18$, $d = 61$ nm, $s = 215$ nm, and variable $a = 731$ nm (purple), 781 nm (blue), 831 nm (green), 881 nm (yellow), and 931 nm (red). Both experiment and simulation follow a similar qualitative trend, with red-shifting, peak broadening, and an increase in the transmission at the peak as the periodicity increases, with similar bandwidths and spectral location matching between experiment and simulation, though the peaks are much weaker in experiment. The transmission dips are as low as 58.1% in experiment, compared to 17.4% in simulation for the same set of parameters. We attribute this loss of efficiency to be due to fabrication imperfections, errors in experimental normalization, fabrication alignment errors, and measurement alignment errors (in angle and in polarization). We note from Figure 3.5d, a misalignment of the spacer region can quickly quench the expected resonance, even with a misalignment of only 10's of nm's. However, these results qualitatively

demonstrate that GMRs with acceptable SNR for spectral imaging can be experimentally observed with this design.

3.4 Other Design Considerations

Crosstalk

With a filter design that has a lateral footprint of <10 μm, this design now has a pixel size and thus spatial resolution on par with available commercial CMOS arrays. As the filter size decreases, optical crosstalk, or interaction between the adjacent filters can become significant, and is important to characterize, as components in an imaging device must be sufficiently spaced as interactions between filters can distort the spectral characteristics of the GMR in two ways: (1) energy passing through one filter leaks into an adjacent filter and (2) light from one filter interacts with light from an adjacent filter.

FDTD simulations detailing the effects of crosstalk in this design are presented in Figure 3.8. Two standard filters are used for this analysis: filter 1 (blue) has parameters $a = 631$ nm, $h = 64$ nm, $f = 0.18$, $d = 61$ nm, and $s = 215$ nm and filter 2 (red) has parameters $a = 831$ nm, $h = 64$ nm, $f = 0.18$, $d = 61$ nm, and $s = 215$ nm, with only a different periodicity between the two filters. As demonstrated in Figure 3.5a, the periodicity is the strongest parameter to tune the spectral location of the GMR and allows us to obtain peaks at different spectral locations. Reference spectra of both filter 1 and filter 2 are simulated independently (i.e. in a separate simulation that does not experience the effects of a second adjacent filter), shown in black. Figure 3.8a shows the interaction of two adjacent filters as the lateral spacing between them, w, is varied. Here, w, is defined as the width of the mirror, while the spacer lengths s_1 and s_2 of filters 1 and 2, respectively, are maintained constant. These spectra are presented for w from 0 to 50 nm, in increments of 10 nm with a separate power monitor (or a photodetector in an imaging system) located 300 nm below each filter. We define this distance between the bottom surface of the filters and the location of the power monitors or detectors as L. In general, although the peak shape is distorted slightly, especially for $w < 20$ nm, the GMR of each filter tends to maintain its amplitude and FWHM, indicating that crosstalk does not greatly affect this design even at small values of w. Figure 3.8b shows the interaction of two adjacent filters as L is varied from 300 nm to 1800 nm in increments of 300 nm, with $w = 0$ nm. In this scenario, very little change is observed, even as the photodetectors are moved further and further away

from the bottom of the filter, indicating that scattering is an insignificant issue in this design. Therefore, GMR peak distortions that appear as a result of placing two filters adjacent to one another is the result of the interaction of the leaky waveguide mode and its ability to couple into the leaky waveguide mode of the adjacent filter, rather than scattering.

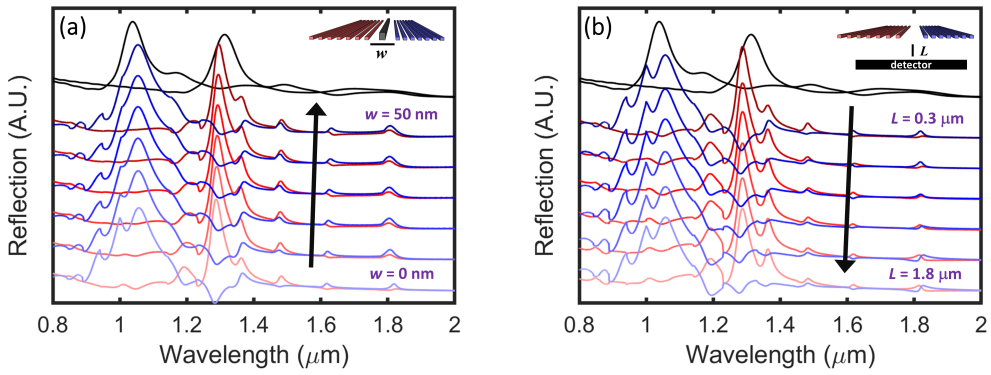

Figure 3.8: FDTD generated spectra demonstrating crosstalk of two adjacent filters as the lateral spacing between them, w, and the axial distance between the filter and the monitor, L, is varied. Filter 1 (blue) has parameters $a = 631$ nm, $h = 64$ nm, $f = 0.18$, $d = 61$ nm, and $s = 215$ nm and filter 2 (red) has parameters $a = 831$ nm, $h = 64$ nm, $f = 0.18$, $d = 61$ nm, and $s = 215$ nm. (a) Overlaid spectra of two filters as w is varied from 0 nm to 50 nm in increments of 10 nm, while $L = 300$ nm. (b) Overlaid spectra of two filters as L is varied from 300 nm to 1800 nm in increments of 300 nm, with $w = 0$ (i.e. no mirror between filters). In both figures, the black spectra indicate the filters at infinity, where each filter is run in a separate simulation independent from the other filter.

Inter-Filter Coupling to Enable Guided Mode Resonances in Small Footprint Filters

The implication of the crosstalk results, notably those in Figure 3.8b as the peaks remain largely unperturbed when the distance between the detector and filter change, is that changes in these reflection peaks are due to inter-filter interactions. Thus, we place filters with different periodicities adjacent to one another and aim to take advantage of the periodicities of neighboring filters such that light propagating through the grating of one filter can couple into an adjacent grating with slightly different periodicity. We do this utilizing two filters of a finite 7-period design without any mirrors. In theory, this could prove to be advantageous, as the addition of the mirrors leads to additional

reflections and thus additional noise and background within this design, which can be reduced with the removal of these mirrors.

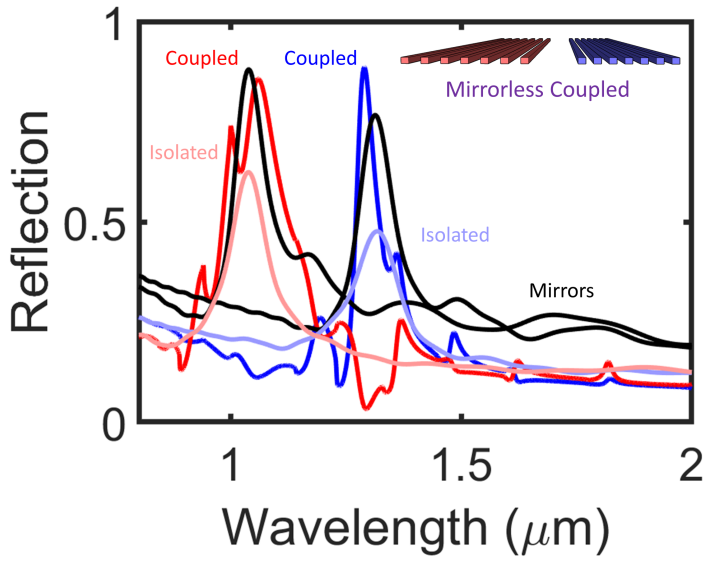

Figure 3.9: FDTD generated spectra comparing the mirrors design, coupled design, and isolated design. The inset is a schematic of the coupled design that does not incorporate mirrors. The coupled design exhibits bandwidth and amplitude comparable to the mirrors design, with noise comparable to the isolated design.

With FDTD simulations, we simulate two adjacent filters with different periodicities, that do not have a mirror between them (Figure 3.9). All spectra considered here are based on designs that only consist of 7 periods. These simulations utilize periodic lateral boundaries, meaning that these two filters are infinitely repeating in alternating fashion, with the unit cell indicated as an inset in Figure 3.9. Thus, each filter is surrounded on both sides with the filter of opposite periodicity. Here, we present the response of three designs together for comparison: (1) the 7-period finite design with mirrors (black) that corresponds with the work previously demonstrated here in Chapter 3 which we will henceforth refer to as the mirrors design, (2) the mirrorless 7-period design with adjacent filters of different periodicity (dark red and dark blue, for each filter) henceforth referred to as the mirrorless coupled (or simply coupled) design that is proposed as an improvement over the mirrors design, and (3) the mirrorless 7-period designs that are mirrorless and isolated without any adjacent filters (pale red and pale blue) henceforth referred to as the mirrorless isolated (or simply isolated) design included as a reference for comparison. As

discussed in this chapter, we know that the mirrors design greatly outperforms the isolated design in terms of increased amplitude and reduced bandwidth, though it is noted that this comes at the cost of slightly greater noise, due to additional reflections introduced by the reflective mirrors. However, we also find that by placing two filters at an optimized distance from one another, the amplitude and bandwidth of the coupled design can not only match or exceed that of the mirrors design, but also demonstrate lower noise levels comparable to that of the isolated design, ultimately leading to increased SNR ratio of an imaging device. An additional benefit of this newly proposed improved design is a further reduction in lateral footprint due to removal of the mirrors.

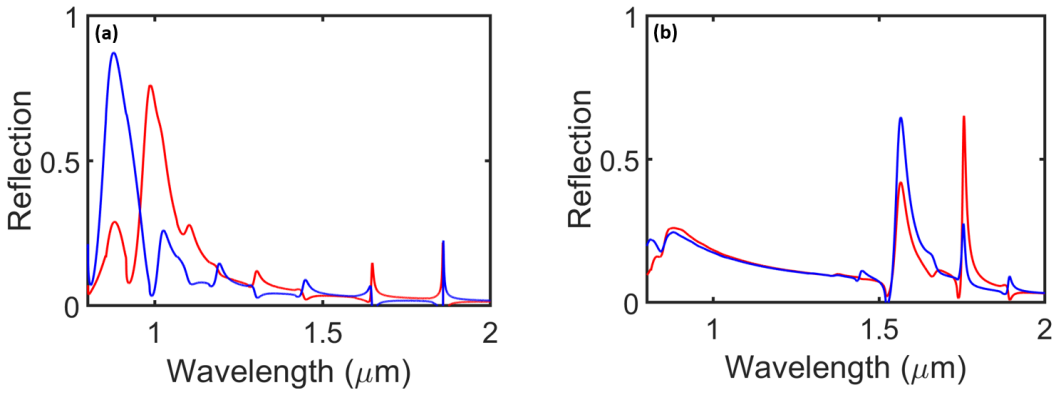

Figure 3.10: FDTD generated spectra demonstrating filtering at each end of the 0.8-2.0 μm spectral range. Only the periodicity, a, and inter-filter distance, b are varied to cover this spectral range. The filters have parameters: (a) $a_1 =$ 531 nm, $a_2 = 601$ nm, and $b = 50$ nm. (b) $a_1 = 1070$ nm, $a_2 = 1105$ nm, and $b = 400$nm.

Next, we utilize this idea, and design a suite of 16 filters that would make up a superpixel in an imaging system filtering the entire region between 0.8-2.0 μm, with each filter filtering a unique wavelength, by only varying the periodicity and inter-filter distance, which we denote, b. The inter-filter distance is the distance in addition to the existing spacer regions (i.e. what previously was the length of a mirror). Although we no longer incorporate mirrors, we still maintain the spacer regions for consistency. We utilize the coupled design, and run similar simulations with two adjacent filters utilizing periodic boundary conditions. In doing so, we can generate filters that filter 16 different wavelengths. The results of three of these filters are presented in Figure 3.10. All of the filters maintain the standard NOMAD optimized values of $h = 64$ nm, $f = 0.18$, and $s = 215$ nm, while we vary only the periodicities and inter-filter distance

while maintaining a constant height, as we would in parallel fabrication for a real device. The variation in periodicity allows the peak to shift, while the variation in inter-filter distance allows for tuning and optimization of the peak performance. The two filters in Figure 3.10a have periodicities $a_1 = 531$ nm (blue) and $a_2 = 601$ nm (red), and inter-filter distance $b = 50$ nm. In doing so, we are able to obtain two contiguous spectral bands. We continue to do this throughout this spectral range, until we reach filters at the higher wavelength end of the spectrum (Figure 3.10)b. Here, we have $a_1 = 1070$ nm (blue), $a_2 = 1105$ nm (red), and $b = 400$ nm. Of important note is that there is only a 35 nm difference in the periodicities between these two filters, versus the 70 nm difference between the two filters in Figure 3.10. From Figure 3.5a, we know that as we increase the periodicity, we narrow the peak and lose amplitude. In doing so, one challenge that arises is that the peaks now narrow sufficiently such that contiguity between the two spectral bands is lost. The immediately apparent solution to re-obtain contiguity is to reduce the differences between the periodicites of the two peaks as the peaks narrow. However, as the periodicities of the peaks approach one another, we begin to observe leakage from one peak into the other, which ultimately contributes to noise in a filtering measurement. Significant optimization on these filters has yet to be completed, as only the periodicity and inter-filter distance was varied here. Simultaneous variation of the height and fill fractions with the periodicity and inter-filter distance could serve to alleviate this problem. Of important note is that optimization must be done iteratively or in large, computationally expensive simulations containing more filters, as only two adjacent filters are accounted for in these simulations while there are significantly more that can exist in a single superpixel in an actual imaging device that may interact with one another. As each filter has its entire set of geometric parameters, the full optimization for such a structure to maximize device performance is challenging, and extremely computationally expensive.

For simplicity, we explore the effect of varying the other parameters on the mirrorless coupled design with only two filters, varying one geometric parameter at a time while keeping the others constant, with the intention of reducing the leakage between adjacent peaks (Figure 3.11). Figure 3.11a has $a_1 = 930$ nm, $a_2 = 990$ nm, $b = 325$ nm, $h = 64$ nm, $s = 215$ nm, and fill fractions $f_1 = f_2 = 0.2$. Qualitatively, these peaks are more or less similar to the peaks found in Figure 3.10, and are an intermediate of the previous examples in

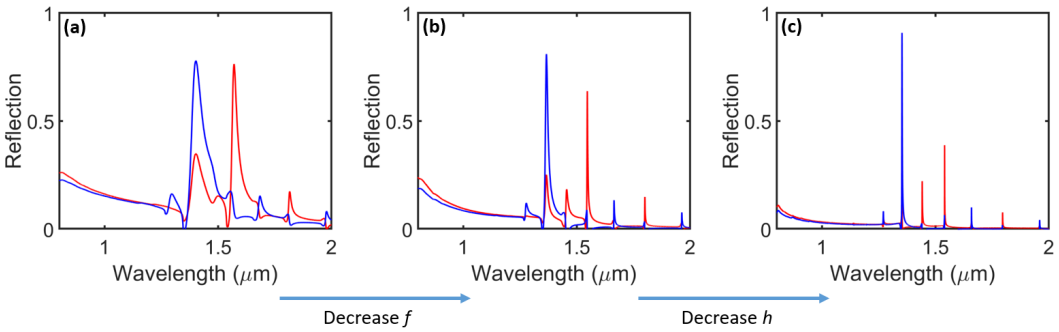

Figure 3.11: Parameter sweeps for the mirrorless coupled design generated in FDTD simulation. In all cases, the filters have parameters $a_1 = 930$ nm, $a_2 = 990$ nm, $b = 325$ nm, and $s = 215$ nm. (a) $f_1 = 0.2$, $f_2 = 0.2$, $h = 64$ nm. (b) Decrease in the fill fractions: $f_1 = 0.1$, $f_2 = 0.1$, $h = 64$ nm. (c) Decrease in the height of both filters: $f_1 = 0.1$, $f_2 = 0.1$, $h = 34$ nm.

Figure 3.10a and Figure 3.10b. In Figure 3.11b, the fill fractions are decreased such that $f_1 = f_2 = 0.1$, and significant narrowing of the peaks is observed, as well as reduced leakage between the two filters. From Figure 3.5c, while a narrowing of the peak is expected, the amplitude should decrease and there is a certain fill fraction below which the peak is completely quenched. However, here we discover that the addition of an adjacent filter causes an increase in the peak amplitude as the peaks narrow. In Figure 3.11b, we continue with these reduced fill fractions, and then reduce the heights of each filter down to $h = 34$ nm. Here, even further narrowing of the peaks are observed with the blue peak reaching FWHM values less than a few nm. Leakage into the blue peak decreases significantly to ≈0.1 (Figure 3.12), though this may only be due to the quenching of the other filter's reflection peak. Diffraction analysis on this spectrum indicates marginal differences between the total and 0^{th} order reflection, indicating this peak is a primarily a result of interaction between the adjacent filters, rather than diffraction or scattering. With a total of 14 periods (less than 15 μm laterally), an extremely high reflection rapid spectral variation near-unity with only several nm FWHM is observed.

3.5 Conclusions

Conventional GMR-based filters possess high resolving power at the cost of requiring many periods and thus large lateral footprints and large pixel sizes in an imaging system since incident light that is scattered into a periodic array must propagate for a sufficient number of periods until it can scatter

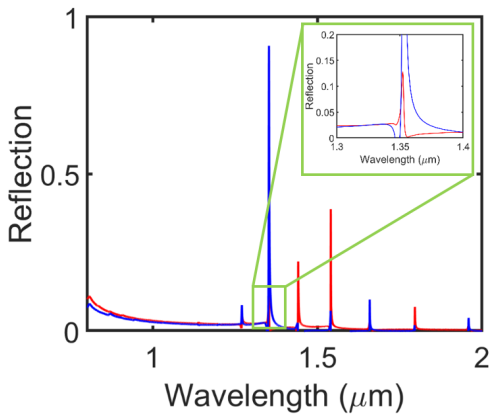

Figure 3.12: Magnified plot of Figure 3.11c showing that the leakage of the other filter (red band) has reduced to ≈0.1 in the blue band as the fill fraction and height are decreased from their standard values in the coupled design.

back out. If this does not occur, edge loss effects are observed, leading to decreased peak amplitudes and increased bandwidths. We demonstrate that these edge loss effects can be suppressed, both in simulation and in experiment, by introducing a design that utilizes a 7-period compact and ultra-thin a-Si grating surrounded on two sides with reflective Al mirrors embedded in a continuous SiO_2 matrix that demonstrates narrow-band, passively tunable, reflectivity peaks suitable for spectral imaging applications in the near-IR. We compared the effectiveness of this design to an infinite design and a similar compact design without the incorporation of mirrors. We explored the effect of varying geometric parameters of the grating slabs to passively tune the GMR and obtain the desired spectral characteristics and demonstrated its performance and passive tunability in experimentally fabricated filters. The successful miniaturization of the GMR filter design enables the incorporation of these filters in imaging applications where spatial resolution would otherwise be limited by the conventionally large footprints of GMR-based designs.

Chapter 4

HIGH Q-FACTOR BANDPASS FILTERS WITH TANDEM GUIDED MODE RESONANCE FILTERS

4.1 Introduction

We have now demonstrated the ability to fabricate 2D GMR based filters, and demonstrated how the spectral characteristics are ideal for multi- and hyperspectral imaging. Furthermore, we have miniaturized the lateral footprint of these filters down to 5-10 μm, enabling spatial resolution on par with commercial imaging pixel sizes. We sacrificed marginal spectral performance (e.g. spectral resolution and peak amplitude) to significantly reduce the lateral footprint and thereby greatly increase the spatial resolution of our filters. However, the drawback in doing so is a loss in Q-factor with broadened peaks. With these Q-factors, the designs presented in Chapter 3 have sufficient spectral resolution to function in the multispectral regime, but lack the resolution to reach the hyperspectral regime.

Here, we propose and theoretically study in FDTD an alternate design based on ZCGs rather than HCGs. For the modes of interest, a ZCG possesses peaks that have extremely narrow bandwidths [8, 45, 73, 95], though it also possesses two undesirable sidebands. While for some applications, these sidebands may be irrelevant, they pose a problem in the proposed filtering applications. We present a design with a finite ZCG possessing extremely high Q-factor stacked in tandem with a wideband ZCG reflector to overcome the limitations of the traditional ZCG design.

4.2 Design of Tandem Guided Mode Resonance Filter

The designed finite ZCG is presented in Figure 4.1. Figure 4.1a shows a schematic illustration of this design, which operates with incident light in the TE polarization state (red text), with the electric field running parallel to the grating beams. The design of this finite filter is similar to the design of the compact HCG filter in Chapter 3 utilizing a finite filter with mirrors on each side for the array to emulate an infite array, though here we implement the zero-contrast architecture and utilize a design with 11 periods. The finite ZCG incorporates a SiO_2 substrate, Al mirrors, and an a-Si grating exposed

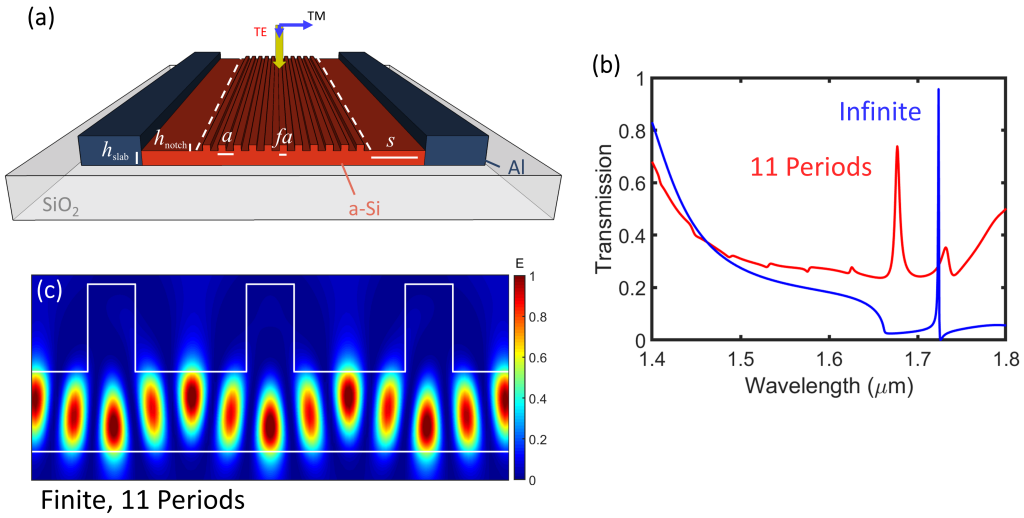

Figure 4.1: Designed finite ZCG structure. (a) Schematic illustration of the 11 period finite ZCG structure on a SiO_2 substrate with an air cover with periodicity, a, fill fraction, f, grating notch height, h_{notch}, slab notch height, h_{slab}, and spacer, s. The illumination and polarization are indicated. This design operates with input light in the TE polarization state with the E-field running parallel to the grating slabs (red text). (b) FDTD simulation comparing the transmission spectrum of an infinite ZCG (blue) to that of an 11 period ZCG (red) with the same geometric parameters. The peak location shifts due to the incorporation of the spacer region.(c) Zoomed in electric field profile of the 11 period ZCG design showing 3 periods. The ZCG is outlined in white. From this E-field profile, the order-mode resonance associated with this narrow passband is determined to be $TE_{2,0}$.

to air (i.e. air cover). We chose 11 periods, though the filter still functions well with fewer periods at the cost of decreasing Q-factor. Unlike the design in Chapter 3, as we utilize the zero-contrast architecture, this design contains an additional slab of high index a-Si material underneath the grating. The geometric parameters are defined the same as in Chapter 3, though we now separate the heights into a: slab height, h_{slab}, notch height, h_{notch}, and mirror height h_{mirror} that correspond with the height of the silicon slab, height of the silicon grating notches, and height of the aluminum mirrors, respectively. This ZCG has geometric parameters $h_{\text{notch}} = 336$ nm, $h_{\text{slab}} = 306$ nm, $h_{\text{mirrors}} = 300$ nm,$a = 1148$ nm, $s = 600$ nm, and $f = 0.3$. NOMAD was not used to optimize this design as was done in Chapter 3, though the response could be improved with such an optimization. The associated transmission profile for this finite ZCG design compared to the infinite case is shown in Figure 4.1b, calculated in FDTD simulation. The spectrum for an infinite ZCG with

the same parameters (without a spacer region or mirrors) is shown in blue, while the spectrum for our proposed finite 11 period design in Figure 4.1a is shown in red with an extremely narrow transmission GMR centered at 1.68 μm and a FWHM of 10 nm. As before, due to the difficulty in accurately defining a background with the Fano line-shape, we calculate the FWHM at half of the peak amplitude, rather than at half of the peak amplitude minus the background, as conventionally defined. This leads us to an underestimation of our design's performance. While the GMR has a high amplitude and small bandwidth (i.e. high Q-factor), there are two undesired sidebands that exist on each side of the resonance. The difference in the spectral location between the finite and infinite case here is a result of the incorporation of a spacer region, which causes the spectral location of this peak to shift. Figure 4.1c shows the electric field profile of this design. It is zoomed in for clarity and only shows 3 periods of the finite ZCG with an outline of the ZCG boundaries shown in white. From this e-field profile, the order-mode resonance associated with this narrow passband is $T_0(TE_{2,0})$ if we express the order-mode resonance as $TE_{m,v}$, where m is the generating diffraction order and v is the resultant mode.

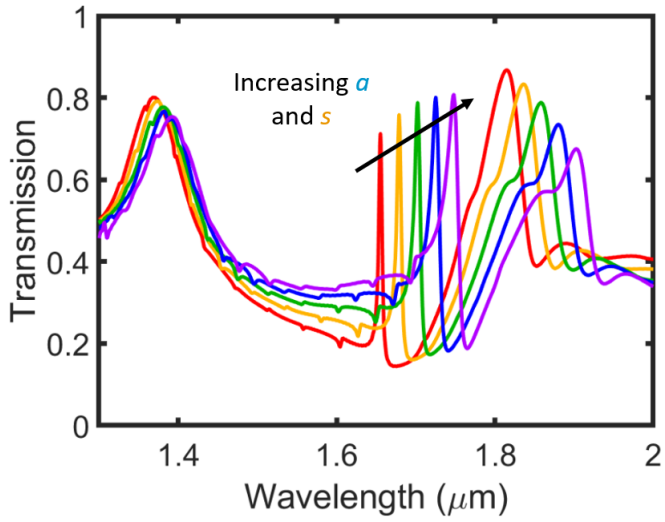

Figure 4.2: FDTD simulation demonstrating the passive tunability of the finite ZCG arrays based on a change in the periodicity and spacer, varied together in increments of 20 nm. The peak of interest can be shifted towards or away from either sideband through this geometric variation.

As before, the spectral characteristics of this GMR can be tuned through geometric parameter variation. Here, we explore only a variation in the spacer and the periodicity, varied simultaneously in simulation. The spacer is defined

as the distance half a period away from the center of the outermost grating slab until the inner mirror edge, and allows us to ensure the reflected wave is in phase with itself. We vary s and a together by a constant amount in increments of 20 nm, and observe red-shifting, an increase in amplitude, an increase in noise, and a decrease of the bandwidth of the GMR as we increase a and s (Figure 4.2). With this increase in geometrical parameters, the right sideband red-shifts and loses amplitude, while the left remains mostly unaffected. This suggests that the left sideband may arise due to axial interference within the array, while the right sideband may arise from a different order-mode resonance.

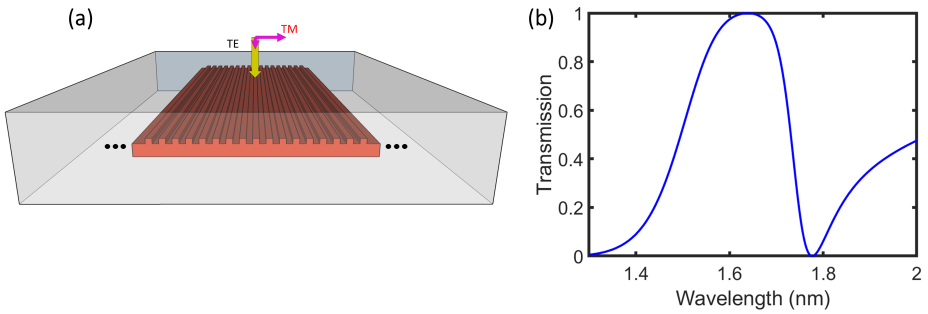

Figure 4.3: Design of infinite ZCG wideband reflector. (a) Schematic illustration of ZCG wideband reflector fully embedded in SiO_2 in the TM polarization state with the E field perpendicular to the direction of the grating slabs (red text). Ellipses on either side of the array indicate that this ZCG is infinite (or sufficiently large to approximate infinity). (b) FDTD simulation providing the transmission spectrum of the wideband reflector. This wideband region cuts off after 1.4 μm, after which a high transmission region exists.

To eliminate the undesired sidebands and isolate the desired GMR passband, we design an infinite wideband ZCG reflection filter proposed to be used in tandem with the finite ZCG filter (Figure 4.3). This filter consists of a SiO_2 substrate and an a-Si grating fully embedded in SiO_2 (i.e. SiO_2 cover) that operates at the opposite polarization state to that of the finite ZCG, in the transverse magnetic (TM) polarization state with the electric field running perpendicular to the length of the grating beams (schematically illustrated in Figure 4.3a). While HCGs are capable of obtaining wideband reflection, ZCGs have been demonstrated to provide even wider reflection bands [7]. Of interest in this context, we noticed the existence of a broad (235 nm FWHM) near-unity transmission band that exists adjacent to the reflection band once the reflection band ends at 1.4 μm (Figure 4.3b). As each finite ZCG transmission band

possesses FWHM as low as 5 μm, a single "infinite" wideband ZCG can be used for many different finite ZCGs, while still being narrow enough to quench the undesired sidebands. Thus, one single "infinite" wideband ZCG can be utilized for each superpixel, where each superpixel contains many finite ZCGs in which each filter contains a separate but contiguous passband required for hyperspectral imaging. Further, for the proposed wavelength range, Ge photodetectors can be utilized which have low photosensitivity for wavelengths beyond 1.8 μm (Figure 4.4) [96]. This can serve to help further quench the right sideband.

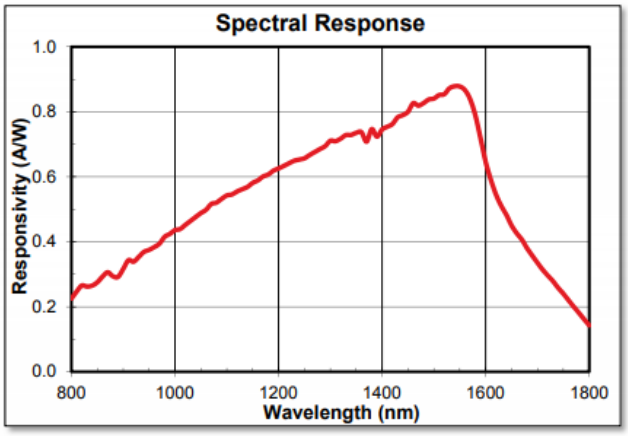

Figure 4.4: Spectral response of a Ge photodetector demonstrating that the photosensitivity of a Ge photodetector quickly diminishes near 1.8 μm. [96]

The full proposed stack is schematically illustrated in Figure 4.5a. The finite ZCG presented in Figure 4.1a with an air cover is stacked on top of the "infinite" ZCG wideband reflector design presented in Figure 4.3a. As the wideband reflector has no bearing on the pixel size of each individual finite ZCG, it is not limited by the same design considerations we have previously encountered, ensuring the wideband reflector has a sufficient number of periods to approximate infinity. The two ZCGs operate at opposite polarizations to obtain the desired optical responses presented here, and thus the wideband reflector is rotated at 90°. As the footprint of the wideband reflector is much greater than that of the finite ZCG, it is possible to utilize one wideband reflector for many ZCGs that each filter a different wavelength. This is illustrated with the FDTD calculated simulation spectra in Figures 4.5b and 4.5c. Figure 4.5b contains the FDTD simulation showing the overlaid transmission spectra of each of the finite ZCGs presented in Figure 2.11 (colored) with the wideband reflector

in Figure 4.3b (black). Then, figure 4.5c shows the resulting transmission spectra of the stacked design after applying a Fresnel correction. The optical response of this tandem stack, including the additional interfaces that are not accounted for in simulation, is calculated by applying a similar Fresnel calculation utilized in Chapters 2 and 3 (Appendix A.1). The form of the Fresnel correction for this stack is:

$$R_{03} = \frac{R_{01} + \left(\frac{R_{12}+R_{23}}{1+R_{23}R_{12}}\right)}{1 + \left(\frac{R_{12}+R_{23}}{1+R_{23}R_{12}}\right)R_{01}} \tag{4.1}$$

where R_{ij} is the reflectivity between layers i and j. This equation is applied for a 4-layer stack of (air-SiO_2-SiO_2-air), where the reflectivity obtained from simulation of the finite ZCG is treated as R_{01} and the reflectivity from the infinite wideband ZCG is treated as R_{12}, the SiO_2-SiO_2 interface. The other air-glass interfaces can be calculated with the normal Fresnel equations assuming a refractive index of $n = 1$ for air, and $n = 1.44$ for SiO_2. Peaks under the wide transmission band can pass through as normal, while peaks outside of this transmission band are quenched. Thus, this design successfully removes the undesired sidebands. A suite of contiguous filters can be designed to fit underneath this wideband and all operate in the same superpixel with a single wideband reflector.

The studies on this dual tandem ZCG filter are purely done in simulation, though fabrication of such a structure should be relatively straightforward, involving a total of 3 electron beam writes (more if alignment marks are written), 2 ICP-RIE depositions, and 1+ electron-beam evaporation step depending on the specific procedure used. The greatest envisioned challenge to such a fabrication process is the alignment of the two filters, though rotational alignment is likely more difficult than lateral alignment of the two filters, since the underlying wideband reflector will be much greater in size than the finite ZCG filters.

4.3 Conclusions

We have now demonstrated the ability to fabricate 2D GMR based filters, and demonstrated how the spectral characteristics are ideal for multi- and hyper-spectral imaging. Furthermore, we have miniaturized the lateral footprint of these filters down to 5-10 μm, enabling spatial resolution on par with commercial

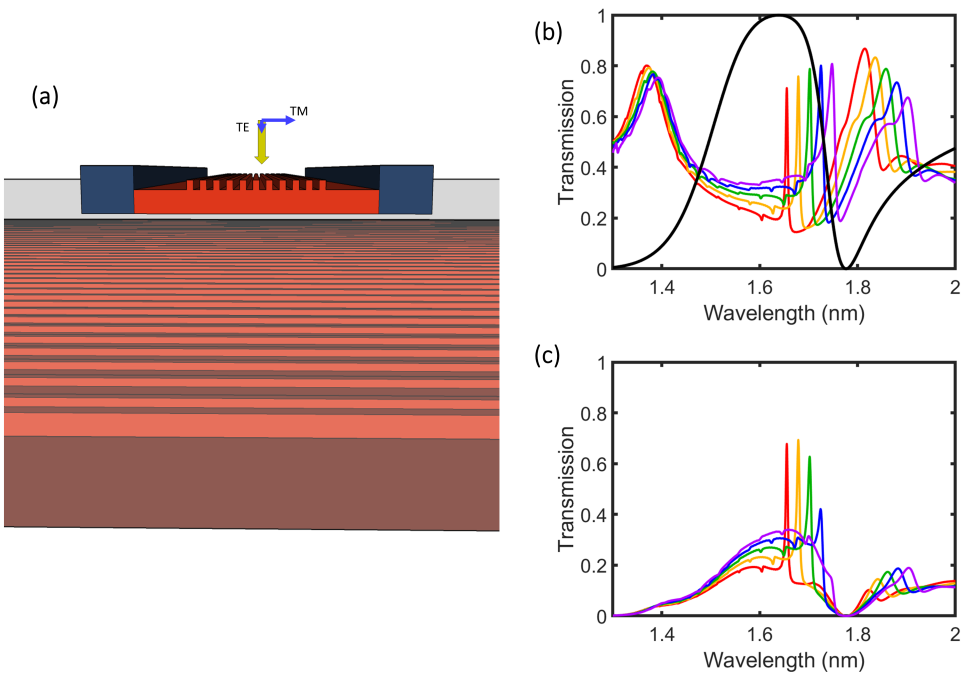

Figure 4.5: Design of the tandem dual ZCG design. (a) Schematic illustrating the stacked tandem ZCG design. These two filters must be operated at opposite polarizations, so the wideband reflector is rotated 90° (b) FDTD simulation showing the overlaid transmission spectra of each of the finite ZCGs (colored) with the wideband reflector (black). (c) Resulting transmission spectra of the stacked design after applying a Fresnel correction. Peaks under the wide transmission band can pass through as normal, while peaks outside of this transmission band are quenched. This design successfully removes the undesired sidebands.

imaging pixel sizes. We sacrificed marginal spectral performance (e.g. spectral resolution and peak amplitude) to significantly reduce the lateral footprint and thereby greatly increase the spatial resolution of our filters. However, the drawback in doing so is the loss in Q-factor with broadened peaks. With this cost, the designs presented in Chapter 3 function in the multispectral regime, but lack the resolution to reach the hyperspectral regime.

We proposed a filter design incorporating a finite ZCG with an extremely high Q-factor passband and two undesirable sidebands stacked in tandem with an infinite wideband reflector ZCG that possesses a broader adjacent passband that can quench the sidebands while permitting transmission of the desired finite ZCG GMRs to enable hyperspectral filtering and imaging, which overcomes the traditional limitations of ZCGs in this context. We demonstrated

the total response of such a stack and how such a design can provide high amplitude transmission passbands with bandwidths less than 10 nm. Such a design utilizes only conventional nanofabrication techniques and thus should be easily fabricated and scaled to production.

Chapter 5

3D DIELECTRIC PHOTONIC CRYSTALS: NANO-ARCHITECTED TIO_2

5.1 Introduction

In this chapter, we transition from planar PhCs to 3D PhCs in the visible and near-IR. For many photonics applications, sub-micron features must be obtained in a low absorption, high refractive index material. One possible pathway to attain this goal is through the AM of hybrid organic-inorganic materials via DLW of a pre-ceramic architecture followed by pyrolysis in air. This technique possesses significant flexibility in the materials and geometries that can be printed, a traditional challenge in the fabrication of 3D PhCs. We approach this challenge with the goal of facilitating and expanding the suite of available materials that can be used to fabricate 3D PhCs to enable future applications of 3D PhCs. Here, we focus specifically on the goal of printing materials with high refractive index with AM. Nanoarchitecting of transparent high refractive index 3D materials often requires complex experimental procedures, such as multi-angled etching [97], micromanipulation to stack individual layers [98], or single or double-inversion of a 3D template that tends to result in features with up to 16% porosity at best [99, 100], and available materials for fabrication via purely additive methods have been much more limited.

Using DLW is relatively simple when compared to some of the aforementioned fabrication techniques, but traditionally was used to only create structures in polymer. Typical polymers possess refractive indices between 1.30-1.70. Several hybrid materials that can be used for lithography, including Si, Zr, Zn, and Ge-based compositions, have been formulated and demonstrated [101–103], but the refractive indices of the final post-process materials have been found to be less than 1.60. Other work has demonstrated the DLW of As_2S_3 chalcogenide glasses with n between 2.45 and 2.53 by taking advantage of their photo-induced metastability [104]. Metal oxides have also been nano-architectured with DLW of aqueous metal-containing photopolymers followed by calcination, but the low metal ion loading leads to linear shrinkage of up to 87%, making it difficult to preserve complex geometries that may be required for 3D PhCs

[105]. Currently, the suite of materials with high refractive index that can be used to fabricate structures with AM is very limited. As our model material, we fabricate structures in TiO_2 due to its relatively high index ($n \approx 2.45$-3.03 from 500-1500 nm) and its band gap or optical absorption edge at 3.0 eV for rutile TiO_2 (or 3.2 eV for anatase TiO_2) which lies in the UV, rendering it an ideal high-index, low-absorbing candidate in the visible regime. The highest refractive index is attained in the rutile phase of TiO_2, and this high index contrast can be fully exploited only for non-porous constituent material. Thus, an ideal AM process for TiO_2 would be able to repeatably and accurately produce sub-micron features out of fully dense rutile TiO_2. Due to these ideal properties, TiO_2 is a material that is often chosen for applications in the visible regime and has already been demonstrated in 3D photonic crystals [100, 106]. As such, it serves as the perfect benchmark to compare and confirm that our AM process is working as intended.

AM processes for TiO_2 have previously appeared in literature through several methods: (1) the direct ink writing (DIW) of sol-gel inks [107], (2) femtosecond laser processing [108], and (3) laser-induced decomposition of sol-gel precursors [109], though each of these methods are less than ideal. The DIW of sol-gel inks followed by calcination produces TiO_2 with resolution and feature sizes on the order of 100's of nm's that are at least 10% porous, composed of a large fraction of the lower refractive index anatase phase, ultimately lowering the effective refractive index of the structure [107]. Femtosecond laser processing has been used to selectively introduce insoluble regions by bond breaking in a liquid TiO_2 precursor, but these samples exhibit poor adhesion and are lost upon heat-treating [108]. Finally, Laser-induced decomposition has been used to pattern TiO_2/carbon composites in 2D, but the process has not been shown to have the potential to reach the optical regime, with minimum feature sizes of 3 μm for crystalline TiO_2 [109]. Thus, the current processes for the AM of TiO_2 suffer from high porosity, low refractive index of the constituent material, and poor repeatability. Here, we demonstrate an AM process that is capable of repeatably and accurately producing 3D nano-architected TiO_2 with >99% dense features.

This process begins with a synthesized hybrid organic-inorganic precursor that is used to form a TiO_2-based resin or photoresist for TPL. After writing 3D structures in TPL, these structures are pyrolyzed at 750-900 °C to yield

shrunken ceramic 3D nano-architectures with approximately 60% smaller features that consist entirely of fully dense nanocrystalline TiO_2. We demonstrate this process for 3D dielectric PhCs by fabricating TiO_2 woodpile face-centered tetragonal (FCT) structures with beam dimensions of 300-600 nm and lateral periods of 0.8-1.5 μm. The structures are designed and optimized with PWE simulations and then experimentally characterized with fourier transform infrared spectroscopy (FTIR) measurements for comparison post-fabrication to show that these structures exhibit full photonic band gaps centered at 1.8-2.9 μm. This AM process for fabricating 3D nano-architected fully dense TiO_2 will enable rapid prototyping and manufacturing of 3D PhCs for applications in micro-optical devices.

5.2 Additive Manufacturing of Complex 3D Nano-Architectured Ceramic Structures in TiO_2

The TiO_2 pre-ceramic photopolymer used in TPL was synthesized via a ligand exchange reaction with titanium (IV) ethoxide and acrylic acid in 1:4 molar ratio to synthesize a titanium (IV) acrylate precursor, conducted in a glovebox to minimize exposure to oxygen and water (Figure 5.1a). This hybrid organic-inorganic precursor is combined with an acrylic monomer, pentaerythritol triacrylate, and can be embedded into a polymer network during free-radical polymerization. A two-photon photoinitiator, 7-diethylamino-3-thenoylcoumarin (DETC), was then dissolved in dichloromethane and added to the solution. The resulting liquid pre-ceramic photoresist was used to fabricate 3D structures on silicon substrates in TPL DLW (Figure 5.1b) that rested on a series of springs and pillars that decoupled the fabricated 3D architectures from the substrate, and thereby minimized any structural distortions from shrinkage during pyrolysis (Figure 5.1c) [110, 111]. Following development, these architectures were pyrolyzed in air at 900 °C, resulting in shrunken replicas of the original structures with 60% smaller dimensions made entirely out of TiO_2 (Figure 5.1d). The post-pyrolysis shrinkage appeared to be isotropic and resulting features were uniform.

We demonstrated the efficiency of this approach by fabricating 3D architectures woodpiles with FCT geometry via DLW that had overall dimensions of 220 x 220 μm, a lateral period, x_L, of 3.7 μm, an axial factor (defined as the ratio of the axial period, x_A, to the lateral period x_L) of 1.1, and rectangular beams with 1.3 x 1.5 μm cross-sections, where a is the lateral beam dimension

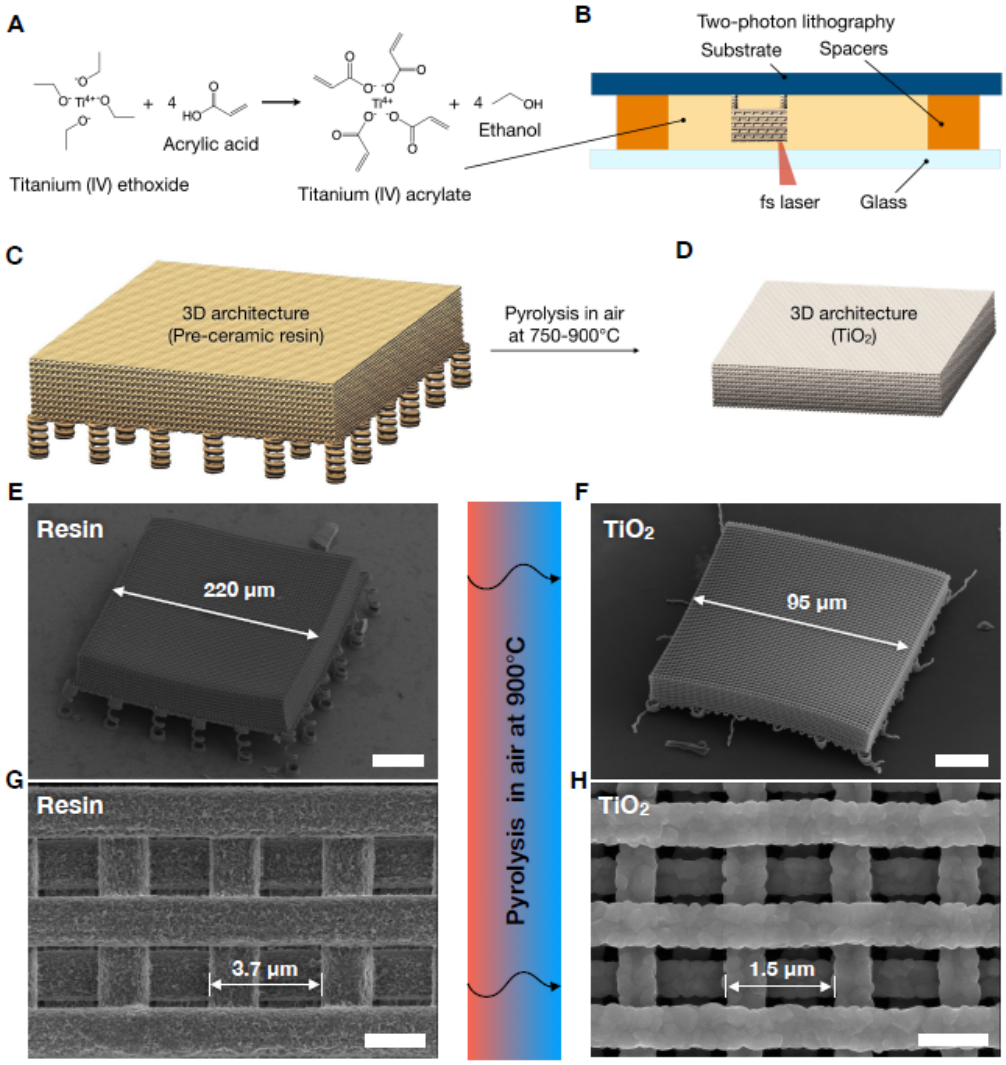

Figure 5.1: Process for AM of nano-architected titanium dioxide (TiO_2). (a) TiO_2 precursor is synthesized using a ligand exchange reaction between titanium (IV) ethoxide and acrylic acid. (b) Schematic of the assembly for sculpting the TiO_2 pre-ceramic photoresist into 3D architectures using TPL. (c) Schematic of the woodpile structure made out of a cross-linked pre-ceramic resin that is being pyrolyzed to form (d) the final nano-architectured structure out of TiO_2. (e) SEM image of the pre-ceramic resin that is pyrolyzed to form the (f) final TiO_2 nano-architecture. (g) Higher magnification SEM image of the pre-ceramic and (h) final TiO_2 structure. Scale bars are 50 μm for (e), 20 μm for (f), 2 μm for (g), and μm for (h).

and b is the axial beam dimension (Figures 5.1e and 5.1g). The woodpile corresponds to different crystal lattices, depending on the axial factor. For an axial factor of 1, the woodpile corresponds to a body-centered cubic (BCC)

lattice, while an axial factor of $\sqrt{2}$ corresponds to a face-centered cubic lattice (FCC). The FCC lattice possesses the most spherical Brillouin zone and thus the widest band gaps [112]. Any other values of axial factors correspond to a FCT lattice. The structure has 60 periods in the lateral direction and 9 periods in the axial direction. Figures 5.1f, 5.1g show SEM images of a representative woodpile structure after pyrolysis that has beams with 530 x 600 nm rectangular cross-sections, a lateral period of 1.47 μm, and lateral dimensions of 95 x 95 μm.

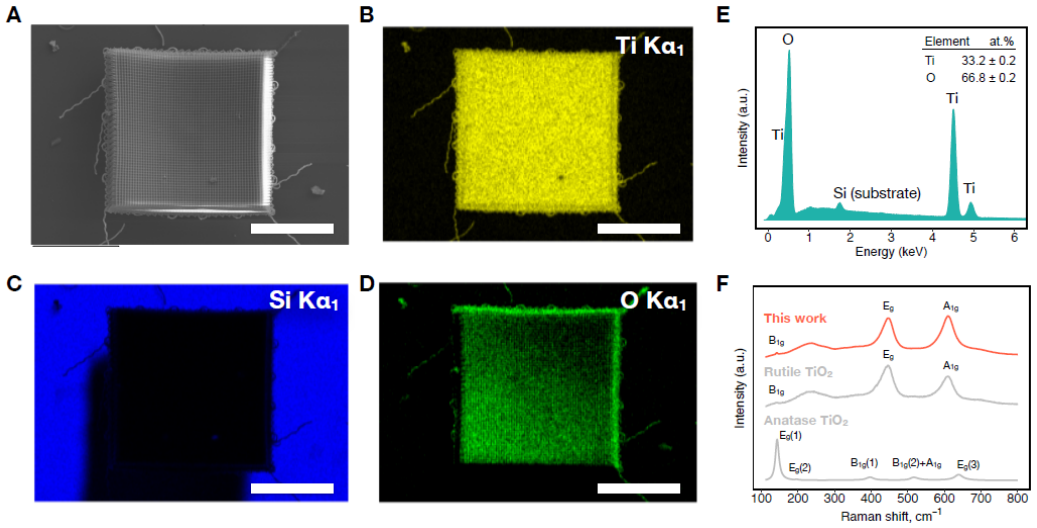

Figure 5.2: EDS and Raman characterization of as-fabricated TiO_2 woodpiles. (a) SEM image of a woodpile structure on a silicon substrate (top view) where EDS maps were taken. (b-d) EDS maps of titanium, silicon, and oxygen showing uniform distribution of Ti and O throughout the woodpile structure. (e) EDS spectrum taken from the woodpile structure reveals mostly titanium and oxygen content. (f) Raman spectrum taken from the woodpile structure compared with a reference spectrum of rutile and anatase TiO_2 suggests a pre-dominant rutile phase of TiO_2. Scale bars are 50 μm for (a-d).

As the goal of this work was to produce structures with high refractive index, a fully dense structure with low porosity ensures that the effective index can be maximized. This information can be gleaned from the chemical composition of the fabricated structures. SEM energy-dispersive X-ray spectroscopy (EDS) was used to characterize the chemical composition of the as-fabricated material on a representative woodpile structure with overall total lateral dimensions of 95 x 95 μm and a lateral period of 1.5 μm (Figure 5.2a). These EDS maps (Figures 5.2b-d) appear uniform throughout the woodpile structure without

regions of segregation into titanium- or oxygen-rich phases. An EDS spectrum taken from a 20 x 20 μm area in the center of the architecture (Figure 5.2e) reveals the chemical composition to be 66.8 at% oxygen and 33.2 at% titanium, corresponding to a 1:2 atomic ratio of Ti to O, characteristic of and indicating TiO_2, as desired. The underlying silicon substrate was excluded from these composition measurements. Compositional and microstructural analysis suggest that this material as-fabricated is comprised of fully dense nano-crystalline rutile TiO_2 that contains minimal to no carbon content. Determining the exact amount of carbon is difficult as EDS is less sensitive to light elements and carbon tends to be present everywhere in the environment. Inclusion of the carbon peak in the EDS spectrum fit did not result in improvement of the fit, which further corroborates extremely low at% C within the fabricated structures. By comparison, previous processes based on laser-driven formation of TiO_2/carbon composites yielded a substantial amount of carbon that can lower the material transparency [109].

Next, to ensure the fabricated structures composed primarily of the higher index rutile phase, the as-fabricated TiO_2 was analyzed via Raman spectroscopy and transmission electron microscopy (TEM). Raman spectra were collected from the 3D TiO_2 architectures using a 514 nm laser focused through a 50x microscope objective. A representative Raman spectrum is shown in Figure 5.2f along with reference spectra collected from both rutile and anatase samples. The Raman spectrum taken from a representative TiO_2 architecture reveal peaks that are in good agreement with first-order vibration modes found in rutile TiO_2 (B_{1g} at 145 cm^{-1}, E_g at 448 cm^{-1}, and A_{1g} at 613 cm^{-1}), as well as with characteristic second-order scattering around 240 cm^{-1} (Figure 5.2f) [113]. The Raman signature revealed peaks at 145 cm^{-1}, 448 cm^{-1}, and 613 cm^{-1} that match the reference spectrum taken from rutile TiO_2 (Figure 5.2f).

The atomic-level microstructure of the as-fabricated TiO_2 structures was determined with TEM and electron diffraction. We prepared a thin cross-section of a woodpile architecture with 960 x 150 nm elliptical cross-sections, lateral periodicities of 1090 nm, and overall lateral dimensions of 70 x 70 m using Focused Ion Beam (FIB) lift out (Figure 5.3a). High-resolution (Figure 5.3b) and dark-field (Figure 5.3c) TEM images reveal that a typical beam cross-section is >99% dense and is comprised of nanocrystalline material with a mean size of 110 nm (Figure 5.3d). An electron diffraction pattern (Figure 5.3b, inset)

confirms rutile TiO_2 as the constituent material, a finding that is consistent with the results of the Raman spectrum analysis. This finding is also consistent with other works that studied phase transformation in sol-gel derived TiO_2 [107, 114]. For example, dry sol-gels of TiO_2 were found to convert from anatase into rutile at 550 °C, with full transformation occurring at 800 °C [114]. Thus, after the high temperature heat treatment at 900 °C during fabrication of these architectures, rutile is expected as the dominant phase of TiO_2. Some of the aforementioned existing demonstrations in literature of a TiO_2 AM process resulted in partially converted TiO_2 (e.g. rutile/anatase mix of 47 wt%/53 wt% [107]) and porous features with 10-16% air content [100, 107], both of which lower the effective index of the final fabricated material and structure, limiting their utility in photonics applications where a high index is required.

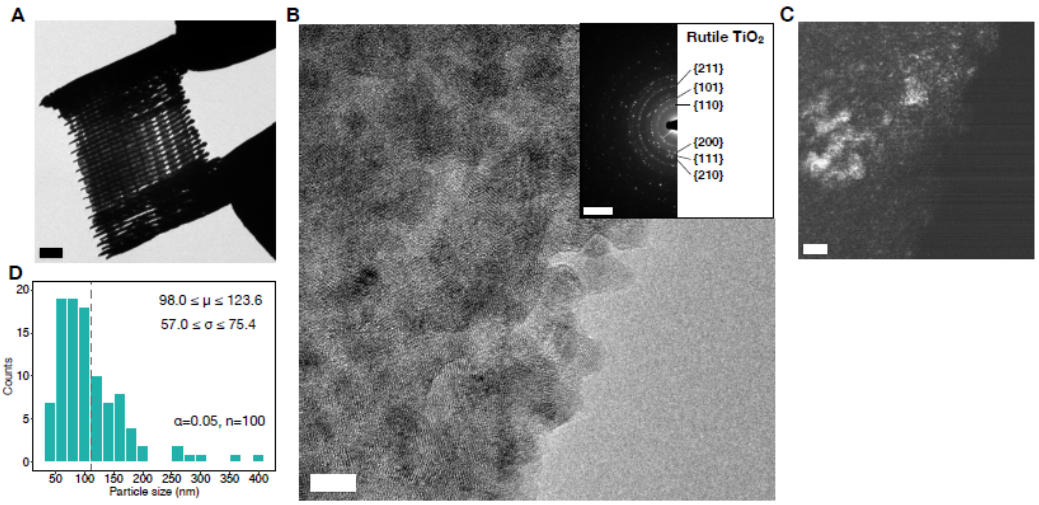

Figure 5.3: TEM for as-fabricated TiO_2 woodpile structures. (a) FIB lift out of woodpile architecture. (b) High-resolution TEM image with electron diffraction pattern inset. (c) Dark-field TEM image. (d) Particle size of TEM sample. Scale bars are: 2 μm for (a), 5 μm for (b), and 5 μm for (c)

5.3 Verification of the 3D Woodpile Photonic Band Gap

The photonic band structure of the 3D woodpile PhCs were calculated using a PWE method with the commercially available software package RSoft BandSOLVE, which rigorously solves Maxwell's equations by forming a linear set of eigenvalue equations and finding functions that minimize the E-field and find successive modes.

In PWE, Beginning from Maxwell's equations, Faraday's law of induction and

Ampere's law (the curl equations) can be combined under the assumption that all materials are linear, lossless, and isotropic to give the time-independent form of the wave equation, the Helmholtz equation [115]:

$$\nabla \times [\frac{1}{\epsilon(\mathbf{r})} \nabla \times \mathbf{H}(\mathbf{r})] = \frac{\omega^2}{c^2} \mathbf{H}(\mathbf{r}) \tag{5.1}$$

In periodic dielectric materials, the solution to this "master equation" (Equation 5.1) must satisfy:

$$\mathbf{H}(\mathbf{r}) = e^{i(\mathbf{k}\cdot\mathbf{r})} u_k(\mathbf{r}) \tag{5.2}$$

By applying Bloch's theorem, an eigenvalue equation can be obtained for an unknown frequency eigenvalue and periodic Bloch mode function, u_k, that represents the periodicity of the lattice with the wavevector as a free variable. The periodic Bloch mode function, u_k, satisfies:

$$u_k(\mathbf{r}) = u_k(\mathbf{r} + \mathbf{a}) \tag{5.3}$$

This function indicates the periodicity of u_k. u_k is expanded as a Fourier series over plane waves in reciprocal space. Substituting this expansion into Equation 5.1 provides a linear set of eigenvalue equations. Because periodicity is imposed from the Bloch mode function, only the first Brillouin zone needs to be considered in the calculation. The H-field eigenmodes can be calculated and converted to the required E-fields via Ampere's law. By finding the function that minimizes the E-field, successive modes (bands) are found.

The simulated structures have FCT crystal structure and individual lattice beams comprised of a single material with constant refractive index of 2.30 (the PWE simulations are assumed to be dispersionless), based on ellipsometry measurements on a film of the TiO_2 resin (Figure 5.4). Based off of these PWE simulations, sets of geometric parameters were generated and used to inform and guide fabrication. To compensate for fabrication imperfections and sensitivity of the geometric parameters to imperfections, the geometric parameters of as-fabricated structures were re-measured in SEM and the band structure simulations were re-run back and forth in an iterative process to ensure that the experimentally as-fabricated structures exhibit a full photonic band gap.

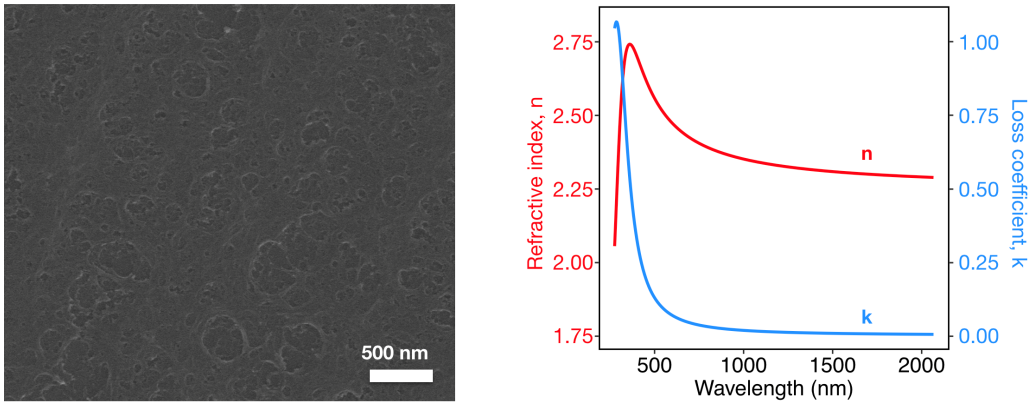

Figure 5.4: SEM image of a 100 nm-thick film of TiO_2 on Si prepared for ellipsometry measurements

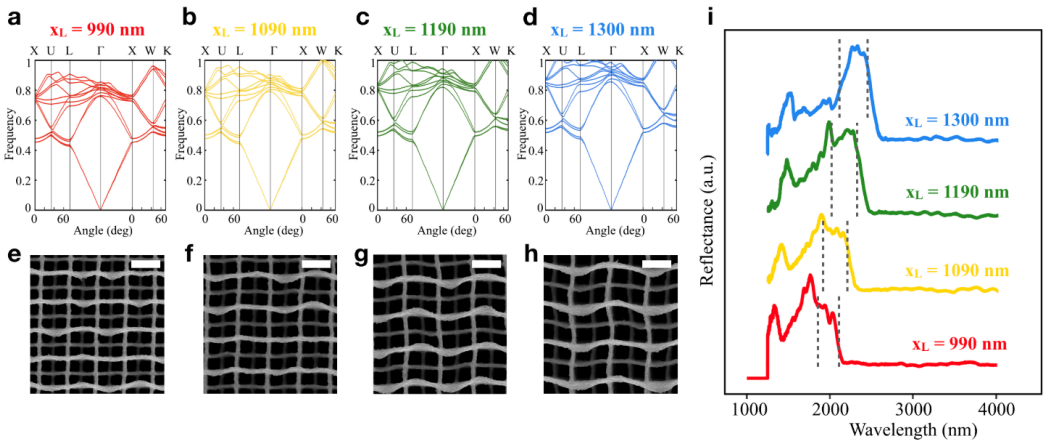

Figure 5.5: Partial gap structures fabricated with AM process. (a-d) Band structures of the woodpile architectures with lateral periods of 990 nm, 1090 nm, 1190 nm, and 1300 nm showing passive tunability of stop band position. (e-h) SEM images of representative woodpile structures (top view) fabricated with the TiO_2 AM process. (i) Measured reflectance spectra for as-fabricated woodpile structures with varying periodicities showing passive tunability of the reflectance band position. Vertical dashed lines correspond to the range of the reflectance band positions from PWE simulations for the range of angles probed in FTIR. Scale bars are for 1 μm for (e-h)

Through this iterative process, prior to significant optimization, initially fabricated woodpile architectures did not exhibit a full photonic band gap, but rather only a partial band gap for certain angles. The results for these structures are summarized in Figure 5.5. The four woodpiles have lateral periodicities of 990 nm, 1090 nm, 1190 nm, and 1300 nm, with axial factors of 1.1, and a number of lateral periods of 70, 64, 59, and 54, and a number of axial periods

of 15, 15, 14, and 12, respectively. The associated band structure for each of these structures calculated in PWE are shown in Figures 5.5a-5.5d. We experimentally confirmed the simulation results by probing the reflectance of as-fabricated woodpile structures (Figure 5.5i). Reflectance and transmittance spectra were collected in FTIR with a calcium fluoride beam splitter and an IR light source. The angle range for the Cassegrain objective used in the microscope was between 16° and 35.5° relative to the normal. A background signal was collected from double-sided polished silicon that served as a substrate for the samples. A SEM image for each is shown in Figures 5.5e-5.5h. The band edges for these structures are summarized in Table 5.1.

Table 5.1: Partial photonic band gap edges (nm) for woodpile structures with lateral periods between 990 nm and 1300 nm for specific angles in XUL and XWK directions in Figure 5.5

Direction	Angle	Band edges in wavelength, nm			
		x_L = 990	x_L = 1090	x_L = 1190	x_L = 1300
X-U-L		2025.8	2126.0	2231.8	2337.3
	16	2121.3	2221.3	2330.1	2435.8
		1912.3	1998.5	2095.1	2186.3
	35.5	1977.6	2085.7	2206.6	2320.2
X-W-K		2016.7	2116.9	2224.7	2330.2
	16	2120.4	2220.4	2333.8	2439.5
		1848.0	1936.4	2031.1	2127.0
	35.5	1939.3	2040.1	2159.3	2268.4

To obtain full band gap structures, after several iterations to ensure a full band gap in simulation, we chose geometric parameters that correspond to the woodpile architecture shown in 5.1f and 5.1h. As Maxwell's equations are not scale dependent and the PhC band gap effect is dependent on the periodicity, any PWE solution and full photonic band gap that exists can be scaled to the desired target wavelength. A band structure showing the original full photonic band gap from PWE was found between 0.465 ($2\pi c/x_L$) and 0.474 ($2\pi c/x_L$) (Figure 5.6), which corresponds to gap edges at the wavelengths 3.10 μm and 3.16 μm. Figure 5.7a shows a band diagram calculated for this FCT woodpile architecture, and the corresponding Brillouin zone (Figure 5.7a, inset). FTIR measurements were taken between 16° and 35.5° within a 30 x 30 μm area at the center of the sample. These measurements revealed a high reflectance and low transmittance band centered at around 2.9 μm in these woodpile structures (Figure 5.7b). To compare these spectra to simulations, we plotted the expected position of a full photonic band gap as a grey band and the range

of the angle-dependent stop band positions for angles between 16° and 35.5° as vertical dash lines (Figure 5.7b). The position values of these bands were found to be within 7% from the expected full photonic band gap.

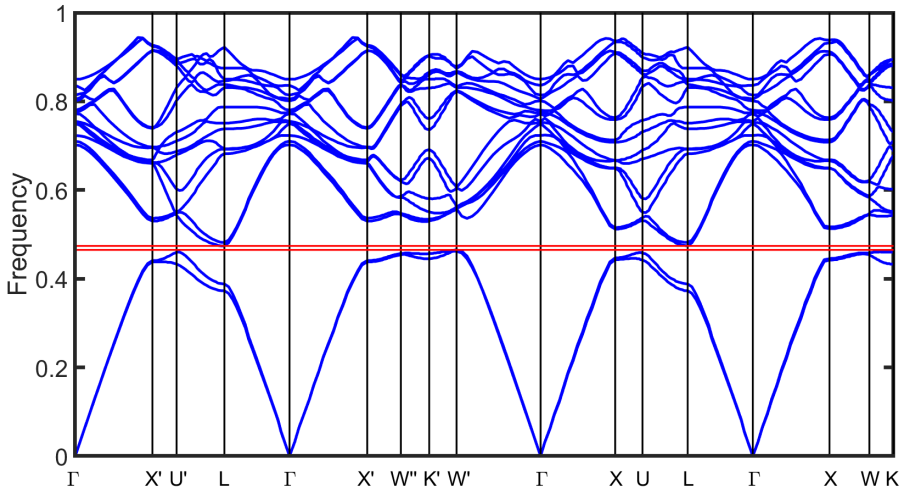

Figure 5.6: PWE generated band structure showing the existence of a full photonic band gap in the simulated FCT woodpile architecture

As similarly demonstrated in other experimental studies [99], due to the optics within FTIR, the position of reflectance and transmittance bands observed by FTIR is influenced by a range of stop-band positions that are being probed simultaneously at off-normal light incidences (i.e. measurements are not angle-resolved). We calculated the expected angle-dependent stop-band edges from the band diagram for the woodpile structure probed along the X-U-L and X-W-K directions simultaneously at many off-normal incidence angles that are representative of the experimental limitations. All of these band edges as well as the edges of the full photonic band gap are summarized in Table 5.2. This approach revealed that the full range of probed stop-bands in this fabricated structure to be between 0.457 ($2\pi c/x_{\mathrm{L}}$) and 0.544 ($2\pi c/x_{\mathrm{L}}$), which corresponds to a wavelength range between 2.7 μm and 3.5 μm.

We further demonstrate the efficiency and ease of this process for rapid prototyping of 3D dielectric photonic crystals due to the simplicity of the band gap scaling via its geometric parameters, and fabricated three additional woodpile structures with lateral periods of 1.12, 1.03, and 0.84. These structures were replicas of the TiO_2 woodpile architecture with $x_{\mathrm{L}} = 1.47$ μm shown in Figure 5.1f, but with all linear dimensions smaller by 25%, 31%, and 44%, respectively

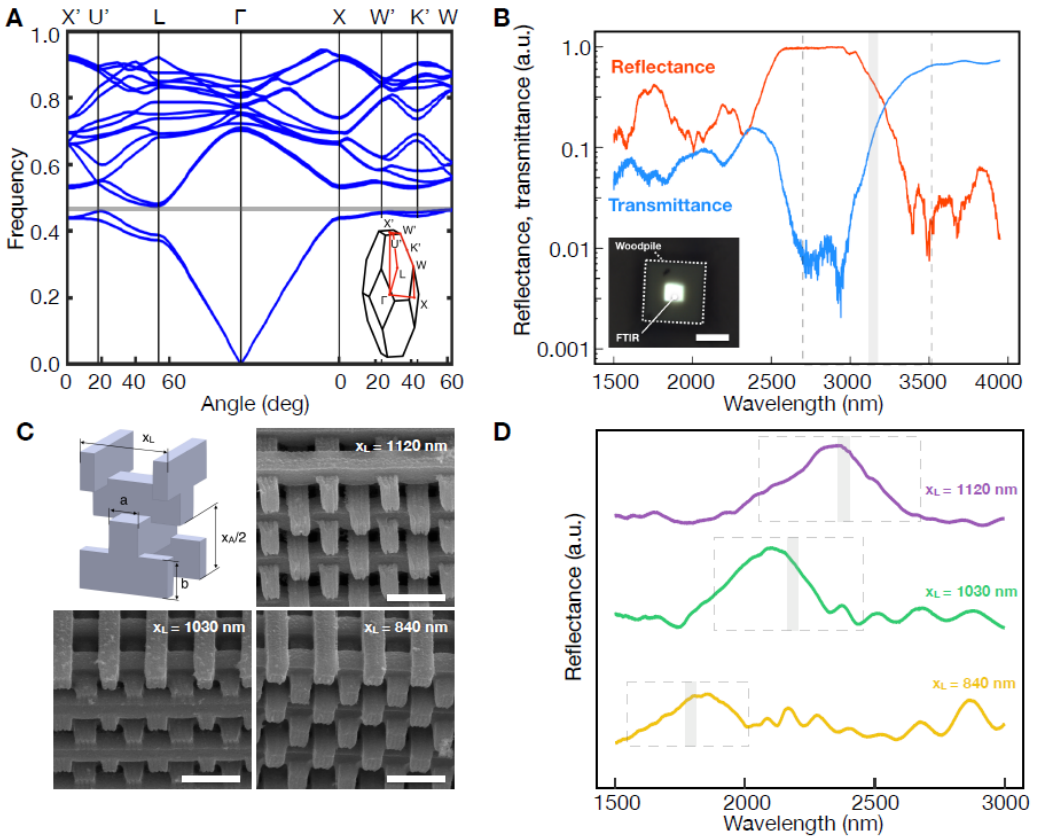

Figure 5.7: Verification of photonic band gap for full band gap woodpile architecture. (a) Band structure full gap structure. (b) FTIR data showing reflectance and transmission bands. The solid grey bar indicates the predicted full band gap position from the band structure, and the dashed grey lines indicate the estimated angle-dependent stop band edges. (c) SEM images of examined woodpiles. (d) FTIR spectra for structures with periodicities of 840 nm, 1030 nm, and 1120 nm.

(Figure 5.7c). Figure 5.7d shows the measured reflectance spectra for these structures collected using FTIR between 1.5 μm and 3.0 μm. For each of these structures, FTIR spectra revealed high reflectance bands centered at 1.8 μm, 2.2 μm, and 2.4 μm, which are within 0.3%, 4.8%, and 3.0% of the target full photonic band gap positions, respectively (Table 5.2).

FTIR reflectance and transmittance spectra taken from four woodpile samples (Figures 5.7b and 5.7d) revealed that the observed high reflectance peaks were centered within 0.3% to 7% from the expected position of full photonic band gaps predicted by PWE (Figure 5.7a). These minor deviations can be attributed to: (1) fabrication imperfections and variability of geometric dimensions throughout the structure and (2) the uncertainty of the refractive index

Table 5.2: Full and angle-dependent photonic band gap edges (nm) for woodpile structures with lateral periods between 840 nm and 1470 nm corresponding to the structures presented in Figure 5.7.

Direction	Angle	Band Edge Frequency (Upper/Lower)	Band edges in wavelength, nm			
			x_L = 1470	x_L = 1120	x_L = 1030	x_L = 840
X'-U'-L	16	0.544	2700	2054	1883	1545
		0.457	3215	2445	2242	1839
	35.5	0.492	2986	2271	2082	1708
		0.418	3521	2678	2455	2014
X'-W'-K'	16	0.543	2708	2060	1888	1549
		0.451	3260	2479	2273	1865
	35.5	0.530	2771	2108	1933	1586
		0.457	3217	2446	2243	1840
Full bandgap		0.474	3101	2359	2162	1774
		0.465	3161	2404	2204	1809

measured by ellipsometry. Many of these imperfections and non-idealities are not able to be accounted for within the PWE simulations. SEM measurements and nested variance analysis showed ~1% in-plane and ~5% out-of-plane deviations of the lateral period throughout the woodpile structure. Second, the measured refractive index of a TiO_2 film of 2.3 is 4-15% lower than a typically expected index value of 2.40-2.71 of rutile TiO_2 within a 1500-3000 nm range. This likely arises as the ellipsometry measurement was done on a TiO_2 film which may be more porous and therefore have a lower index than a fully dense structure as was analyzed in TEM (Figure 5.4, left). Statistically, uncertainty in the geometrical dimensions of up to 5% and in the refractive index of up to 15% can contribute to the up to 7% observed deviations between experimental and simulated peak positions.

5.4 Conclusions

We have developed an additive manufacturing process for titanium dioxide (TiO_2) that allows us to 3D nano-architect nanocrystalline rutile, carbon-free, and fully dense TiO_2 with sub-micron resolution. We have demonstrated this process by fabricating TiO_2 FCT woodpile architectures with features as small as 150 nm. We have taken advantage of the high refractive index and low absorption of as-fabricated material to fabricate a series of PhCs with full photonic band gaps centered at 1.8-2.9 μm, as confirmed by PWE simulations and FTIR measurements. AM of 3D nano-architected titania is poised to

enable facile fabrication of 3D dielectric PhCs, as well as components for a much broader set of applications, including micro-optics and 3D MEMS devices. In a broader sense, a significant aspect and advantage of this work is that this AM process is not limited to only producing TiO_2, but many other materials, and enables the ability to use AM for the fabrication of new materials in 3D (such as high index materials as demonstrated here) that will facilitate and enable further developments in 3D PhCs.

Chapter 6

NEGATIVE REFRACTION IN 3D PHOTONIC CRYSTALS VIA BAND ENGINEERING

6.1 Introduction

As a specific case study, we explore 3D PhCs that exhibit AANR in the mid-IR based on dispersion engineering, which can be enabled by the work in Chapter 5 due to the ability to quickly and easily print 3D architectures in various materials. Negative refraction is the property of light bending back across the same side of the surface normal as it refracts through an interface, first proposed by Veselago in the late 1960s [116]. Snell's law indicates that such a phenemonon implies a negative index of refraction:

$$n_1 \sin\theta_1 = n_2 \sin\theta_2 \tag{6.1}$$

where n_1 and n_2 are the refractive indices of materials 1 and 2 on each side of an interface, and θ_1 and θ_2 are the angles of incidence in which light propagates in each material from the surface normal. Such a property could enable superlensing, allowing subwavelength imaging below the diffraction limit of light. Veselago first proposed that this phenomenon occurs in "left-handed materials", in which both the electric permittivity and magnetic permeability are negative, implying a negative group velocity, $v_g = \frac{\partial\omega}{\partial k}$. This has been found to occur in artificially prepared metamaterials [117–120] and in PhCs consiting only of right-handed materials [121].

Negative refraction in dielectric PhCs is a property which arises from the dispersion characteristics of wave propagation within a PhC [121]. Much of the existing work on negative refraction in PhCs has primarily focused on 2D PhCs [123, 124]. However, complete subwavelength imaging of 3D objects requires a 3D PhC that can negatively refract light in each spatial plane, otherwise known as AANR. Such a 3D PhC was first proposed in 2002 by Luo et al. as a BCC lattice of air cubes embedded in a dielectric with a dielectric constant of 18 (e.g. germanium in the near-IR) [122]. This structure is schematically illustrated along with its bandstructure in Figure 6.1. The proposed air cubes have sides with length $0.75a$ parallel to the sides of the conventional BCC unit

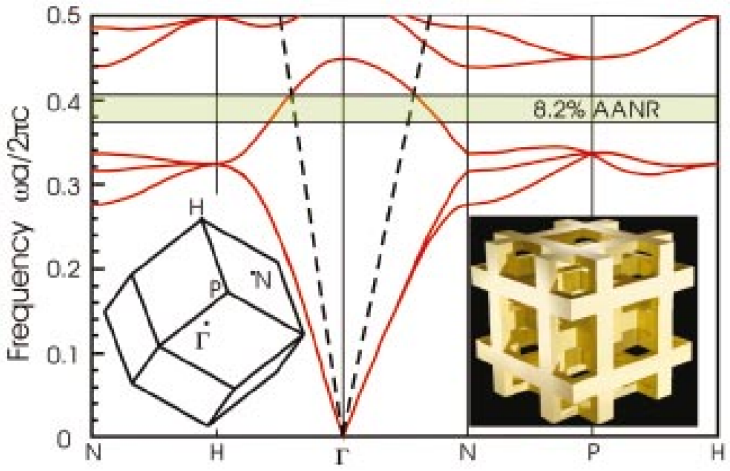

Figure 6.1: (Color) Band structure (red) of a BCC lattice of air cubes in dielectric $\epsilon = 18$. The cubes have sides $0.75a$ and are oriented with sides parallel to those of the conventional BCC cell. In the shaded AANR frequency range (green), the photonic crystal exhibits negative refraction for incoming radiation of all angles. The dashed lines are light lines along Γ-H and Γ-N. Reprinted from [122] with the permission of AIP Publishing.

cell, where a is the periodicity of each unit cell. For AANR to be realized, the frequency range must be near a negative-photonic mass region, where the photonic-crystal constant-frequency contour is all-convex and larger than that of air. In this case, this is the third band, which is concave down in the $\Gamma - \mathrm{H}$ and $\Gamma - \mathrm{N}$ directions between the frequency at which the band intersects the light line or dispersion of air (upper boundary) and the frequency at which the band has an inflection point. For such a structure, a large AANR frequency range of 8.2% exists from $0.375(2\pi c/a)$ to $0.407\ (2\pi c/a)$ in the third band (frequency is normalized as there is no inherent length scale). At $\omega = 0.407\ (2\pi c/a)$, $n_{\text{eff}} \approx -1$ with a nearly spherical frequency contour. The rest of this AANR frequency range should have an index $n_{\text{eff}} \leq -1$, while the region above $0.407\ (2\pi c/a)$ and below the fourth band should have an index $-1 < n_{\text{eff}} < 0$ [122].

Despite this previous theoretical demonstration, the only existing experimental demonstration of AANR in a 3D PhC is by Lu et al. in the microwave regime [125, 126]. PhCs tend to operate at a wavelength on the order of the length scale of light with which it interacts, limiting experimental demonstrations of such a design at the optical and IR length scales due to limitations in available fabrication methods to obtain sufficient feature resolution. As discussed in

Chapter 5, TPL has enabled the fabrication of arbitrarily complex 3D PhCs with sub-micron features, though this is done in polymers that possess relatively low refractive indices. Here, with the use of TPL, we create polymeric core lattices, and utilize deposition techniques to coat the polymer scaffold with a high index dielectric (e.g. germanium) to fabricate 3D core-shell lattices that are capable of negative refraction.

6.2 Design of All-Angle Negative Refraction Photonic Crystals

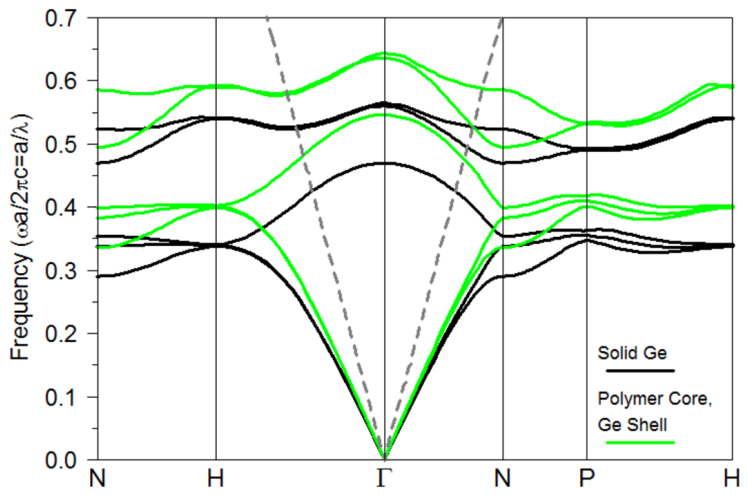

Figure 6.2: Band structure (black) of a 3D BCC photonic crystal lattice composed of fully dielectric beams with $n = 4$ (Ge at $= 8$ μm), and (green) 3D BCC PhC lattice composed of a 500 nm polymer core ($n = 1.49$) and 250 nm germanium shell ($n = 4$). The dashed grey lines are the light lines along Γ-H and Γ-N.

Photonic band-structure of 3D PhCs capable of AANR in the mid-IR (7.6 μm - 8.6 μm) wavelength range were calculated with PWE for a BCC lattice analogous to the one proposed by Luo et al. [122]. These simulations were performed using the commercial software package RSoft BandSOLVE. Beams fabricated in TPL DLW are more cylindrical than rectangular, and so this consideration was implemented into our design. The resulting band structure is presented in Figure 6.2 for two designs: (1) PhC of a single uniform material with a dielectric constant of 16.038 (e.g. germanium at $\lambda = 8.0$ μm) with $a = 4$ μm and beam diameter, $b = 0.25a$ (black curve) and (2) a polymer core-Ge shell PhC with $a = 4$ μm, total diameter $b = 0.25a$ where the index of the acrylate polymer core material is $n = 1.49$ (green curve). If the fraction of Ge shell material decreases such that the effective index of the core-shell beam

decreases below a certain threshold, negative refraction no longer becomes possible. Optimizations in simulation revelealed that within this wavelength range, the diameter of the polymer core cannot be greater than ~600 nm to maintain a sufficient effective index to observe negative refraction, though this beam diameter lies below the resolution limit of TPL DLW.

6.3 Fabrication of Core-Shell All-Angle Negative Refraction Photonic Crystals

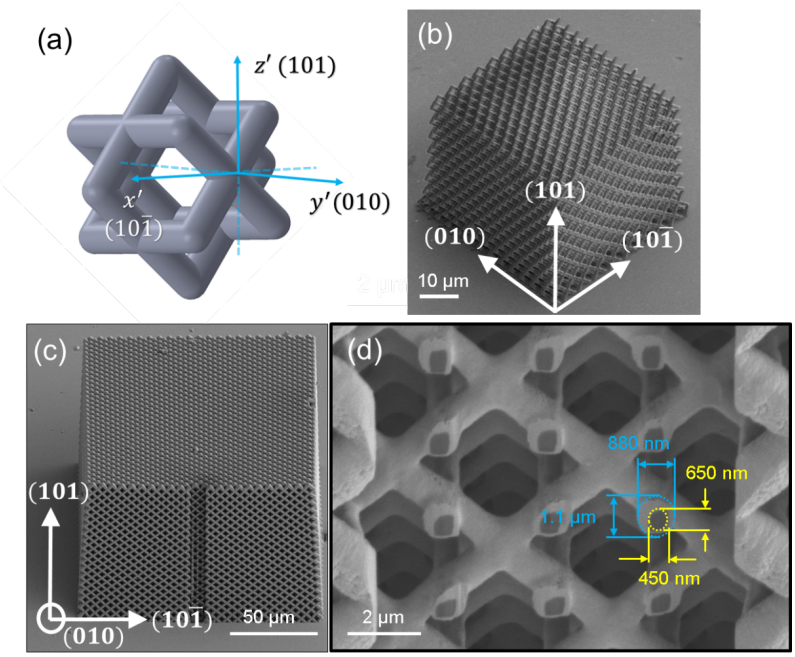

Figure 6.3: 3D BCC photonic crystal lattice. (a) Schematic of proposed rotated BCC cube-like PhC unit cell with (101) surface orientation. (b) A TPL DLW fabricated polymer PhC lattice with (101) surface orientation. (c) SEM image of the full core-shell lattice at 52 tilt with focused ion beam (FIB) milled cross-section. (d) Enlarged section of the PhC (010) face with approximate beam dimensions following a FIB cut into the lattice edge.

The polymer scaffold lattices were fabricated with TPL DLW in acrylate-based "IP-Dip" photosensitive polymer on a 500 μm thick double sided polished silicon chip, to allow for transmission measurements through the sample and substrate. They are rotated 45° from the original cubic design so that the crystal surface is along the (101) direction. After exposing the photoresist and generating the 3D polymer scaffold, structures were developed for 30 minutes in propylene glycol mono-methyl ether acetate (PGMEA) followed by a 5-minute rinse in isopropyl alcohol. To prevent lattice collapse or excessive shrinkage due to capillary

forces during the drying stage, lattices were dried via a critical point drying method using a critical point dryer. The final lattices have lateral dimensions of 130 μm x 130 μm x 100μm (33 x 23 x 18 unit cells). Figure 2 shows a schematic and SEM images of the fabricated structures. For this BCC PhC design, the phenomenon of effective negative index is present in a frequency range where the third band resides. The (101) direction (which corresponds to the PhC orientation and surface symmetry depicted in Figure 6.3b and 6.3c), refers to moving along the Γ-N high symmetry direction and belongs to the C2v symmetry group. For this high symmetry direction, the two potential polarizations of incident light interacting with the PhC are not degenerate, and the $(10\overline{1})$ polarization specifically can couple strongly to the photonic crystal mode [122]. Conversely, for the other polarization along (010), coupling will be nonexistent at normal incidence, and extremely low at non-zero incident angles [122]. Through group symmetry arguments, the negative refraction phenomena will be strongly dependent on PhC orientation and incident light polarization. Negative index behavior in our BCC PhC will be most obvious for a lattice with (101) surface termination and incident light of $(10\overline{1})$ polarization. We therefore chose to fabricate our BCC PhC with the (101) orientation (Figure 6.3b) and note these restrictions on coupling in our experimental designs.

The lattices fabricated in TPL possess circular beams with dimensions of ∼850-900nm. To reduce the beam diameter below <600 nm and thereby maintain a sufficiently high effective index for observation of negative refraction, lattices were etched in an O_2 plasma at 15 sccm O_2 with 50 W power in a downstream remote plasma cleaning mode where oxygen plasma is generated outside the sample chamber which limits sample immersion in energetic plasma and reduces the extent to which lattices are sputtered by energetic ions. With this process, only gentle, isotropic chemical etching should take place on the lattice beam surface by neutral radicals.

This process on average etched the beams at 10 nm/min, though etching was anisotropic even at these mild etch conditions, resulting in elliptical beams and some regions of over-etching causing tapering of the beams. On average, O_2 plasma etching using the parameters listed above yields elliptical beams with a short axis of 454 ± 27 nm, and long axis of 647 ± 49 nm.

The final step for the fabrication of the low-index core, high-index shell BCC PhC lattices is the deposition of germanium onto the etched polymer scaffold, a

step that involved significant fabrication complexity. While a chemical deposition technique such as chemical vapor deposition would provide more isotropic and conformal coatings, due to limited available resources and equipment for Ge deposition, sputtering was the only available approach. We deposited Ge onto etched polymer lattices by sputtering with a Ge target with RF power supply at 100 W and 5 mTorr with 20 sccm argon in a magnetron sputter deposition system. Base pressure was set to $\sim$4x10^{-6} Torr, and target ramp up and ramp down times were precisely controlled at 10 W/min. Prior to deposition on the sample, the target underwent a 2-minute burn-in process to remove contaminates and oxides on the surface.

To improve the conformality of Ge deposition and ensure material penetration through the lattice, sputtering was performed on samples mounted at 90^{o} on an SEM stub on the rotating chuck. In doing so, the side faces of the lattice, namely the (010) and (10$\bar{1}$) surfaces, were directed towards the target, rather than the top of the lattice. With the above mentioned sputtering parameters, we observed a deposition rate of $\sim$0.375 nm/min on the 3D lattice structure, significantly slower than thin film deposition for this set of parameters. Each of the four side faces of the sample were directed towards the target and sputtered in increments of 2 hrs and 46 min, resulting in the deposition of $\sim$250 nm thick Ge shells on the polymer lattice beams. Cross-section cutaways were taken with focused ion beam (FIB) milling to assess the conformality and thickness of germanium deposited onto the polymer lattices. Only the edges of the core-shell PhC were FIB milled to minimize sample damage, revealing beam cross-sections for imaging and measurement with scanning electron microscopy (Figure 6.3c). Figure 6.3d shows a higher magnification image of a 10 μm cross section of the (010) face of our core-shell PhC and shows an average lattice period of 3.8 μm, likely due to structure shrinkage in the TPL DLW process. In Figure 6.3d, we observe: (1) Ge fully coats the beams, but in a non-isotropic manner with a $\sim$200 nm offset in Ge shell position relative to polymer core position, (2) beam cross-sections are elliptical with an average long axis of 1.1 μm, and average short axis of 880 nm, and (3) anisotropic etching of the polymer core is apparent at this cleaning cross-section depth, and can be approximated as elliptical with a short axis of 450 nm and long axis of 650 nm. Subsequent FIB cutting into the depth of the lattice demonstrates that the offset in Ge shell position relative to polymer core position persists through the length of the beam, and the dimensions of the full beam and polymer core do

not vary significantly, remaining elliptical with similar average dimensions as described. Although non-uniform, averaging the polymer core dimensions and comparing them to the full core-shell beam dimensions provides an average Ge shell thickness of 255 nm, sufficient for the observation of negative refractive behavior.

6.4 Optical Characterization of Core-Shell All-Angle Negative Refraction Photonic Crystals

These structures were designed to be probed with mid-IR light and the photonic band structure was experimentally mapped to determine if they exhibited negative refractive index. Band shape determines the shape of the equi-frequency contours and direction of the group velocity vector inside the PhC, and thus the propagation direction of a refracted beam. In a similar manner to the analysis by Luo et al. [122], our simulations aimed at identifying a frequency region for observing AANR focused on band 3, which possesses a concave-down shape indicative of a negative photonic-mass, along the Γ-N (101) direction. The AANR region is found between the point where the band intersects the light line, and the point where band curvature changes. In this frequency region, equi-frency contours (EFCs) will be all-convex and larger than that of air, and the effective refractive index may be regarded as $n_{\text{eff}} \approx -1$. In the frequency region above the light line, where band shape is still concave-down, group velocity continues to be negative, but EFCs will no longer be larger than air. A consequence of this is that effective refractive index will still be negative, but will be between $-1 < n_{\text{eff}} < 0$, and negative refraction will now be angle dependent. The optical experimental characterization tools at our disposal such as FTIR and angle resolved spectroscopy both rely on the coupling of external radiation to PhC leaky modes, which are modes or bands above the light line. Consequently, we were unable to access or observe the PhC AANR region experimentally, but could instead couple into band 3 above the light line, where effective index should still be negative, but angle-dependent.

In order to truly observe and distinguish photonic states, i.e. photonic bands of our 3D core-shell PhCs, angle resolved spectroscopic measurements are required from a set-up that can selectively excite states at precise momentum and wavelengths. This was done in a custom built set-up, and consists of a quantum cascade laser (QCL) with an operating mode between 7.7 μm and 8.62 μm as the source, a series of ZnSe lenses to focus the laser beam down to spot

size approximately 100 μm in diameter, and a Ge beam splitter to direct half of the laser beam to a reference detector, and half to the sample. Pyroelectric sample and reference detectors are mounted on concentric rotation stages allowing for the collection of transmission and reflection spectra at distinct angles of incidence. Alignment of the laser beam and the photonic crystal sample is accomplished using a visible CCD camera and alignment markers. More precise micron scale alignment is performed by transmitting QCL light through the sample, and projecting the magnified image onto a mid-IR camera with MCT detector to determine sample edges versus the sample center.

For the angle resolved reflectance measurements the incident laser light is polarized in the $[10\bar{1}]$ direction relative to the lattice, and interacts with the (101) PhC surface. The angular range covered in the experiments was limited from $\theta = 22.5^{\circ}$ to 45° (where θ is the angle between the incident beam and the normal to the crystal surface) due to limitations of the experimental setup. Specifically, the size of the detector prevents access to angles below 22.5°, and the reflectance single above 45° is too weak due to the smaller effective cross section of the samples at large angles. Fabrication limitations prevented the fabrication of larger structures without incorporating stitching via stage movements in DLW, which would add an additional source of error into these experiments, and thus was avoided.

The band structure of the BCC core-shell PhC is constructed from the angle resolved reflectance spectra captured between 22.5° to 45°. Experimental limitations prevent characterization at normal incidence or near the light line, though the AANR region of the PhC exists below the line and thus cannot be accessed. However, if the curvature of the observable band is concave down, a frequency region with a negative effective index between $-1 < n_{\text{eff}} < 0$ should still exist. The experimentally measured band structure for our core-shell PhC lattice is shown in Figure 6.4a. We observe the emergence of a photonic mode marked by a decrease in reflection intensity (blue) in the region between 7.7 μm and 8.1 μm which has concave-down character, and seems to replicate the appearance of the third band. Reflectance at higher wavelengths is also relatively low between 8.3 μm and 8.62 μm, but this is due to absorption by the PhCs polymer core [127].

For reference, we compare the experimentally derived angle resolved band map in Figure 6.4a to a band structure calculated using PWE in Figure 6.4b.

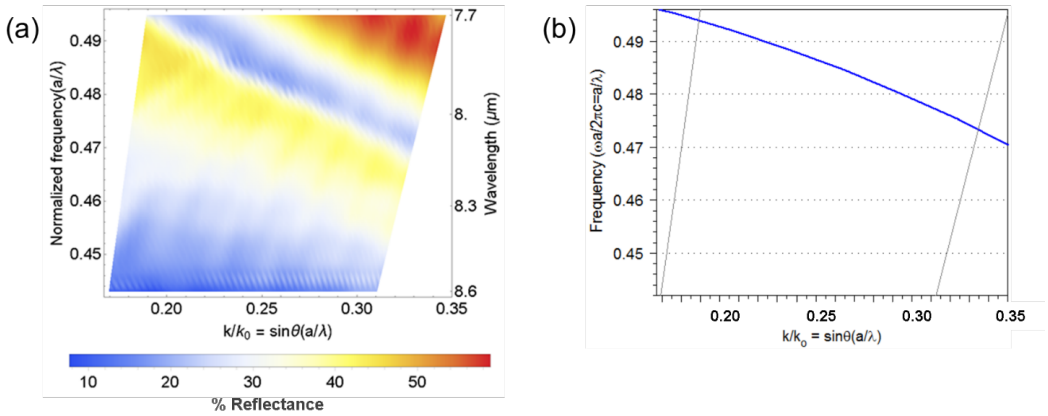

Figure 6.4: Band structures of band 3 in the 3D core-shell PhC found (a) experimentally with angle resolved reflectance measurement and (b) with simulation

The simulated PhC was based on structural features and lattice dimensions determined through FIB and SEM measurements. The unit cell size was set to 3.8 μm, and beam ellipticity, taper, and Ge shell offset were accounted for yielding a representative core-shell PhC for simulation. We calculate the band structure for this PhC approximation in the frequency range between $\omega = 0.441$ $(2\pi c/a)$ and $\omega = 0.494$ $(2\pi c/a)$ and angular span between 22.5° to 45° along the Γ-N direction to match experimental conditions.

The EFCs for the band shown in Figure 6.4a are shown in Figure 6.5a. The PhC contours are nearly circular and decrease in radius as frequency increases, implying that negative refraction should be expected due to the downward concavity of the band. The refraction of an incident wave through the PhC was calculated at $\omega = 0.474$ $(2\pi c/a)$ and the propagation angle was deduced from the EFC shape via the group velocity relation. Figure 6.5b shows the refraction angle versus incident angle for the EFC at this frequency. Specifically at this frequency, incident waves at angles larger than 43° cannot couple to the PhC, and will instead be totally reflected. Snell's law then allows the calculation of the corresponding index for refraction angle. Figure 6.5c plots the effective refractive index as a function of incident angle at this frequency. As the EFC at this frequency is not perfectly circular, effective refractive index is dependent on incident angle. The calculated angle-dependent effective index for our core-shell BCC PhC is negative, with an average value of n_{eff} = -0.67.

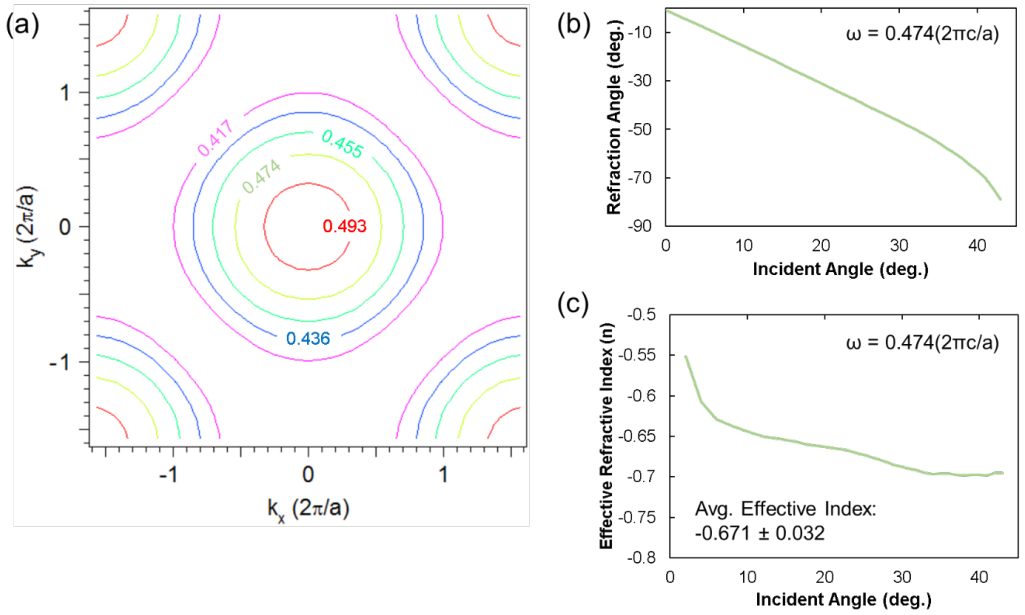

Figure 6.5: EFCs and resulting plots of negative refraction and negative effective index. (a) Slice of the equi-frequency surfaces on plane $k_z = 0$ for band 3 simulated in Figure 6.4c. The highest frequency circle is colored red and lies at the center. Subsequently lower frequencies have larger diameter contours which indicate negative group velocity. (b) Refraction angle versus incident angle for $\omega = 0.474\ (2\pi c/a)$. (c) Effective refractive index as a function of incident angle for $\omega = 0.474\ (2\pi c/a)$.

6.5 Conclusions

We analyzed the dispersion phenomena and negative refraction properties of polymer-germanium core-shell PhCs in the mid-IR using band theory and angle resolved spectroscopy. Band structure calculations were performed to inform the design of the 3D polymer-Ge photonic crystal, which was subsequently fabricated. Its band structure was mapped experimentally and used to calculate the PhC refraction behavior. Analysis of wave-propagation using EFCs revealed that this 3D core-shell PhC will refract light negatively, and possesses an effective negative index of refraction in the region we experimentally mapped. While such a tool is extremely powerful and promises applications such as superlenses for sub-diffraction limit imaging, the extreme fabrication complexity limits its implementation. We can envision that the ability to directly print a Ge structure in TPL DLW could greatly simplify the fabrication process, while also greatly increasing the effective index of the overall structure, and thus relaxing the stringent requirements to observe negative refraction. This is but one area in which the AM process proposed in Chapter 5 could enable more

widescale production of such a structure, or enable fabrication in a more facile or tractable manner.

Chapter 7

CONCLUSIONS AND FUTURE WORK

In this thesis, we utilized both simulation and experiment to design and demonstrate various nanophotonic phenomena in different dielectric PhC systems. We began by discussing the notion of a GMR in 1D and 2D PhCs and proposed their application in spectral imaging due to their ideal spectral characteristics for light filtering. We first studied a 2D nanopillar array HCG system that is lossless, ultra-thin, and possesses spectral characteristics that are on par with existing commercial DBR designs and other state-of-the-art in literature in the near-IR, though our design also possesses many other advantages. We continued this idea and identified the size limitations of existing GMR designs due to the many periods required to observe this phenomenon. We then expanded on this idea and miniaturized our design until we reached pixel sizes and spatial resolutions competitive with commercial filters. We continued to build on our design through further optimizations, increasing the SNR, reducing lateral footprint, and obtaining extremely narrow bandwidths all at the same time. Specifically within this work, further optimization, experimental demonstrations, and even incorporation of new designs such as the mirrorless or tandem designs presented here would further propel this work towards commercial realization. While we focused specifically on the use of GMR-based filters for spectral imaging or spectroscopic applications, the scope of this work can be greatly expanded as these designs have potential and utility as filters or sensors across all areas of research such as biosensing [128, 129], thermoelectrics [130], and photovoltaics [131, 132], to name a few.

We then transitioned to 3D dielectric photonic crystals and fabricated 3D PhCs in TiO_2 using a hybrid organic-inorganic ligand exchange process, characterized their optical band gaps, and demonstrated its advantages over other existing methods for similar fabrication such as CVD or ALD, with relative fabrication simplicity via DLW and the higher effective index of this design due to low porosity within the fully dense material. While TiO_2 was chosen as the model material, the potential of this powerful AM process is much greater in that many different materials can be created as long as a precursor exists that is amenable to this ligand exchange process and that the resulting materials are stable and

can be thermodynamically reduced to their desired form. This process was recently described by Vyatskikh et al. for metals and demonstrated in Nickel [111], though the possible material space with a similar process includes metals, metal oxides, and metal sulfides, which increases the available tools for AM. We studied the specific case where a high-index 3D PhC enables AANR in a 3D Ge structure via dispersion engineering, and discussed how this process could be greatly simplified through the development of a process that allows printing with Ge. One of the more straight-forward, though still extremely complicated techniques to fabricate a high-index 3D structure is the double inversion method previously mentioned, though only one example of such a structure being fabricated in Ge has been shown to date [133]. Expanding on this idea, while the hybrid organic-inorganic ligand exchange process discussed here incorporates metal atoms into the backbone of a polymer, given that precursors amenable to the ligand exchange process exist, an alternative that exists is the use of metal salts that can be dissolved in solution and then calcinated [105]. Such a process could enable direct printing with Ge, but could also enable applications of 3D PhCs in plasmonics or active optoelectronics by enabling the printing of materials such as gold, silver, or vanadium oxide. Thus, the facile fabrication of 3D PhCs in different materials opens the door to more widespread incorporation of 3D PhCs.

REFERENCES

[1] S. V. Gaponenko. *Introduction to nanophotonics*. Cambridge University Press, 2010.

[2] M. A. Butt, S. A. Fomchenkov, and S. N. Khonina. Multilayer dielectric stack notch filter for 450-700 nm wavelength spectrum. *CEUR Workshop Proceedings*, 1900:1–4, 2017. ISSN 16130073. doi: 10.18287/1613-0073-2017-1900-1-4.

[3] E. Sakat, G. Vincent, P. Ghenuche, N. Bardou, S. Collin, F. Pardo, J. Pelouard, and R. Haïdar. Guided mode resonance in subwavelength metallodielectric free-standing grating for bandpass filtering. *Optics Letters*, 36(16):3054–3056, 2011. ISSN 0146-9592. doi: 10.1364/ol.36.003054.

[4] G. A. Golubenko, A. S. Svakhin, V. A. Sychugov, A. V. Tischenko, E. Popov, and L. Mashev. Diffraction characteristics of planar corrugated waveguides. *Optical and Quantum Electronics*, 18:123–128, 1986.

[5] S. S. Wang and R. Magnusson. Theory and applications of guided-mode resonance filters. *Applied optics*, 32(14):2606–2613, 1993. ISSN 0003-6935. doi: 10.1364/AO.32.002606.

[6] S. S. Wang, R. Magnusson, J. S. Bagby, and M. G. Moharam. Guided-mode resonances in planar dielectric-layer diffraction gratings. *Journal of the Optical Society of America A*, 7(8):1470–1474, 1990. ISSN 1084-7529. doi: 10.1364/JOSAA.7.001470.

[7] R. Magnusson. Wideband reflectors with zero-contrast gratings. *Optics Letters*, 39(15):4337–4340, 2014.

[8] M. Shokooh-Saremi and R. Magnusson. Properties of two-dimensional resonant reflectors with zero-contrast gratings. *Optics Letters*, 39(24):6958–6961, 2014. ISSN 0146-9592. doi: 10.1364/OL.39.006958. URL `http://ol.osa.org/abstract.cfm?URI=ol-39-24-6958{\%}5Cnhttps://www.osapublishing.org/abstract.cfm?URI=ol-39-24-6958`.

[9] C. J. Chang-Hasnain and W. Yang. High-contrast gratings for integrated optoelectronics. *Advances in Optics and Photonics*, 4:379–440, 2012. doi: 10.1364/AOP.4.000379.

[10] C. F. R. Mateus, M. C. Y. Huang, Y. Deng, A. R. Neureuther, and C. J. Chang-hasnain. Ultrabroadband mirror using low-index cladded subwavelength grating. *IEEE Photonics Technology Letters*, 16(2):518–520, 2004.

[11] C. F. R. Mateus, M. C. Y. Huang, L. Chen, C. J. Chang-Hasnain, and Y. Suzuki. Broad-band mirror (1.12-1.62 μm) using a subwavelength grating. *IEEE Photonics Technology Letters*, 16(7):1676–1678, 2004.

[12] E. Yablonovitch, T. J. Gmitter, and K. M. Leung. Photonic band structure: The face-centered-cubic case employing nonspherical atoms. *Physical Review Letters*, 67(17):2295–2298, 1991. ISSN 00319007. doi: 10.1103/PhysRevLett.67.2295.

[13] E. Yablonovitch. Inhibited spontaneous emission in solid-state physics and electronics. *Physical Review Letters*, 58(20):2059–2062, 1987. doi: https://doi.org/10.1103/PhysRevLett.58.2059.

[14] S. John. Strong localization of photons in certain disordered dielectric superlattices. *Physical Review Letters*, 58(23):2486–2489, 1987. ISSN 00319007. doi: 10.1103/PhysRevLett.58.2486.

[15] K. M. Ho, C. T. Chan, and C. M. Soukoulis. Existence of a photonic gap in periodic dielectric structures. *Physical Review Letters*, 65(25): 3152–3155, 1990. ISSN 00319007. doi: 10.1103/PhysRevLett.65.3152.

[16] I. Leifer, W. J. Lehr, D. Simecek-beatty, E. Bradley, R. Clark, P. Dennison, Y. Hu, S. Matheson, C. E. Jones, B. Holt, M. Reif, D. A. Roberts, J. Svejkovsky, G. Swayze, and J. Wozencraft. State of the art satellite and airborne marine oil spill remote sensing: Application to the BP Deepwater Horizon oil spill. *Remote Sensing of Environment*, 124:185–209, 2012. ISSN 0034-4257. doi: 10.1016/j.rse.2012.03.024. URL `http://dx.doi.org/10.1016/j.rse.2012.03.024`.

[17] M. Fingas and C. E. Brown. *Oil spill remote sensing: A review*. Elsevier Inc., 2011. ISBN 9781856179430. doi: 10.1016/B978-1-85617-943-0.10006-1. URL `http://dx.doi.org/10.1016/B978-1-85617-943-0.10006-1`.

[18] T. Slonecker, G. B. Fisher, D. P. Aiello, and B. Haack. Visible and infrared remote imaging of hazardous waste: A review. *Remote Sensing*, 2:2474–2508, 2010. doi: 10.3390/rs2112474.

[19] D. J. Williams, B. L. Feldman, T. J. Williams, D. Pilant, P. G. Lucey, and L. D. Worthy. Detection and identification of toxic air pollutants using airborne LWIR hyperspectral imaging. *Proc. of SPIE*, 5655, 2005. doi: 10.1117/12.578819.

[20] R. G. Vaughan, W. M. Calvin, and J. V. Taranik. SEBASS hyperspectral thermal infrared data: surface emissivity measurement and mineral mapping. *Remote Sensing of Environment*, 85:48–63, 2003. doi: 10.1016/S0034-4257(02)00186-4.

[21] P. G. Lucey, T. Williams, M. Mignard, J. Julian, D. Kokobun, G. Allen, D. Hampton, W. Schaff, M. Schlangen, E. M. Winter, W. Kendali, A. Stocker, K. Horton, and A. P. Bowman. AHI: An airborne long wave infrared hyperspectral imager. *Proceedings of the SPIE*, 3431:36–43, 1998.

[22] R. M. Levenson and J. R. Mansfield. Multispectral imaging in biology and medicine: Slices of life. *Cytometry Part A*, 69:748–758, 2006. ISSN 15524922. doi: 10.1002/cyto.a.20319.

[23] T. Zimmermann, J. Rietdorf, and R. Pepperkok. Spectral imaging and its applications in live cell microscopy. *FEBS Letters*, 546:87–92, 2003. ISSN 00145793. doi: 10.1016/S0014-5793(03)00521-0.

[24] S. Marshall, T. Kelman, T. Qiao, P. Murray, and J. Zabalza. Hyperspectral imaging for food applications. *Signal Processing Conference (EUSIPCO)*, pages 2854–2858, 2015.

[25] Y.-Z. Feng and D.-W. Sun. Application of hyperspectral imaging in food safety inspection and control: A review. *Critical Reviews in Food Science and Nutrition*, 52(11):1039–1058, 2012. doi: 10.1080/10408398.2011.651542.

[26] R. Lu and Y.-R. Chen. Hyperspectral imaging for safety inspection of food and agricultural products. *Proc. of SPIE*, 3544:121–133, 1998. doi: 10.1117/12.335771.

[27] P. W. T. Yuen and M. Richardson. An introduction to hyperspectral imaging and its application for security, surveillance and target acquisition. *The Imaging Science Journal*, 58:241–254, 2010. doi: 10.1179/174313110X12771950995716.

[28] W.-Y. Jang, Z. Ku, A. Urbas, J. Derov, and M. J. Noyola. Plasmonic superpixel sensor for compressive spectral sensing. *IEEE Transactions on Geoscience and Remote Sensing*, 53(6):3471–3480, 2015.

[29] W.-Y. Jang, Z. Ku, J. Jeon, J. O. Kim, S. J. Lee, J. Park, M. J. Noyola, and A. Urbas. Experimental demonstration of adaptive infrared multispectral imaging using plasmonic filter array. *Scientific Reports*, 6: 1–9, 2016. doi: 10.1038/srep34876. URL `http://dx.doi.org/10.1038/srep34876`.

[30] J. A. Hackwell, D. W. Warren, R. P. Bongiovi, S. J. Hansel, T. L. Hayhurst, J. Dan, M. G. Sivjee, and J. W. Skinner. LWIR/MWIR imaging hyperspectral sensor for airborne and ground-based remote sensing. *Proceedings of the SPIE*, 2819(1):102–107, 1996.

[31] G. A. Shaw and H.-H. K. Burke. Spectral imaging for remote sensing. *Lincoln Laboratory Journal*, 14(1):3–28, 2003.

[32] N. Gat, S. Subramanian, J. Barhen, and N. Toomarian. Spectral imaging applications: remote sensing, environmental monitoring, medicine, military operations, factory automation, and manufacturing. *Proc. of SPIE*, 2962:63–77, 1997. doi: 10.1117/12.267840.

[33] Y. Huo, C. C. Fesenmaier, and P. B. Catrysse. Microlens performance limits in sub-2um pixel CMOS image sensors. *Optics Express*, 18(6):5861–5872, 2009. ISSN 1094-4087. doi: 10.1117/12.807007. URL `http://proceedings.spiedigitallibrary.org/proceeding.aspx?doi=10.1117/12.807007`.

[34] C. C. Fesenmaier, Y. Huo, and P. B. Catrysse. Effects of imaging lens f-number on sub-2 m CMOS image sensor pixel performance. *Proc. of SPIE*, 2009. ISSN 0277786X. doi: 10.1117/12.807011. URL `http://proceedings.spiedigitallibrary.org/proceeding.aspx?doi=10.1117/12.807011`.

[35] F. Flory and A. Piegari. *Optical thin films and coatings: From materials to applications*. Cambridge:Woodhead Publishing, 2013.

[36] Y. Gu, L. Zhang, J. K. W. Yang, P. Yeo, and C.-W. Qiu. Color generation via subwavelength plasmonic nanostructures. *Nanoscale*, 7:6409–6419, 2015. doi: 10.1039/c5nr00578g.

[37] S. Yokogawa, S. P. Burgos, and H. A. Atwater. Plasmonic color filters for CMOS image sensor applications. *Nano Letters*, 12:4349–4354, 2012. doi: 10.1021/nl302110z.

[38] S. P. Burgos, S. Yokogawa, and H. A. Atwater. Color imaging via nearest neighbor hole coupling in plasmonic color filters integrated onto a complementary metal-oxide semiconductor image sensor. *ACS Nano*, 7 (11):10038–10047, 2013. ISSN 19360851. doi: 10.1021/nn403991d.

[39] T. Xu, Y.-K. Wu, X. Luo, and L. J. Guo. Plasmonic nanoresonators for high-resolution colour filtering and spectral imaging. *Nature Communications*, 1(5):1–5, 2010. ISSN 2041-1723. doi: 10.1038/ncomms1058. URL `http://www.nature.com/doifinder/10.1038/ncomms1058`.

[40] D. Fleischman, L. A. Sweatlock, H. Murakami, and H. Atwater. Hyper-selective plasmonic color filters. *Opt. Express*, 25(22):27386–27395, 2017. ISSN 10944087. doi: 10.1364/OE.25.027386. URL `http://www.opticsexpress.org/abstract.cfm?URI=oe-25-22-27386`.

[41] Q. Chen, D. Chitnis, K. Walls, T. D. Drysdale, S. Collins, and D. R. S. Cumming. CMOS photodetectors integrated With plasmonic color filters. *IEEE Photonics Technology Letters*, 24(3):197–199, 2012.

[42] X. Buet, E. Daran, D. Belharet, F. Lozes-Dupuy, A. Monmayrant, and O. Gauthier-Lafaye. High angular tolerance and reflectivity with narrow bandwidth cavity-resonator-integrated guided-mode resonance filter. *Optics Express*, 20(8):9322, 2012. ISSN 1094-4087. doi: 10.1364/OE.20.009322. URL `https://www.osapublishing.org/oe/abstract.cfm?uri=oe-20-8-9322`.

[43] E.-H. Cho, H.-S. Kim, B.-H. Cheong, O. Prudnikov, W. Xianyua, J.-S. Sohn, D.-J. Ma, H.-Y. Choi, N.-C.l Park, and Y.-P. Park. Two-dimensional photonic crystal color filter development. *Optics express*, 17 (10):8621–8629, 2009. ISSN 1094-4087. doi: 10.1364/OE.17.008621.

[44] B. H. Cheong, O. N. Prudnikov, E. Cho, H. S. Kim, J. Yu, Y. S. Cho, H. Y. Choi, and S. T. Shin. High angular tolerant color filter using subwavelength grating. *Applied Physics Letters*, 94(21):5–8, 2009. ISSN 00036951. doi: 10.1063/1.3139058.

[45] M. Niraula, J. W. Yoon, and R. Magnusson. Single-layer optical bandpass filter technology. *Optics Letters*, 40(21):5062–5065, 2015. ISSN 0146-9592. doi: 10.1364/OL.40.005062. URL `https://www.osapublishing.org/abstract.cfm?URI=ol-40-21-5062`.

[46] D. W. Peters, R. R. Boye, J. R. Wendt, R. A. Kellogg, S. A. Kemme, T. R. Carter, and S. Samora. Demonstration of polarization-independent resonant subwavelength grating filter arrays. *Optics Express*, 35(19): 3201–3203, 2010.

[47] V. Karagodsky, F. G. Sedgwick, and C. J. Chang-Hasnain. Theoretical analysis of subwavelength high contrast grating reflectors. *Optics express*, 18(16):16973–16988, 2010. ISSN 1094-4087. doi: 10.1364/OE.18.016973.

[48] P. Lalanne, J. P. Hugonin, and P. Chavel. Optical properties of deep lamellar gratings: A coupled bloch-mode insight. *Journal of Lightwave Technology*, 24(6):2442–2449, 2006. ISSN 07338724. doi: 10.1109/JLT.2006.874555.

[49] P. P. Iyer, N. A. Butakov, and J. A. Schuller. Reconfigurable semiconductor phased-array metasurfaces. *ACS Photonics*, 2:1077–1084, 2015. doi: 10.1021/acsphotonics.5b00132.

[50] B. C. P. Sturmberg, K. B. Dossou, L. C. Botten, R. C. McPhedran, and C. Martijn de Sterke. Fano resonances of dielectric gratings: symmetries and broadband filtering. *Optics Express*, 23(24):1672–1686, 2015. ISSN 1094-4087. doi: 10.1364/OE.23.0A1672. URL `http://www.osapublishing.org/viewmedia.cfm?uri=oe-23-24-A1672{\&}seq=0{\&}html=true{\%}5Cnhttps://www.osapublishing.org/abstract.cfm?URI=oe-23-24-A1672`.

[51] Y. Horie, A. Arbabi, E. Arbabi, S. M. Kamali, and A. Faraon. Wide bandwidth and high resolution planar filter array based on DBR-metasurface-DBR structures. *Optics express*, 24(11):1–6, 2016. ISSN 10944087. doi: 10.1364/OE.24.011677. URL `http://arxiv.org/abs/1604.03167`.

[52] Y. Horie, S. Han, J. Y. Lee, J. Kim, Y. Kim, A. Arbabi, C. Shin, L. Shi, E. Arbabi, S. M. Kamali, H. S. Lee, S. Hwang, and A. Faraon. Visible wavelength color filters using dielectric subwavelength gratings for backside-illuminated CMOS image sensor technologies. *Nano Letters*, 17 (5):3159–3164, 2017. ISSN 15306992. doi: 10.1021/acs.nanolett.7b00636.

[53] L. Cao, P. Fan, E. S. Barnard, A. M. Brown, and M. L. Brongersma. Tuning the color of silicon nanostructures. *Nano Letters*, 10(7):2649–2654, 2010. ISSN 15306984. doi: 10.1021/nl1013794.

[54] J. Proust, F. Bedu, B. Gallas, I. Ozerov, and N. Bonod. All-dielectric colored metasurfaces with silicon mie resonators. *ACS Nano*, 10(8): 7761–7767, 2016. ISSN 1936086X. doi: 10.1021/acsnano.6b03207.

[55] N. Yu and F. Capasso. Flat optics with designer metasurfaces. *Nature Materials*, 13(2):139–150, 2014. ISSN 14764660. doi: 10.1038/nmat3839.

[56] S. Jahani and Z. Jacob. All-dielectric metamaterials. *Nature Nanotechnology*, 11(1):23–36, 2016. ISSN 17483395. doi: 10.1038/nnano.2015.304. URL `http://dx.doi.org/10.1038/nnano.2015.304`.

[57] A. V. Kildishev, A. Boltasseva, and V. M. Shalaev. Planar photonics with metasurfaces. *Nature Materials*, 339, 2012. ISSN 14764660. doi: 10.1038/nmat3431.

[58] S. A. Kemme, D. A. Scrymgeour, and D. W. Peters. High efficiency diffractive optical elements for spectral beam combining. *Laser Technology for Defense and Security VIII*, 8381, 2012. doi: 10.1117/12.919593. URL `http://proceedings.spiedigitallibrary.org/proceeding.aspx?doi=10.1117/12.919593`.

[59] K. Hehl, J. Bischoff, U. Mohaupt, M. Palme, B. Schnabel, L. Wenke, R. Bodefeld, W. Theobald, E. Welsch, R. Sauerbrey, and H. Heyer. High-efficiency dielectric reflection gratings: design, fabrication, and analysis. *Applied Optics*, 38(30):6257–6271, 1999.

[60] L. Mashev and E. Popov. Zero order anomaly of dielectric coated gratings. *Optics Communications*, 55(6):377–380, 1985.

[61] M. T. Gale, K. Knop, and R. Morf. Zero-order diffractive microstructures for security applications. *SPIE Optical Security and Anticounterfeiting Systems*, 1210:83–89, 1990.

[62] K. Ikeda, K. Takeuchi, K. Takayose, I.-S. Chung, J. Mørk, and H. Kawaguchi. Polarization-independent high-index contrast grating and its fabrication tolerances. *Applied optics*, 52(5):1049–1053, 2013. ISSN 1539-4522. doi: 10.1364/AO.52.001049. URL `http://www.ncbi.nlm.nih.gov/pubmed/23400067`.

[63] A. Maurel, S. Félix, J. F. Mercier, A. Ourir, and Z. E. Djeffal. Wood's anomalies for arrays of dielectric scatterers. *Journal of the European Optical Society*, 9:1–7, 2014. ISSN 19902573. doi: 10.2971/jeos.2014.14001.

[64] R. F. Kazarinov, Z. N. Sokolova, and R. A. Suris. Planar distributed-feedback optical resonators. *Soviet physics, Technical physics*, 21(2):130–136, 1976.

[65] Y. Ding and R. Magnusson. Band gaps and leaky-wave effects in resonant photonic-crystal waveguides. *Optics express*, 15(2):680–694, 2007. ISSN 1094-4087. doi: 10.1364/OE.15.000680.

[66] S. T. Peng. Rigorous formulation of scattering and guidance by dielectric grating waveguides: general case of oblique incidence. *Journal of the Optical Society of America A*, 6(12):1869–1883, 1989.

[67] K. Walls, Q. Chen, J. Grant, S. Collins, D. R. S. Cumming, and T. D. Drysdale. Narrowband multispectral filter set for visible band. *Optics Express*, 20(20):7152–7158, 2012. doi: 10.1007/s11468-012-9360-6.

[68] Y. Kanamori, M. Shimono, and K. Hane. Fabrication of transmission color filters using silicon subwavelength gratings on quartz substrates. *IEEE Photonics Technology Letters*, 18(20):2126–2128, 2006.

[69] D. L. Brundrett, E. N. Glytsis, and T. K. Gaylord. Normal-incidence guided-mode resonant grating filters: design and experimental demonstration. *Optics Letters*, 23(9):700–702, 1998.

[70] J.-N. Liu, M. V. Schulmerich, R. Bhargava, and B. T. Cunningham. Optimally designed narrowband guided-mode resonance reflectance filters for mid-infrared spectroscopy. *Optics Express*, 19(24):219–226, 2011.

[71] T. Clausnitzer, J. Limpert, K. Zöllner, H. Zellmer, H.-J. Fuchs, E.-B. Kley, A. Tünnermann, M. Jupé, and D. Ristau. Highly efficient transmission gratings in fused silica for chirped-pulse amplification systems. *Applied Optics*, 42(34):6934–6938, 2003. ISSN 0003-6935. doi: 10.1364/AO.42.006934. URL `https://www.osapublishing.org/abstract.cfm?URI=ao-42-34-6934`.

[72] B. W. Shore, M. D. Perry, J. A. Britten, R. D. Boyd, M. D. Feit, H. T. Nguyen, R. Chow, G. E. Loomis, and L. Li. Design of high-efficiency

dielectric reflection gratings. *Journal of the Optical Society of America A*, 14(5):1124–1136, 1997. ISSN 1084-7529. doi: 10.1364/JOSAA.14.001124.

[73] R. Magnusson and Y. H. Ko. Guided-mode resonance nanophotonics: fundamentals and applications. *Proc. of SPIE*, 9927, 2016. doi: 10.1117/12.2237973.

[74] R. C. Ng, J. R. Greer, and K. T. Fountaine. Fabrication of ultra-thin si nanopillar arrays for polarization-independent spectral filters in the near-IR. *Proc. of SPIE*, 10541, 2018. doi: 10.1117/12.2286804. URL `https://www.spiedigitallibrary.org/conference-proceedings-of-spie/10541/2286804/Fabrication-of-ultra-thin-si-nanopillar-arrays-for-polarization-independent/10.1117/12.2286804.full`.

[75] R. C. Ng, J. C. Garcia, J. R. Greer, and K. T. Fountaine. Polarization-independent, narrowband, near-IR spectral filters via guided mode resonances in ultrathin a-Si nanopillar arrays. *ACS Photonics*, 6(2):265–271, 2019. ISSN 23304022. doi: 10.1021/acsphotonics.8b01253.

[76] M. D. Henry. *ICP etching of silicon for micro and nanoscale devices*. PhD thesis, California Institute of Technology, 2010. URL `http://resolver.caltech.edu/CaltechTHESIS:05262010-152815609`.

[77] D. Fleischman. *Nanophotonic structures: fundamentals and applications in narrowband transmission color filtering*. PhD thesis, California Institute of Technology, 2019.

[78] R. R. Boye and R. K. Kostuk. Investigation of the effect of finite grating size on the performance of guided-mode resonance filters. *Applied Optics*, 39(21):3649–3653, 2000. ISSN 0003-6935. doi: 10.1364/ao.39.003649.

[79] D. K. Jacob, S. C. Dunn, and M. G. Moharam. Design considerations for narrow-band dielectric resonant grating reflection filters of finite length. *Journal of the Optical Society of America A*, 17(7):1241–1249, 2000. ISSN 1084-7529. doi: 10.1364/josaa.17.001241.

[80] J. M. Bendickson, E. N. Glytsis, T. K. Gaylord, and D. L. Brundrett. Guided-mode resonant subwavelength gratings: effects of finite beams and finite gratings. *Journal of the Optical Society of America A*, 18(8):1912–1928, 2001. ISSN 1084-7529. doi: 10.1364/josaa.18.001912.

[81] A. Liu, W. Hofmann, and D. Bimberg. Two dimensional analysis of finite size high-contrast gratings for applications in VCSELs. *Optics Express*, 22(10):11804–11811, 2014. ISSN 1094-4087. doi: 10.1364/OE.22.011804. URL `https://www.osapublishing.org/oe/abstract.cfm?uri=oe-22-10-11804`.

[82] I.-R. Johansen, J. O. Grepstad, M. M. Greve, O. Solgaard, A. Sudbø, and B. Holst. Finite-size limitations on quality factor of guided resonance modes in 2D photonic crystals. *Optics Express*, 21(20):23640–23654, 2013. doi: 10.1364/oe.21.023640.

[83] D. Fleischman, K. T. Fountaine, C. R. Bukowsky, G. Tagliabue, L. A. Sweatlock, and H. A. Atwater. High spectral resolution plasmonic color filters with subwavelength dimensions. *ACS Photonics*, 6:332–338, 2019. ISSN 23304022. doi: 10.1021/acsphotonics.8b01634.

[84] Y. Zhou, M. Moewe, J. Kern, M. C. Y. Huang, and C. J. Chang-Hasnain. Surface-normal emission of a high-Q resonator using a subwavelength high-contrast grating. *Optics Express*, 16(22):17282–17287, 2008. doi: 10.1364/oe.16.017282.

[85] S. Ura, S. Murata, Y. Awatsuji, and K. Kintaka. Design of resonance grating coupler. *Optics Express*, 16(16):12207–12213, 2008. doi: 10.1364/oe.16.012207.

[86] K. Kintaka, Y. Kita, K. Shimizu, H. Matsuoka, S. Ura, and J. Nishii. Cavity-resonator-integrated grating input/output coupler for high-efficiency vertical coupling with a small aperture. *Optics letters*, 35 (12):1989–1991, 2010. ISSN 1539-4794. doi: 10.1364/OL.35.001989. URL `http://www.ncbi.nlm.nih.gov/pubmed/20548362`.

[87] K. Kintaka, T. Majima, J. Inoue, K. Hatanaka, and J. Nishii. Cavity-resonator-integrated guided-mode resonance filter for aperture miniaturization. *Optics Express*, 20(2):1444–1449, 2012.

[88] K. Kintaka, T. Majima, K. Hatanaka, J. Inoue, and S. Ura. Polarization-independent guided-mode resonance filter with cross-integrated waveguide resonators. *Optics Letters*, 37(15):3264–3266, 2012.

[89] R. Laberdesque, O. Gauthier-Lafaye, H. Camon, A. Monmayrant, M. Petit, O. Demichel, and B. Cluzel. High-order modes in cavity-resonator-integrated guided-mode resonance filters (CRIGFs). *Journal of the Optical Society of America A*, 32(11):1973–1981, 2015. ISSN 1084-7529. doi: 10.1364/JOSAA.32.001973.

[90] J. Inoue, A. Tsuji, K. Kintaka, K. Nishio, and S. Ura. Wavelength division multiplexer based on resonance filters for a compact multi- wavelength light source. *Optics Express*, 26(3):1874–1879, 2018.

[91] J. H. Barton, R. C. Rumpf, R. W. Smith, C. Kozikowski, and P. Zellner. All-dielectric frequency selective surfaces with few number of periods. *Progress In Electromagnetics Research B*, 41:269–283, 2012.

[92] C. Audet, S. Le Digabel, C. Tribes, and V. Rochon Montplaisir. The NOMAD project. URL `https://www.gerad.ca/nomad`.

[93] S. Le Digabel. Algorithm 909: NOMAD: Nonlinear optimization with the MADS algorithm. *ACM Transactions on Mathematical Software*, 37 (4):1–15, 2011. ISSN 00983500. doi: 10.1145/1916461.1916468.

[94] K. Diest, L. A. Sweatlock, and D. E. Marthaler. Metamaterials design using gradient-free numerical optimization. *Journal of Applied Physics*, 108(8), 2010. ISSN 00218979. doi: 10.1063/1.3498816.

[95] L. Mace, O. Gauthier-Lafaye, A. Monmayrant, and H. Camon. Zero-contrast grating filters for pixelated applications in the mid-ir range. *Journal of the Optical Society of America A*, 34(4):657–665, 2017. ISSN 15208532. doi: 10.1364/JOSAA.34.000657.

[96] Ge Photodiode. URL `www.thorlabs.com`.

[97] S. Takahashi, K. Suzuki, M. Okano, M. Imada, T. Nakamori, Y. Ota, K. Ishizaki, and S. Noda. Direct creation of three-dimensional photonic crystals by a top-down approach. *Nature Materials*, 8(9):721–725, 2009. ISSN 14764660. doi: 10.1038/nmat2507.

[98] K. Aoki, D. Guimard, M. Nishioka, M. Nomura, S. Iwamoto, and Y. Arakawa. Coupling of quantum-dot light emission with a three-dimensional photonic-crystal nanocavity. *Nature Photonics*, 2(11):688–692, 2008. ISSN 17494885. doi: 10.1038/nphoton.2008.202.

[99] I. Staude, M. Thiel, S. Essig, C. Wolff, K. Busch, G. Von Freymann, and M. Wegener. Woodpile photonic crystals with a complete bandgap reaching telecom wavelengths. *Optics Letters*, 35(7):1094–1096, 2010. ISSN 21622701. doi: 10.1364/cleo.2010.cths1.

[100] A. Frölich, J. Fischer, T. Zebrowski, K. Busch, and M. Wegener. Titania woodpiles with complete three-dimensional photonic bandgaps in the visible. *Advanced Materials*, 25(26):3588–3592, 2013. ISSN 09359648. doi: 10.1002/adma.201300896.

[101] L. Jonušauskas, D. Gailevičius, L. Mikoliunaite, D. Sakalauskas, S. Šakirzanovas, S. Juodkazis, and M. Malinauskas. Optically clear and resilient free-form μ-optics 3D-printed via ultrafast laser lithography. *Materials*, 10(1):1–18, 2017. ISSN 19961944. doi: 10.3390/ma10010012.

[102] C. C. Yeh, H. C. Liu, W. Heni, D. Berling, H. W. Zan, and O. Soppera. Chemical and structural investigation of zinc-oxo cluster photoresists for DUV lithography. *Journal of Materials Chemistry C*, 5(10):2611–2619, 2017. ISSN 20507526. doi: 10.1039/C6TC05201K.

[103] M. Malinauskas, A. Ukauskas, V. Purlys, A. Gaidukeviiut, Z. Baleviius, A. Piskarskas, C. Fotakis, S. Pissadakis, D. Gray, R. Gadonas, M. Vamvakaki, and M. Farsari. 3D microoptical elements formed in a

photostructurable germanium silicate by direct laser writing. *Optics and Lasers in Engineering*, 50(12):1785–1788, 2012. ISSN 01438166. doi: 10.1016/j.optlaseng.2012.07.001.

[104] S. Wong, M. Deubel, F. Pérez-Willard, S. John, G. A. Ozin, M. Wegener, and G. Von Freymann. Direct laser writing of three-dimensional photonic crystals with a complete photonic bandgap in chalcogenide glasses. *Advanced Materials*, 18(3):265–269, 2006. ISSN 09359648. doi: 10.1002/adma.200501973.

[105] D. W. Yee, M. L. Lifson, B. W. Edwards, and J. R. Greer. Additive manufacturing of 3D-architected multifunctional metal oxides. *Advanced Materials*, 1901345:1–9, 2019. ISSN 15214095. doi: 10.1002/adma.201901345.

[106] C. Mille, E. C. Tyrode, and R. W. Corkery. 3D titania photonic crystals replicated from gyroid structures in butterfly wing scales: Approaching full band gaps at visible wavelengths. *RSC Advances*, 3(9):3109–3117, 2013. ISSN 20462069. doi: 10.1039/c2ra22506a.

[107] E. B. Duoss, M. Twardowski, and J. A. Lewis. Sol-gel inks for direct-write assembly of functional oxides. *Advanced Materials*, 19(21):3485–3489, 2007. ISSN 09359648. doi: 10.1002/adma.200701372.

[108] S. Passinger, M. S. M. Saifullah, C. Reinhardt, K. R. V. Subramanian, B. N. Chichkov, and M. E. Welland. Direct 3D patterning of TiO_2 using femtosecond laser pulses. *Advanced Materials*, 19(9):1218–1221, 2007. ISSN 09359648. doi: 10.1002/adma.200602264.

[109] S. Y. Yu, G. Schrodj, K. Mougin, J. Dentzer, J. P. Malval, H. W. Zan, O. Soppera, and A. Spangenberg. Direct laser writing of crystallized TiO 2 and TiO 2 /carbon microstructures with tunable conductive properties. *Advanced Materials*, 30(51):1–8, 2018. ISSN 15214095. doi: 10.1002/adma.201805093.

[110] A. Vyatskikh, R. C. Ng, B. Edwards, and J. R. Greer. Additive manufacturing of titanium dioxide for dielectric photonic crystals. *Proc. of SPIE*, 10930, 2019. doi: 10.1117/12.2507076.

[111] A. Vyatskikh, S. Delalande, A. Kudo, X. Zhang, C. M. Portela, and J. R. Greer. Additive manufacturing of 3D nano-architected metals. *Nature communications*, 9(1), 2018. ISSN 20411723. doi: 10.1038/s41467-018-03071-9. URL `http://dx.doi.org/10.1038/s41467-018-03071-9`.

[112] M. P. C. Taverne, Y.-L. D. Ho, and J. G. Rarity. Investigation of defect cavities formed in three-dimensional woodpile photonic crystals. *Journal of the Optical Society of America B*, 32(4), 2015. ISSN 0740-3224. doi: 10.1364/josab.32.000639.

[113] O. Frank, M. Zukalova, B. Laskova, J. Kürti, J. Koltai, and L. Kavan. Raman spectra of titanium dioxide (anatase, rutile) with identified oxygen isotopes (16, 17, 18). *Physical Chemistry Chemical Physics*, 14(42):14567–14572, 2012. ISSN 14639076. doi: 10.1039/c2cp42763j.

[114] X. Z. Ding, Z. A. Qi, and Y. Z. He. Effect of tin dioxide doping on rutile phase formation in sol-gel-derived nanocrystalline titania powders. *Nanostructured Materials*, 4(6):663–668, 1994. ISSN 09659773. doi: 10.1016/0965-9773(94)90018-3.

[115] J. D. Joannopoulos, S. G. Johnson, J. N. Winn, and R. D. Meade. *Photonic crystals molding the flow of light*. Princeton University Press, 2nd edition, 2008.

[116] Veselago, V. G. The electrodynamics of substances with simultaneously negative values of ϵ and μ. *Soviet Physics Uspekhi*, 10(4):509–514, 1968.

[117] J. B. Pendry, A. J. Holden, D. J. Robbins, and W. J. Stewart. Magnetism from conductors and enhanced nonlinear phenomena. *IEEE Transactions on Microwave Theory and Techniques*, 47(11):2075–2084, 1999. ISSN 00189480. doi: 10.1109/22.798002.

[118] J. B. Pendry, A. J. Holden, W. J. Stewart, and I. Youngs. Extremely low frequency plasmons in metallic mesostructures. *Physical Review Letters*, 76(25):4773–4776, 2001.

[119] C. M. Soukoulis, S. Linden, and M. Wegener. Negative refractive index at optical wavelengths. *Science*, 315(5808):47–49, 2007. ISSN 00368075. doi: 10.1126/science.1136481.

[120] V. M. Shalaev. Optical negative-index metamaterials. *Nature Photonics*, 1(1):41–48, 2007. ISSN 17494885. doi: 10.1038/nphoton.2006.49.

[121] M. Notomi. Theory of light propagation in strongly modulated photonic crystals: Refraction-like behavior in the vicinity of the photonic band gap. *Physical Review B*, 62(16):10696–10705, 2000. ISSN 01631829. doi: 10.1103/PhysRevB.62.10696.

[122] C. Luo, S. G. Johnson, and J. D. Joannopoulos. All-angle negative refraction in a three-dimensionally periodic photonic crystal. *Applied Physics Letters*, 81(13):2352–2354, 2002. ISSN 00036951. doi: 10.1063/1.1508807.

[123] C. Luo, S. G. Johnson, J. D. Joannopoulos, and J. B. Pendry. All-angle negative refraction without negative effective index. *Physical Review B*, 65(20), 2002. ISSN 1550235X. doi: 10.1103/PhysRevB.65.201104.

[124] E. Cubukcu, K. Aydin, E. Ozbay, S. Foteinopoulou, and C. M. Soukoulis. Subwavelength resolution in a two-dimensional photonic-crystal-based superlens. *Physical Review Letters*, 91(20):1–4, 2003. ISSN 10797114. doi: 10.1103/PhysRevLett.91.207401.

[125] Z. Lu, J. A. Murakowski, C. A. Schuetz, S. Shi, G. J. Schneider, and D. W. Prather. Three-dimensional subwavelength imaging by a photonic-crystal flat lens using negative refraction at microwave frequencies. *Physical Review Letters*, 95(15):2–5, 2005. ISSN 00319007. doi: 10.1103/PhysRevLett.95.153901.

[126] Z. Lu, S. Shi, C. A. Schuetz, J. A. Murakowski, and D. W. Prather. Three-dimensional photonic crystal flat lens by full 3D negative refraction. *Optics Express*, 13(15):5592–5599, 2005. ISSN 1094-4087. doi: 10.1364/opex.13.005592.

[127] V. F. Chernow, H. Alaeian, J. A. Dionne, and J. R. Greer. Polymer lattices as mechanically tunable 3-dimensional photonic crystals operating in the infrared. *Applied Physics Letters*, 107(10), 2015. ISSN 00036951. doi: 10.1063/1.4930819. URL `http://dx.doi.org/10.1063/1.4930819`.

[128] R. Magnusson, B. R. Wenner, J. W. Allen, M. S. Allen, S. Gimlin, K. J. Lee, D. W. Weidanz, H. Hemmati, and Y. H. Ko. The guided-mode resonance biosensor: principles, technology, and implementation. *Proc. of SPIE*, 10510, 2018. ISSN 16057422. doi: 10.1117/12.2288795.

[129] G. J. Triggs, Y. Wang, C. P. Reardon, M. Fischer, G. J. O. Evans, and T. F. Krauss. Chirped guided-mode resonance biosensor. *Optica*, 4(2): 229–234, 2017. ISSN 2334-2536. doi: 10.1364/optica.4.000229.

[130] K. W. Mauser, S. Kim, S. Mitrovic, D. Fleischman, R. Pala, K. C. Schwab, and H. A. Atwater. Resonant thermoelectric nanophotonics. *Nature Nanotechnology*, 12(8):770–775, 2017. ISSN 17483395. doi: 10.1038/nnano.2017.87.

[131] T. Khaleque and R. Magnusson. Light management through guided-mode resonances in thin-film silicon solar cells. *Journal of Nanophotonics*, 8 (1), 2014. ISSN 1934-2608. doi: 10.1117/1.jnp.8.083995.

[132] Y.-C. Lee, C.-F. Huang, J.-Y. Chang, and M.-L. Wu. Enhanced light trapping based on guided mode resonance effect for thin-film silicon solar cells with two filling-factor gratings. *Optics Express*, 16(11):7969–7975, 2008. ISSN 1094-4087. doi: 10.1364/oe.16.007969.

[133] F. García-Santamaría, M. Xu, V. Lousse, S. Fan, P. V. Braun, and J. A. Lewis. A Germanium inverse woodpile structure with a large photonic band gap. *Advanced Materials*, 19(12):1567–1570, 2007. ISSN 09359648. doi: 10.1002/adma.200602906.

APPENDIX

A.1 Fresnel Correction

This calculation allows us to account for additional interfaces that were not present in FDTD simulations. The calculation can be done for a fixed number of layers (3 layers in this case), and generalized to an arbitrary number of layers. First, assume we have a homogeneous film of a single material (i.e. air-film-air with each layer numbered as layers 0, 1, and 2, respectively). R_A is the amplitude of the wave reflected directly from the top surface of the film, R_B is the amplitude of the wave reflected from the bottom surface of the film that transmits back through the top, R_C is the wave that reflects from the bottom surface, then reflects again off the top then the bottom surface, before transmitting through the top surface, and so on. R_{ij}, T_{ij}, and r_{ij} are the reflectance, transmittance, and reflection coefficient at each interface between each layer, respectively. We define useful definitions:

$$R_{01} = r_{01}^2 \tag{A.1}$$

at normal incidence:

$$R_{01} = (\frac{n_0 - n_1}{n_0 + n_1})^2 \tag{A.2}$$

as R_A is the reflectance off the top interface,

$$R_{\mathrm{A}} = R_{01} \tag{A.3}$$

From the descriptions above, where R_B and R_C describe additional internal reflection within the film:

$$R_{\mathrm{B}} = T_{01}R_{12}T_{10} \tag{A.4}$$

$$R_{\mathrm{C}} = T_{01}R_{12}R_{10}R_{12}T_{10} \tag{A.5}$$

More generally, to describe the reflectance out of the top surface after m internal reflections off the back-side of the film for ($\alpha \geq 1$):

$$R_{\mathrm{m}} = T_{01}T_{10}R_{12}^{\alpha}R_{10}^{\alpha-1} \tag{A.6}$$

As the total reflectance out of the top surface is the sum of all of these R_n terms that transmit from the film to the top surface, we can write this as a summation:

$$R_{\mathrm{tot}} = \sum R_n = R_{01} + T_{01}T_{10}R_{12}\sum_{\alpha=0}^{\infty} R_{12}^{\alpha}R_{10}^{\alpha} \tag{A.7}$$

This is a geometric series:

$$\sum_{\alpha=0}^{\infty} ar^k = \frac{a}{(1-r)} \quad \text{for} \quad |r| < 1 \tag{A.8}$$

$$R_{\mathrm{tot}} = R_{01} + T_{01}T_{10}R_{12}\sum_{\alpha}^{\infty}(R_{12}R_{10})^{\alpha} \tag{A.9}$$

$$R_{02} = R_{01} + T_{01}T_{10}R_{12}\left(\frac{1}{1-R_{12}R_{10}}\right) \tag{A.10}$$

For normal incidence, TE and TM polarizations are the same, i.e. $T = 1 - R$ for TE, but $R_{TE} = R_{TM}$. We can also utilize the property that $R_{ij} = -R_{ji}$. Furthermore, as we have considered 3 layers in an air-film-air stack, here R_{02} describes the total reflectance in this system considering all interfaces for such a stack. Simplifying further:

$$R_{\mathrm{tot}} = R_{02} = R_{01} + \frac{(1-R_{01})(1+R_{01})R_{12}}{1-R_{12}R_{10}} \tag{A.11}$$

$$= R_{01} + \frac{(1-R_{01}^2)R_{12}}{1-R_{12}R_{10}} \tag{A.12}$$

$$R_{02} = \frac{R_{01}+R_{12}}{1-R_{12}R_{10}} \tag{A.13}$$

We can take this result and generalize it to multiple layers by blocking layers together. For example, for a 5 stack (i.e. 3 layers of materials with air on the top and bottom) we can start by blocking together the air, material 1, and material 2 layers denoted as layers 0,1, and 2 respectively, then look at

reflection through a "film" of glass denoted as layer 3, with air as layer 4 on the opposite side. In doing so, our reflection coefficient is similarly:

$$R_{24} = \frac{R_{23} + R_{34}}{1 - R_{34}R_{32}} \tag{A.14}$$

$$R_{24} = \frac{R_{23} + R_{34}}{1 + R_{34}R_{23}} \tag{A.15}$$

Next, we can move up a layer, this time blocking together the air-glass layers (layers 0 and 1), then the nanopillar-glass layer (layers 2 and 3), and then the opposite air region as layer 4. Then again:

$$R_{14} = \frac{R_{12} + R_{24}}{1 + R_{24}R_{12}} \tag{A.16}$$

Finally, we group the center 3 layers, i.e. air, then glass-nanopillar-glass, and air, to find r_{04} which is reflection out of the entire stack:

$$R_{04} = \frac{R_{01} + R_{14}}{1 + R_{14}R_{01}} \tag{A.17}$$

Notice that each reflection coefficient depends on the previous one, as we successively grouped different layers together and moved up the entire stack. This provides an expression where only the reflectance between adjacent layers must be known. Substituting everything:

$$R_{04} = \frac{R_{01} + \left\{ \frac{R_{12} + \left[\frac{R_{23}+R_{34}}{1+R_{34}R_{23}} \right]}{1 + \left[\frac{R_{23}+R_{34}}{1+R_{34}R_{23}} \right] R_{12}} \right\}}{1 + \left\{ \frac{R_{12} + \left[\frac{R_{23}+R_{34}}{1+R_{34}R_{23}} \right]}{1 + \left[\frac{R_{23}+R_{34}}{1+R_{34}R_{23}} \right] R_{12}} \right\} R_{01}} \tag{A.18}$$

Similarly, for a stack of 4 layers:

$$R_{13} = \frac{R_{12} + R_{23}}{1 + R_{23}R_{12}} \tag{A.19}$$

$$R_{03} = \frac{R_{01} + R_{13}}{1 + R_{13}R_{01}} \tag{A.20}$$

$$R_{03} = \frac{R_{01} + \left(\frac{R_{12}+R_{23}}{1+R_{23}R_{12}}\right)}{1 + \left(\frac{R_{12}+R_{23}}{1+R_{23}R_{12}}\right)R_{01}} \tag{A.21}$$

The same procedure can be repeated for an arbitrary number of layers.